ABSTRACT

Title of Dissertation: THE NANOARCHITECTURE OF THE OUTER HAIR CELL LATERAL WALL: STRUCTURAL CORRELATES OF ELECTROMOTILITY

Willy Weiyih Sun, Doctor of Philosophy, 2021

Dissertation directed by: Dr. Bechara Kachar, National Institute on Deafness and Other Communication Disorders, Laboratory of Cell Structure and Dynamics

Dr. Catherine Carr, Department of Biology

Proper mammalian hearing depends on an outer hair cell-based mechanism that amplifies the sound-induced travelling waves in the cochlea. Outer hair cells (OHCs) contribute to this cochlear amplification through their electromotile property—voltage-dependent somatic length changes that can operate at acoustic frequencies. This unique form of motility is driven by prestin, a member of the solute carrier 26 family of anion transporters that is highly expressed along the OHC lateral plasma membrane. The lateral plasma membrane is supported by a cortical actin-spectrin lattice and a smooth ER system known as lateral cisternae to form a regular layered structure along the entire OHC lateral wall. The detailed structural organization of each layer and how they interact to transduce prestin conformational changes into whole-cell motility are not well understood. In this dissertation, I combine cryogenic sample preparation methods and electron tomography to elucidate the functional architecture of the OHC lateral wall complex. In chapter 1, I review the biology of the mammalian auditory system. In chapter 2, I detail how the combined methodological approach used can preserve and reveal the three-dimensional nano-architectures in cells at near-native state. In chapter 3, I describe the successful use of this methodology to elucidate the structure-function relationships in a comparable model structure, the glycocalyx on the surface of enterocytes. In Chapter 4, I provide the details on the organization of each layer of the OHC lateral wall complex and how they are structurally integrated. I show that the lateral plasma membrane contains closely tiled microdomains of orthogonally packed putative prestin protein complexes. The cortical lattice connects the plasma membrane to the adjacent lateral cisternae through two independent cross-bridging components. The lateral cisternae are in turn integrated through inter and intra-cisternal cross-bridging systems. Finally, mitochondria are attached to the lateral cisternae through another set of linker elements. By quantifying the dimensions of each of these components and mapping their distribution I provide a detailed blueprint of the nano-architecture of the OHC electromotile apparatus and discuss how its cohesive structure allows effective transmission of forces generated by prestin to the rest of the cell to drive cochlear amplification.

THE NANOARCHITECTURE OF THE OUTER HAIR CELL LATERAL WALL: STRUCTURAL CORRELATES OF ELECTROMOTILITY

by

Willy Weiyih Sun

Dissertation submitted to the Faculty of the Graduate School of the
University of Maryland, College Park, in partial fulfillment
of the requirements for the degree of
Doctor of Philosophy
2021

Advisory Committee:
  Professor Catherine Carr, Chair
  Dr. Bechara Kachar, Co-Chair
  Professor Ricardo Araneda
  Dr. Matthew Kelley
  Dr. Catherine Weisz
  Professor Matthew Goupell, Dean's Representative

Dedication

This dissertation is dedicated to my parents. Thank you for everything.

致父母，謝謝你們。

Acknowledgements

I would like to thank my advisor Dr. Bechara Kachar for his supervision and support. It is truly a privilege to conduct my research in such a high-caliber lab and to be able to take advantage of the abundant resources offered by the National Institutes of Health (NIH) & the National Institute on Deafness and Other Communication Disorders (NIDCD). I would also like to express my gratitude and appreciation to the current and former colleagues at the Kachar lab, especially Dr. Evan Krystofiak, for his mentoring and friendship. I owe many thanks to Runjia Cui, our biologist, for all her support and friendship. In addition, I would like to thank my committee members for their invaluable advice, especially Dr. Catherine Carr, my co-advisor, for her guidance and advocacy. I am indebted to Dr. Catherine Weisz and the members of her lab for support and constructive feedback.

I am grateful to have several opportunities to collaborate with and learn from experts both inside and outside of my field. I would like to thank the Weigert lab from the National Cancer Institute for their contribution to the intestinal glycocalyx project. I would like to thank Dr. Jing Zheng and Dr. Anthony Ricci for the opportunity for me to contribute to their projects. Additional acknowledgements of those contributed to specific studies and help with illustrations are indicated in the main text.

My graduate fellowship was supported by funding from NIDCD/NIH and NACS/UMD. I would like to thank the administrators at NIDCD and NACS for making this partnership program possible and running smoothly. I would also like to thank

NIDCD core facility staff for their support, especially Drs. Ronald Petralia and Dennis Winkler, for instrumentation training.

Finally, I would like to acknowledge my former mentor Dr. Alain Dabdoub and former colleagues in the Dabdoub lab, Drs. Bonnie Jacques, Joanna Mulvaney and Koji Nishimura. Thank you for inspiring me to go on this journey and equipping me with the right tools.

Thank you, family and friends, for everything.

千言萬語亦難盡述父母之恩

唯以一詩概括

十五

宋 王安石

將母邗溝上，留家白紵陰。

月明聞杜宇，南北總關心。

Table of Contents

List of Tables

List of Figures

List of Abbreviations

CL – Cortical lattice

EM – Electron microscopy

ER – Endoplasmic reticulum

LC – Lateral cisternae

LM – Lateral plasma membrane

OHC – Outer hair cell

TEM – Transmission electron microscopy

Chapter 1: Introduction

1.1 – Deafness and Hearing Loss

Hearing plays a crucial role in communication and interactions with our environment. Both hearing loss, not being able to hear as well as someone with normal hearing, and deafness, having lost most or all of our ability to hear, can significantly affect a person's health, safety, and quality of life (Jorgensen & Messersmith, 2015). While substantial progress has been made in understanding the biology of hearing, a comprehensive solution that restores hearing to those experiencing hearing loss and deafness is still a distance away. This body of research details using innovative experimental techniques to obtain a more complete picture of the cellular and molecular basis of hearing. Ultimately, this fundamental knowledge will be used to aid the formulation of therapeutics.

1.1.1 – Hearing Loss - A Growing Epidemic

The spectrum of hearing loss ranges from mild to profound with the World Health Organization (WHO) defining disabling hearing impairment to be a loss of 40 decibels (dB) or more for adults and 30 dB for children (Gaffney, Eichwald, Grosse, & Mason, 2010). Currently, the WHO estimates that roughly 466 million people or 5% of the world's population experiences disabling hearing loss, ~34 million children and

~432 million adults. Within the adult population, those 65 years of age and over are disproportionately affected with about one-third of the age group living with disabling hearing loss. By the year 2050, it has been projected that at least 900 million people, approximately 1 in 10, will have disabling hearing loss.

In the United States, about 2 to 3 per 1000 newborns have congenital hearing loss (Lin, Niparko, & Ferrucci, 2011). In the population aged 12 years and older, approximately 13% or 30 million people experience hearing loss in both ears (Mathers, Smith, & Concha, 2000). Within the US adult population, 2% of those aged 45 to 54 have disabling hearing loss. The percentage of disabling hearing loss increases significantly with age, 8.5% amongst those aged 55 to 64, ~25% for the 65 to 74 age group and 50% of those 75 years of age and older.

Global and US statistics both indicate that hearing loss is a prevalent condition, especially amongst the elder population. Our hearing is facing unprecedented challenges from the increasingly noisy environment to wear and tear associated with aging. Hearing loss and deafness is an invisible disability that could impact one’s emotional, social and financial wellbeing. Therefore, it is imperative to develop treatments to help those with hearing loss and to facilitate healthy aging. While the knowledge on how we hear and causes of hearing loss has expanded substantially over the past several decades, many fundamental questions remain to be addressed. In order to tackle this growing epidemic, we need to continue in our efforts in obtaining a comprehensive understanding of hearing and hearing loss.

1.1.2 – Forms of Hearing Loss

Our ear (Figure 1.1) is an ensemble of highly specialized parts including the outer ear (pinna, the ear canal and the tympanic membrane), the middle ear (the eardrum and three ossicles) and the inner ear (the cochlea, the semicircular canals and the auditory & vestibular nerves). These parts come together to form a sophisticated system that allows us to know that a car is coming from behind, hold a conversation in a noisy environment and differentiate the sound of a cello from a violin. Any abnormality of any part of our ear could lead to hearing loss.

There are four types of hearing loss and they are conductive, sensorineural, mixed (a combination of the prior two) and auditory neuropathy. Conductive hearing loss refers to sound not being able to propagate properly through the outer and the middle ear, which reduces the intensity of sound that reaches the inner ear. For instance, blockage of the ear canal by earwax or foreign objects, ear infection or bone abnormality can lead to conductive hearing loss. Sensorineural hearing loss is caused by damage to or loss of specialized sensory cells within the inner ear, like hair cells, and auditory nerves, the spiral ganglion, within the inner ear. Without hair cells and the spiral ganglion, the inner ear auditory organ—the cochlea—cannot convert sound into electrical signals and cannot relay sound information to the brain. Finally, auditory neuropathy is a condition where our hearing organ successfully detects and converts sound into electrical signals but fails to relay the processed sound information to the brain.

A variety of factors contributes to these different forms of hearing loss, ranging from biological to environmental. While conditions such as ear infection and physical abnormalities can be readily addressed through treatments and surgeries, factors like aging, genetic mutations, noise-induced trauma and ototoxic drugs are complex problems that require further research and development.

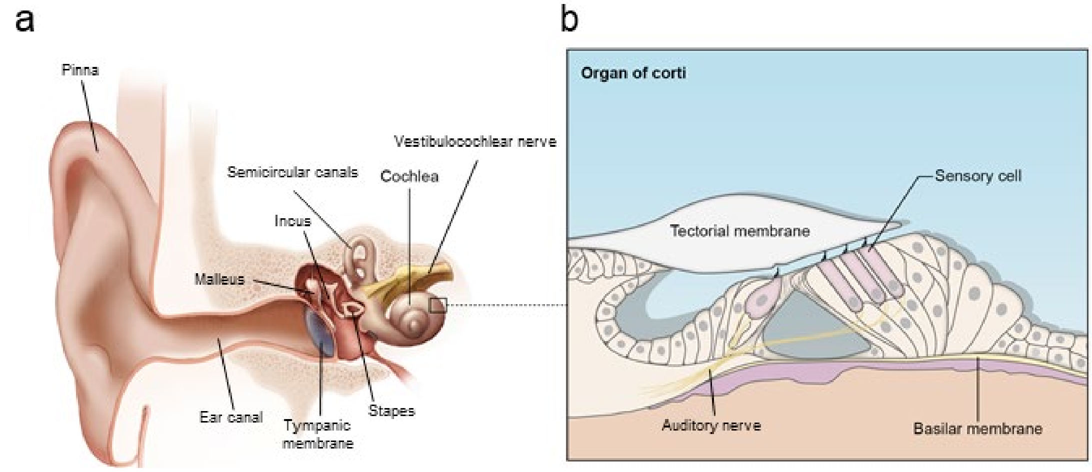

Figure 1.1 The anatomy of the human ear and the hearing organ. (a) Schematic diagram showing the organization of the outer, middle and inner ear. **(b)** A drawing showing the cellular organization of the organ of Corti. Images modified from (Schwander, Kachar, & Muller, 2010).

1.1.3 – Current Remedies and Their Limitations

Conditions that cause conductive hearing loss such as ear canal blockage can be readily corrected with well-established medical procedures. However, restorative options for symptoms of sensorineural hearing loss like hair cell loss and degeneration of auditory nerves are very limited. Currently, hearing aid and cochlear implant are the most widely used remedies for those experiencing sensorineural hearing loss.

The cochlea carries out sound amplification, transducing sound into electrical signals and works in concert with the innervating auditory nerves to relay these electrical signals to the brain for further processing. Hair cells within the cochlea play a critical role in the amplification and transduction of sound and when they are damaged or lost, the amplification and transduction capability of the cochlea is diminished or abolished. A hearing aid (Hoppe & Hesse, 2017) is a physical device with a microphone, an amplifier and a speaker (Figure 1.2a). When the cochlea loses hair cells that are responsible for signal amplification, a hearing aid can be used to partially mitigate this loss of function by amplifying the volume of sound that its microphone picks up to help drive the transduction of sound with enhanced sound intensity. However, hearing aids are only helpful to cochleae that are still largely healthy with most of their hair cell population intact. This is because amplification done by the hearing aid does not replace the biological processes carried out by the cochlea.

Another restorative option for hearing loss is the cochlear implant (Figure 1.2b). A cochlear implant differs from a hearing aid in that the implant directly interfaces with the auditory nerves, bypassing the outer & middle ear and the cochlea of the inner ear. This means that a cochlear implant (Lenarz, 2018) can help mitigate hearing loss even in cases where the majority of the hearing system is non-functional. The cochlear implant is an electronic device that is surgically inserted into the inner ear and it is composed of a microphone for sound reception, an audio processor to interpret the incoming sound and an array of electrodes that directly stimulates the auditory nerves to convey the processed sound information. It is important to note that there is a difference between how the cochlea and the sound processor of a cochlear implant encode acoustic information, which means that cochlear implant users need to undergo training to accustom themselves to this new way of hearing. Most importantly, the cochlear implant is only effective if auditory nerves are healthy and functional. In the event where auditory nerves are damaged or lost, which renders cochlear implant ineffective, auditory brainstem implant (Wong et al., 2019) provides a means to bypass the entire peripheral hearing system and transmits sound information by directly stimulating the cochlear nucleus on the surface of the brainstem. Auditory brainstem implant users also face the same problem that cochlear implant users have, namely, extensive training is needed to make use of this different form of auditory stimulation.

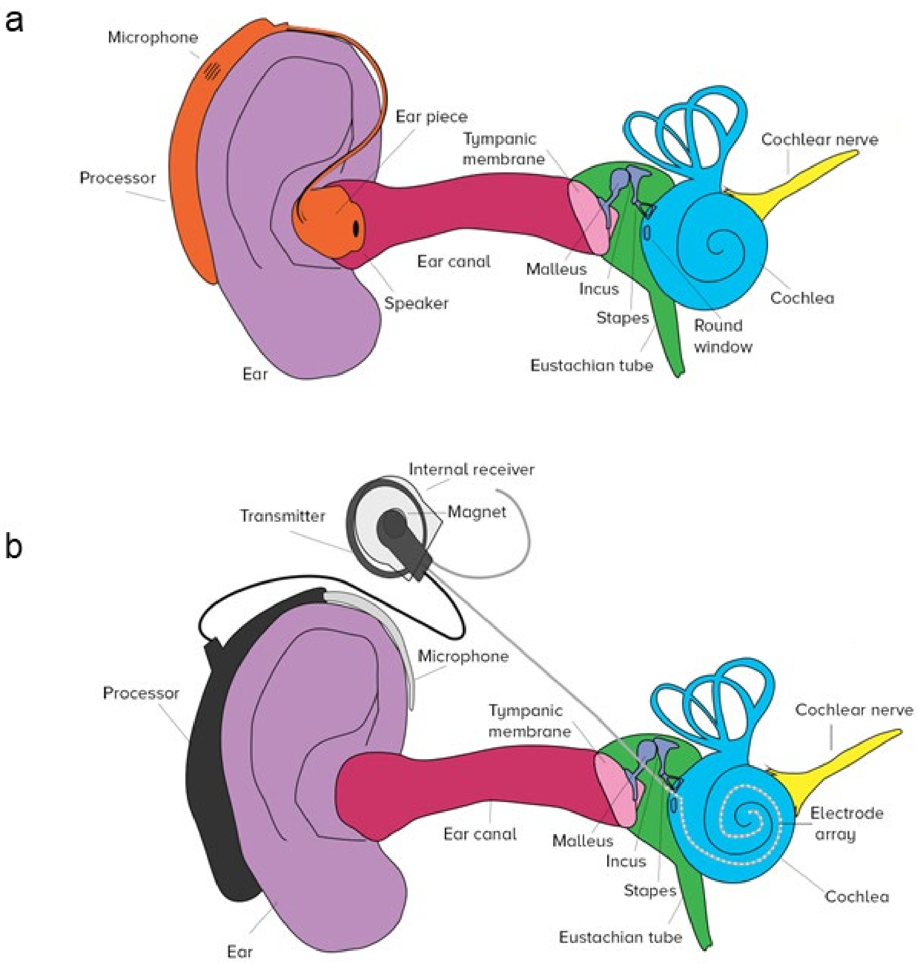

Figure 1.2 Current treatments for hearing loss. (a) A schematic of a hearing aid. **(b)** A schematic of a cochlear implant. Illustrations by Ariel Zych (Zych, 2017).

Hearing loss associated with damaged or destroyed sensory hair cells is permanent, as these specialized cells do not regenerate. While physical devices such as hearing aid, cochlear implant and auditory brainstem implant help mitigate hearing loss, they only emulate but not replace the biological processes underlying hearing. Hence, regenerative medicine treatments (S. B. Shibata et al., 2020) have been the focal point for research and development in addressing hearing loss. Current research using animal models and early phase clinical trial have shown that gene therapy has great potential for treating hearing loss. Gene therapy (Scheller & Krebsbach, 2009) is a treatment of disease by transfer of genetic material into cells, in the case of hearing loss, delivering genes to the cochlea to facilitate the regeneration of hair cells. Amongst various gene candidates, *Atoh1*, an essential regulator responsible for sensory hair cell development, has demonstrated the ability to generate hair cells in different animal models including mouse, rat and guinea pig (Izumikawa et al., 2005; Kawamoto, Ishimoto, Minoda, Brough, & Raphael, 2003; Kraft, Hsu, Brough, & Staecker, 2013; Pan et al., 2013; Woods, Montcouquiol, & Kelley, 2004; Wu et al., 2013; J. L. Zheng & Gao, 2000). While *Atoh1* gene therapy shows promise in animal models, generating new hair cells is the first step of a long journey in the development of a viable pharmacological treatment for hearing loss.

The treatments of hearing loss with hearing aids and cochlear implants have demonstrated that these artificial devices are effective in improving communication and overall quality of life for those experiencing hearing loss. However, the efficacy of hearing aids and cochlear implants is limited by our understanding of hearing and hearing loss. In addition, these devices can be cost-prohibitive, especially for patients in developing nations. On the other hand, regenerative medicine approaches to hearing loss have shown great promise, but the development of treatment like gene therapy is still in its infancy. The path towards attaining normal auditory sensation remains challenging and it will rely on the continuous refinement of our understanding of hearing and hearing loss.

1.2 – The Mammlian Cochlea

To improve on existing interventions for hearing impairment and to develop regenerative medicine treatments require an in-depth understanding of our hearing organ under normal and diseased conditions. The mammalian inner ear houses the critical infrastructure for hearing, the cochlea—a hub for biological processes underlying our auditory perception. The cochlea is a spiral-shaped organ with exquisitely arranged cellular components that modulates cochlear response through amplifying and dampening of incoming sound, converts sound into electrical signals and communicates with auditory nerves. Central to these functions are two major compartments of the cochlea: the organ of Corti and the stria vascularis. The organ of Corti is an epithelium composed of highly specialized sensory cells and supporting cells. And the stria vascularis helps to establish the endocochlear potential, an electrochemical gradient that powers the cellular processes within the organ of Corti.

1.2.1 – The Organ of Corti: A Sensory Epithelium

The major constituents of the organ of Corti (Figure 1.3a) include one row of inner hair cells (IHCs), three rows of outer hair cells (OHCs), inner & outer pillar cells, and supporting cells such as Dieters cells. These cells are polarized epithelial cells that come together to form a two-layered epithelium that is situated atop the collagen fiber-rich basilar membrane and overlaid by the collagen fiber-rich tectorial membrane. The organ of Corti follows the osseous spiral lamina of the modiolus, a bone situated at the central axis of the cochlea, and coils into a spiral. The sensory hair cells and supporting cells along the spiral have a well-defined spatial configuration. The one row of IHCs are situated closer to the medial side of the cochlea (closer to the modiolus) and the three rows of OHCs are positioned toward the lateral side of the cochlea (further away from the modiolus), with the two hair cell populations separated by inner & outer pillar cells. In addition to the well-defined spatial configuration, hair cells, supporting cells and the auditory nerves are tonotopically arranged. Tonotopy refers to arrangements of cochlear cellular components and auditory nerves that enable optimal response to incoming sound in a frequency-location specific manner. The organ of Corti exhibits varying physical characteristics along its length. At the basal end (near the round and oval windows), the three rows of OHCs are shorter in length, the width of the sensory epithelium is narrower, the basilar membrane is stiffer and the tectorial membrane is thicker. This morphology enables the organ of Corti to respond optimally to sounds at the high-frequency end of human hearing (~20 kHz). Moving towards the apical end of the cochlea, OHCs increase in length, the sensory epithelium becomes wider, the basilar membrane becomes more flexible and the tectorial membrane reduces thickness. These incremental changes in morphology from base to apex correspond to optimal cochlear response to high to low frequency sound (range of human hearing is ~20 Hz to ~20 kHz). In conjunction with the changes in cellular structures within the organ of Corti, auditory nerves that innervate hair cells also exhibit frequency selectivity that provides optimal neuronal response to high frequency sound at the basal end and low frequency sound at the apical end. The well-defined cellular configuration and the establishment of tonotopy through incremental changes in morphology and neuronal properties show that the cochlea is an extremely sophisticated piece of micro-architecture that processes sound with accuracy and precision.

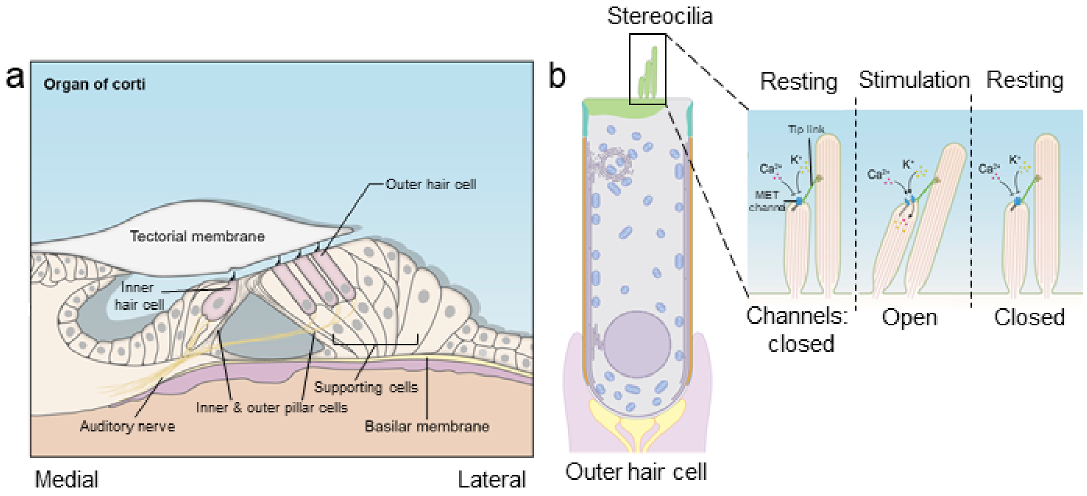

Figure 1.3 Schematic of the organ of Corti and the mechano-electrical transduction process. (a) A cartoon depiction of the organ of Corti. **(b)** A set of diagrams showing close-up views of the mechano-electrical transduction (MET) apparatus at the tips of stereocilia. Illustration modified from (Schwander et al., 2010). The outer hair cell drawing in **(b)** was illustrated by Ethan Tyler and Alan Hoofring, NIH Medical Arts Design Section.

The inner and outer hair cells within the organ of Corti, named because of hair-like actin protrusions known as stereocilia at their apical surfaces, are essential for hearing (Figure 1.3b). These actin protrusions that make up the stereocilia are not only a characteristic feature of hair cells, but they are also the main organelle that drives hair cell functions by carrying out mechano-electrical transduction (MET). Stereocilia actin bundles are graded in length and organized into a well-defined staircase architecture with the OHC stereocilia exhibiting a W-shaped pattern and the IHC stereocilia having a more linear arrangement (McGrath, Roy, & Perrin, 2017). The tips of shorter rows of the stereocilia are connected to the adjacent taller row via membrane-tethered tip links. Sound-induced vibrations move the stereocilia in the medial-lateral direction that leads to the extension of these tip links and causes stretch-sensitive ion channels at the tips of shorter row stereocilia to open. The opening of ion channels allows cations to flow into hair cells via the stereocilia, depolarizing them (Gillespie & Müller, 2009). For IHCs, depolarization leads to the release of neurotransmitters at ribbon synapses, which stimulate the auditory nerves and relay sound information upstream to the brain (Fettiplace, 2017). Depolarization of OHCs invokes a downstream process known as OHC electromotility, an essential activity in the modulation of acoustic signals and frequency tuning (Fettiplace, 2017).

To have a sustained cochlear response to sound at acoustic frequencies, hair cell activities driven by MET need to be rapid and consistent. The cochlea has adapted to the demand of continuous sensory function by establishing a large electric potential difference between hair cells and the extracellular fluid surrounding the stereocilia. Hair cell bodies and the extracellular fluid have a potential difference at approximately 150 mV. This very large potential difference provides an environment that makes cation influx favorable and reliable. This highly specialized environment that enables and sustains hair cell function is the result of cochlea compartmentalization and cochlear fluid homeostasis.

1.2.2 – The Stria Vascularis and the Endocochlear Potential

The organ of Corti is supported by the spiral lamina and is situated within the scala media, one of the three cochlear ducts encapsulated within the protective otic capsule. The scala media houses the organ of Corti and is located in between the scala vestibuli and the scala tympani with the Reissner's membrane forming the upper border to scala vestibuli and the basilar membrane partitioning the organ of Corti from the scala tympani. The scala vestibuli and the scala tympani are filled with perilymph, an extracellular fluid rich in sodium (~140 mM) but poor in potassium (~5 mM) and calcium (~1.2 mM) (Philine Wangemann & Schacht, 1996). In contrast, the extracellular fluid in the scala media, the endolymph, has a high concentration of potassium (~150 mM) with significantly less sodium (~1 mM) and calcium (~0.02 mM) (Philine Wangemann & Schacht, 1996). In addition to the unusually high concentration of potassium, the endolymph exhibits a potential of +80 mV relative to the perilymph (Von Bekesy, 1952). This combination of high potassium concentration and the endolymph's large positive potential help establish a strong electrochemical driving force for hair cell functions.

The generation of this large positive potential, the endocochlear potential, is dependent on potassium ions and involves the stria vascularis—a multilayered epithelium situated along the lateral wall of the cochlea that is central in the regulation of endolymph potassium ion concentration through potassium cycling and secretion (P. Wangemann, 2002). The stria vascularis is composed of three different types of cells, basal cells, intermediate cells and marginal cells where marginal cells are separated from the previous two by an intercellular space—the intrastrial space. The outer layer of the stria vascularis includes tight junction connected basal cells and intermediate cells with basal cells bordering fibrocytes that line the cochlear lateral wall and intermediate cells facing the intrastrial space. Basal cells are connected to fibrocytes and intermediate cells through gap junctions on the basal side and the apical side, respectively (Xia, Kikuchi, Hozawa, Katori, & Takasaka, 1999). Across the intrastrial space, marginal cells are interconnected by tight junctions to form the inner layer of the stria vascularis with the apical surface of the epithelium facing the scala media.

Hair cells and supporting cells of the sensory epithelium are interconnected by tight junctions to separate the apical surface and the basal portion of the epithelium into two different zones. The apical surface of the organ of Corti is bathed in potassium ion rich endolymph with the associated highly positive endocochlear potential while the basal portion is being surrounded by the perilymph. This difference between the apical and basal sensory epithelium creates a favorable condition for sensory transduction where the endocochlear potential drives the potassium ions in the endolymph into hair cells through MET channels at the tips of stereocilia to evoke downstream hair cell activities. To maintain this strong driving force provided by the endocochlear potential, potassium ions in the endolymph and perilymph are tightly regulated. Potassium ions in the endolymph enter the hair cells via apical transduction channels and they are transported out of the basolateral portion of the hair cells by potassium channels (Kros, 1996) into the perilymph. The recycling process is assisted by fibrocytes of the spiral ligament, which take up and funnel potassium ions in the perilymph towards the stria vascularis through a system of channels transporters and gap junctions (Johnstone, Patuzzi, Syka, & Syková, 1989; Zidanic & Brownell, 1990). Marginal cells take up the potassium ions from the intrastrial space via sodium-potassium-chloride cotransporter and secrete them into the endolymph (Shen, Marcus, Sunose, Chiba, & Wangemann, 1997; Sunose, Liu, & Marcus, 1997; P. Wangemann, Liu, & Marcus, 1995) to maintain potassium ion concentration and the endocochlear potential.

The generation and maintenance of the endocochlear potential and the homeostasis of cochlear fluids are vital for enabling and sustaining sensory functions. Mutations that affect transporters, ion channels and gap junctions can lead to disruptions of potassium ion recycling & secretion pathway, changes to the endolymphatic fluid & space, and the loss of endocochlear potential that result in sensorineural hearing loss (Birkenhäger et al., 2001; Delpire, Lu, England, Dull, & Thorne, 1999; Denoyelle et al., 1998; Schulze-Bahr et al., 1997; Teubner et al., 2003; Vetter et al., 1996). The well-organized sensory epithelium and the well-regulated cochlear fluids & endocochlear potential work cooperatively to power the continuous cochlear function that enables high-fidelity hearing.

1.3 – Cellular Basis of Cochlear Amplification and High-Fidelity Hearing

Central to our ability to hear with remarkable sensitivity and selectivity is the amplification of acoustic signals by outer hair cells and the encoding of sound information with accuracy and precision done cooperatively between inner hair cells and auditory nerves. The faithful depiction of our auditory environment allows us to pick up the sound of a pin drop, hold a conversation during a cocktail party and tell the difference between a violin and a cello. Disruptions to these cochlear functions lead to sensorineural hearing loss. The common form of sensorineural hearing loss involves the loss of outer hair cells caused by factors that include aging, noise trauma and ototoxicity. Outer hair cell and the associated cellular process—outer hair cell electromotility—are central to cochlear amplification. The loss of outer hair cells decreases cochlear amplification capability and results in losing sensitivity and selectivity. Understanding the cellular and molecular basis of cochlear amplification is crucial in engineering assistive devices such as hearing aids and cochlear implants to not only restore hearing but doing so with sensitivity and selectivity.

1.3.1 – Cochlear Mechanics

The tonotopic arrangement and biophysical properties of sensory cells & supporting cellular organizations enable the mammalian cochlea to act as a frequency analyzer where the sound is decomposed into component frequencies. The ability to break down sound into component frequencies provides the cochlea with the capability to process complex auditory information with selectivity and sensitivity and this is evident in classical studies of spiral ganglion electrophysiology (Evans, 1972; Kiang, Sachs, & Peake, 1967). Recordings of auditory nerve fibers had shown that auditory nerves are finely tuned and they exhibit the property of characteristic frequency, a specific sound frequency that the nerves are most responsive. While auditory nerves display sharp tuning, it was not apparent how the mechanical response of the cochlea to sound vibration contributes to the overall sensitivity and selectivity. The investigation of cochlear mechanics was challenging because of the fluid environment where the organ of Corti resides. A classical study examining human cochleae from cadavers carried out by Nobel laureate Georg von Békésy showed that sound produces a travelling wave, mechanical displacements of the basilar membrane in response to vibration, from the basal region towards the apex. In addition, different frequencies of sound evoke maximal deflection at different locations along the basilar membrane where the basal region showed the greatest response to high frequencies and low frequencies cause maximal amplitudes in the apical region. Observations by Békésy that the basilar membrane undergoes displacements in response to sound vibration was confirmed by Johnstone and Boyle in a follow-up experiment using live guinea pig cochlea and a much more sensitive measurement technique (Johnstone & Boyle, 1967). However, measurements on the basilar membrane showed that displacements were not as sensitive and selective as the neural tuning curve (Evans & Wilson, 1975). This discrepancy between the sharply tuned characteristics exhibited by the auditory nerves and the broader basilar membrane response indicates that there are additional tuning mechanisms within the cochlea to help enable high-fidelity hearing.

The major component of the basilar membrane is the radial collagen fibers (medial to lateral) of varying diameter (Iurato, 1962). In the late 19th century, Hermann von Helmholtz put forth a physical theory describing how the radial fibers within the basilar membrane respond to sound by suggesting that the radial fibers could resonate to different frequencies along the length of the cochlea. Observations by Békésy and others where the basilar membrane exhibits maximal deflection following cochlear tonotopy supported this idea. However, the discrepancy between the sharply tuned auditory nerves and the broad tuning curve of the basilar membrane indicates that the cochlea likely does not behave as a passive resonator, as the viscosity of the fluids surrounding the organ of Corti would dampen this mechanical vibration. To overcome the dampening of the proposed resonant behavior, an active mechanism within the organ of Corti that amplifies the resonance would be needed (Gold & Gray, 1948; Neely & Kim, 1983).

Outer hair cells are one of the two neuroepithelial cells within the organ of Corti. They are cylindrically shaped cells that organize into three rows along the length of the cochlea and they are positioned above the center of the basilar membrane. The contribution of outer hair cells to normal cochlea function and the auditory neuronal response was not clear as anatomical evidence indicates that the overwhelming majority of the spiral ganglion innervates inner hair cells (Spoendlin, 1969).

Experiments examining the effect of the loss of outer hair cells showed a decrease in auditory nerve selectivity and sensitivity (Dallos & Harris, 1978; M. Charles Liberman & Dodds, 1984), providing physiological evidence that outer hair cells participate in the fine-tuning of cochlear response. However, the precise cellular processes involving outer hair cells that lead to cochlear amplification remained enigmatic.

Breakthroughs on understanding how cochlear mechanics underlie frequency selectivity and sensitivity of the mammalian cochlea came when the observation on electrical stimulation induced outer hair cell length change was made (W. E. Brownell, Bader, Bertrand, & de Ribaupierre, 1985; William E. Brownell & Kachar, 1986; Kachar, Brownell, Altschuler, & Fex, 1986) (Figure 1.4). The experiment was done with isolated outer hair cells that were either stimulated using intracellular electrodes or by applying transcellular current (W. E. Brownell et al., 1985; Kachar et al., 1986). The significant finding was that depolarization of outer hair cells leads to a shortening of the cell while hyperpolarization elongates the cell and this electrically induced motility was referred to as electromotility (J. Ashmore, 2008; J. F. Ashmore, 1987; Dallos & Corey, 1991; Dallos, Evans, & Hallworth, 1991; M. C. Holley & Ashmore, 1988b; J. Santos-Sacchi & Dilger, 1988). The ability for outer hair cells to undergo rapid length change was quickly recognized as a potential mechanism that could modify the mechanics of the organ of Corti and help shape the frequency tuning curve (J. Ashmore, 2008; J. F. Ashmore, 1987; Dallos & Corey, 1991; Kachar et al., 1986; J. Santos-Sacchi & Dilger, 1988).

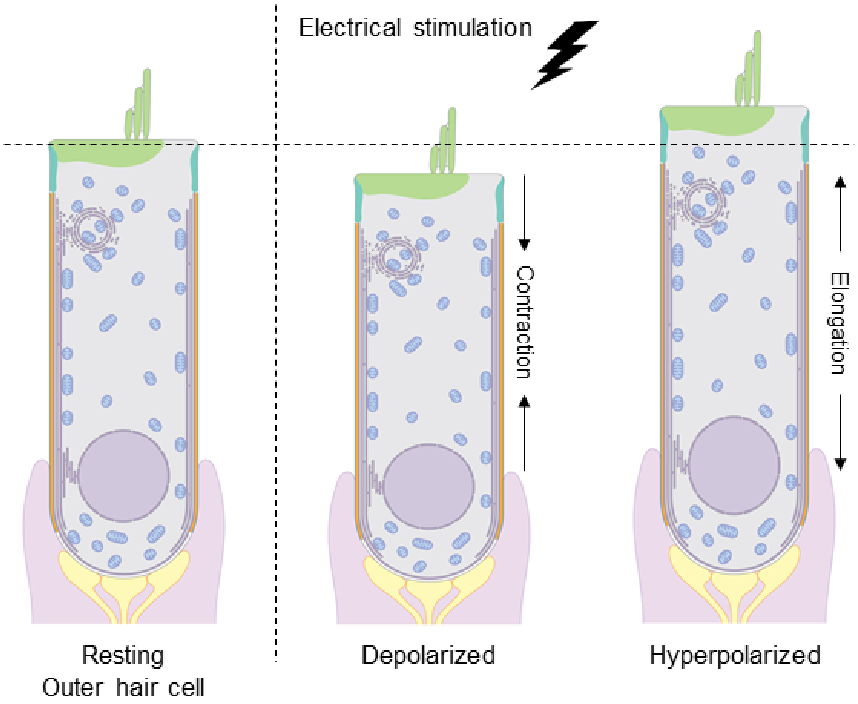

Figure 1.4 Schematic of an outer hair cell undergoing electromotility. A set of drawings showing an outer hair cell during resting, depolarized and hyperpolarized state. Illustration by Ethan Tyler and Alan Hoofring, NIH Medical Arts Design Section.

1.3.2 – Cellular Mechanisms of Outer Hair Cell Electromotility

The discovery of outer hair cell electromotility provided new insights into the cellular basis of cochlear amplification (J. Ashmore, 2008; Dallos & Corey, 1991). However, the precise cellular mechanisms that enable outer hair cells to undergo length change remain elusive. Outer hair cell electromotility is a novel form of motor activity that does not involve conventional mechanisms of cell motility (J. Ashmore, 2008; J. F. Ashmore, 1987; William E. Brownell & Kachar, 1986; M. C. Holley & Ashmore, 1988b; Kachar et al., 1986). Experimental evidence had shown that the energy required for cell length change is not directly correlated to intracellular ATP and in actuality, when ATP synthesis in mitochondria is blocked by inhibitors, shape change can still be observed (M. C. Holley & Ashmore, 1988b). Outer hair cell motility is also not dependent on actin-based or microtubule-based motility mechanisms as disrupting normal actin and microtubule functions such as treating the cell with phalloidin (stabilizes actin filaments) and colchicine (prevents tubulin polymerization) does not prevent electromotility (M. C. Holley & Ashmore, 1988b). Moreover, outer hair cell motility is sensitive to the osmotic environment. When the outer hair cell experiences an external solution that is hypo- or hyperosmotic, the cell shortens or lengthens, respectively (Dulon, Aran, & Schacht, 1987; Dulon, Zajic, & Schacht, 1990; Matthew C. Holley, 1996). Osmolarity is closely associated with the turgor pressure that the outer hair cells experience and collapsing the cell or shrinking the cell diminishes or inhibits electromotility, indicating that positive internal pressure is needed for normal motility (W. E. Brownell, 1990; Chertoff & Brownell, 1994). Examining the outer hair cell osmoregulation showed that aquaporins, a family of membrane-embedded channels that facilitate the movement of water molecules, are important in maintaining outer hair cell turgor (Belyantseva, Frolenkov, Wade, Mammano, & Kachar, 2000). These findings suggest that electromotility is associated with the cell cortex and the lateral plasma membrane of the cell (J. F. Ashmore, 1987; M. C. Holley & Ashmore, 1988a, 1988b, 1990). However, the mechanism underlying force generation and distribution that results in outer hair cell length change remains unclear. Whole-cell voltage clamp experiments showed that outer hair cell length change was not affected by changes in cellular ionic content or by the direction of the transmembrane current, providing evidence that membrane potential underlies outer hair cell electromotility (J. F. Ashmore, 1987; J. Santos-Sacchi & Dilger, 1988).

Stimulating the outer hair cell with the whole-cell patch clamp technique showed that the cell undergoes shape change relative to the fixed point of the patch location, suggesting that force is generated throughout the length of the cell (J. F. Ashmore, 1987; M. C. Holley & Ashmore, 1988b; J. Santos-Sacchi & Dilger, 1988). Furthermore, electrically divided isolated outer hair cells experienced opposite polarity in the voltage drop at their apical and basal end that caused the two ends of these outer hair cells to undergo opposite length change (i.e. when the apical portion contracts, the basal portion elongates and vice versa) (Dallos et al., 1991). These observations taken together demonstrated that the motor activity of the outer hair cell is unlikely the result of cell-scaled structural changes. Rather, electromotility is based on elements associated with the lateral plasma membrane and it is driven by changes in membrane potential. Another direct evidence that electromotility is a plasma membrane-based mechanism is derived from experiments where the intracellular trypsin digestion disrupts internal cellular structures and causes the outer hair cell to lose its cylindrical shape (Kalinec, Holley, Iwasa, Lim, & Kachar, 1992). Even with the intracellular components destroyed, membrane movement can still be detected when stimulated with voltage steps.

The concept that outer hair cell electromotility is a plasma membrane-based mechanism is not only supported by electrophysiological evidence but also by ultrastructural data. Freeze-fracture and freeze-etching replicas of outer hair cell lateral plasma membrane have shown that the plasma membrane contains a dense array of particles (Gulley & Reese, 1977; Kalinec et al., 1992). The density of these membrane particles is ~3000 per μm^2 (Kalinec et al., 1992) and they are distributed throughout the lateral plasma membrane, suggesting that these particles may be the motor elements that are distributed across the length of the cell that drive cell shape change. The exceptionally high density of motor elements suggests that even a small amount of change in their molecular configuration would change the entire cell shape, effectively behaving as an area motor—a structure in the plane of the lateral plasma membrane that switches between two configurations, extended and compact, in response to a change in membrane potential (Iwasa, 1994). Despite these lines of evidence supporting a distributed, plasma membrane-based motor mechanism, there was no concrete data to show that the tightly packed membrane particles are the molecular motors as the molecular identity of the motor element(s) remained elusive.

1.3.3 – Prestin - A Voltage-dependent Transmembrane Motor Protein

The elucidation of the molecular basis of electromotility was aided by the development and refinement of molecular genetic techniques. In the seminal study carried out by Zheng and colleagues [59], inner and outer hair cell cDNA libraries were constructed from gerbil cochleae and by subtracting common cDNAs, an outer hair cell specific library of cDNAs was established. A candidate protein containing 744 amino acids with a molecular mass of 81.4 kDa was found to be highly expressed in outer hair cells. When expressed in heterologous systems such as the TSA201 cells, the transfected cells exhibited both electromotility and non-linear capacitance—a voltage-dependent membrane capacitance that is the result of movements of a charge across the electric field of the plasma membrane. In addition, when transfection cells were treated with salicylate, a known blocker of outer hair cell electromotility (Shehata, Brownell, & Dieler, 1991), the motility in the expression system was inhibited. This protein was named "prestin" for enabling cells to undergo rapid movement (*presto* means fast in Italian). Subsequent immunolabelling showed that prestin is expressed specifically along the basolateral plasma membrane of outer hair cells (Adler et al., 2003; N. Yu, Zhu, & Zhao, 2006).

Prestin is member A5 within the SLC26 family of integral membrane proteins that function as anion exchangers and anion channels that transport chloride, bicarbonate, sulfate and other substrates (Alper & Sharma, 2013; Lohi et al., 2000). The SLC26 family currently contains 11 members and they share similar general structural features, based on the x-ray crystal structure of SLC26Dg, a prokaryotic homolog (Geertsma et al., 2015). All members have a hydrophobic membrane-embedded transport domain that contains a 7 transmembrane domain inverted repeat architecture (a total of 14 α-helices) and a C-terminal cytoplasmic STAS (sulfate transporter and anti-sigma factor antagonist) domain that is involved in intracellular trafficking and protein-protein interactions (Ko et al., 2004; Shibagaki & Grossman, 2004, 2006). While other members of the SLC26 family facilitate the transport of a broad variety of anions, prestin is an exception where it functions as a voltage-sensitive molecular motor that evokes rapid length changes in outer hair cells and contributes to cochlear amplification that enhances auditory sensitivity (Joseph Santos-Sacchi, Navaratnam, Raphael, & Oliver, 2017). Even though prestin does not exhibit anion transport capability, it still interacts closely with anions, mainly intracellular chloride anions (Oliver et al., 2001). Intracellular chloride is critical in modulating prestin function, when cytoplasmic chloride anions are removed or when salicylate, a competitive antagonist is introduced, cell motility and the characteristic nonlinear capacitance are abolished or reduced (Oliver et al., 2001). Due to the lack of experimentally determined prestin protein structure, how prestin confers motility when evoked by membrane potential changes remains unclear. It has been speculated that prestin undergoes conformational changes through binding of chloride anion and performing incomplete cycles of the ion transport function when evoked by membrane potential change.

The significance of prestin to cochlear amplification is clearly illustrated in animal models. In prestin-knockout mice, the length of outer hair cells is reduced, the stiffness of the cell is lessen, and electromotility is completely lost (Cheatham, Huynh, Gao, Zuo, & Dallos, 2004; Cheatham et al., 2007; M. C. Liberman et al., 2002). The lack of electromotility shifted the hearing threshold of these mice by ~50 dB and frequency selectivity is also impaired. While these results indicate that prestin is required for electromotility, it is not clear the degree prestin contributes to cochlear amplification given the observed structural and mechanical changes in the organ of Corti of knockout mice. To examine specifically how prestin contributes to cochlear amplification, a prestin knock-in mouse line was generated where mechanics and structure of outer hair cells remain intact and only prestin function was affected (Dallos et al., 2008). Two amino acids were substituted in this prestin knock-in mouse line, V499G and Y501H, they were chosen based on transfected HEK cell studies where the substitutions significantly diminished the characteristic nonlinear capacitance (J. Zheng et al., 2005). Further characterization of the knock-in mutant showed that the mutation altered the kinetics of prestin, impairing the distinctive rapid motor activity (Homma, Duan, Zheng, Cheatham, & Dallos, 2013). These data indicate that prestin is central in electromotility and is the dominant contributor to cochlear amplification. Finally, there is evidence that genetic mutations that affect prestin lead to deafness (Mutai et al., 2013).

The discovery of prestin has greatly expanded our understanding of the cellular and molecular basis of cochlear amplification and how the cochlea enables high fidelity hearing. While prestin is at the center of electromotility, key cellular cytoskeleton and organelles intimately associated with the lateral plasma membrane are also necessary for normal outer hair cell function. For instance, an actin-spectrin cortical cytoskeleton that scaffolds the outer hair cell lateral plasma membrane is believed to play an important role in transmitting force generated by prestin to the rest of the cell to achieve overall cell shape change. In prestin-knockout mice, this cytoskeleton does not form, suggesting that prestin and the underlying supporting infrastructure are closely tied during development and are necessary for normal electromotility (He et al., 2010).

1.4 – Cellular Structural Basis of Outer Hair Cell Electromotility

An isolated outer hair cell is readily distinguishable under a light microscope as outer hair cells contain a system of smooth endoplasmic reticulum (ER)—the lateral cisternae—that is situated adjacent to the lateral plasma membrane (Saito, 1983), which makes the boundary of outer hair cells more defined. Situated in between the lateral plasma membrane and the lateral cisternae is a sub-membrane actin-spectrin cytoskeleton—the cortical lattice—with circumferentially oriented parallel actin filaments cross-linked by spectrin molecules in the axial direction (M. C. Holley & Ashmore, 1988a, 1990). The cortical lattice is presumed to be connected to the lateral membrane via pillar-shaped proteins (A. Forge, 1991; M. C. Holley & Ashmore, 1990; M. C. Holley, Kalinec, & Kachar, 1992). These structures form a layered organization spanning the length of the outer hair cell forming the outer hair cell lateral wall complex. While the identification of the molecular motor, prestin, provided a molecular basis for the force production of this unique form of membrane-based motility, there are still many questions regarding how prestin activity in the lateral membrane interacts with the underlying supporting cellular structures to generate outer hair cell length change. This body of work focuses on elucidating the structural and molecular correlates of outer hair cell electromotility to better understand outer hair cells' role in cochlear amplification and the relationship between outer hair cell dysfunction and hearing loss inducing factors such as noise, ototoxic drugs and age.

1.4.1 – The Outer Hair Cell Electromotile Machinery - A Multilayered Cellular Complex

The major structural components of the outer hair cell lateral wall have been elucidated with the help of a wide range of imaging techniques, including transmission electron microscopy (TEM), scanning electron microscopy and atomic force microscopy. The outer hair cell lateral wall is a stratified complex that contains three main constituents and they are the lateral plasma membrane with motor protein prestin, the cortical actin-spectrin lattice and a multilayered smooth ER system called the lateral cisternae (Figure 1.5). These elements form a trilaminar structure stretching from just below the cuticular plate region at the apical end to the nucleus region at the basal end.

Figure 1.5 (page 29) Schematic diagrams showing cellular and molecular details at the outer hair cell lateral wall. The outer hair cell lateral wall contains dedicated structural components for outer hair cell electromotility. These components are arranged into structurally distinct layers. Outer hair cell drawing by Ethan Tyler and Alan Hoofring, NIH Medical Arts Design Section.

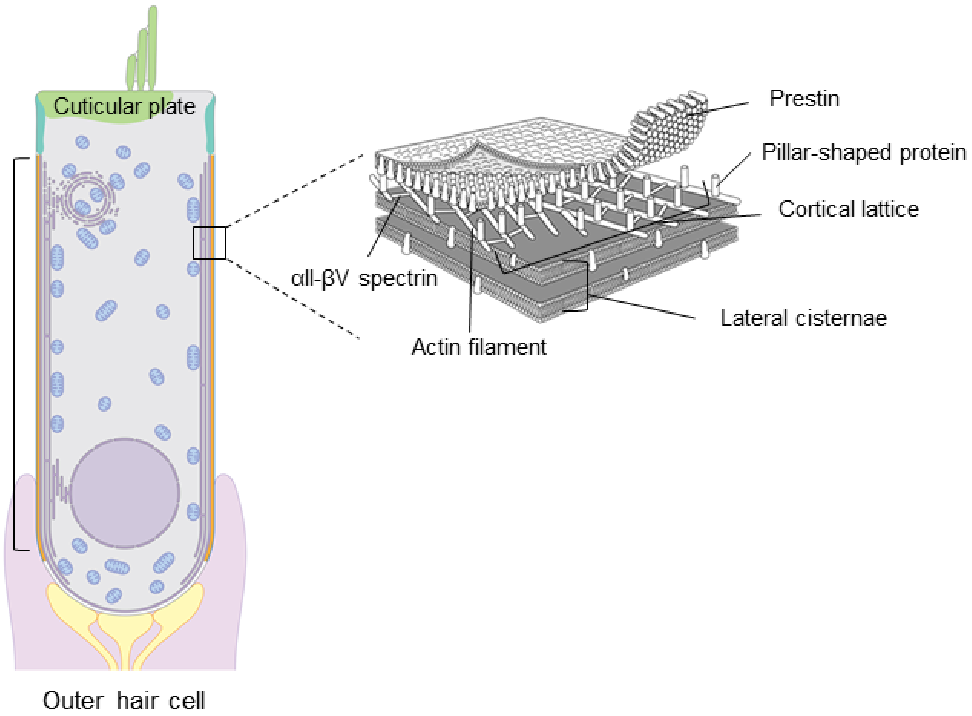

Figure 1.5 (legend on page 28)

The lateral plasma contains the molecular motor prestin that is responsible for generating the mechanical force that drives outer hair cell motility. Prestin is found to be highly expressed along the length of the outer hair cell lateral plasma membrane (Adler et al., 2003; N. Yu et al., 2006). Freeze-fracture and freeze-etching replicas have revealed that the lateral membrane is tightly packed with membrane particles 11~15 nm in diameter (Kalinec et al., 1992) and these particles have been ascribed to represent how prestin is organized in the membrane. The dimension of these membrane particles was further characterized using single particle analysis showing that the membrane particle is a bullet-shaped structure with four-fold symmetry and is ~8 nm in diameter (Mio et al., 2008). The idea that these membrane particles are prestin molecules is supported by freeze-fracture data from prestin-knockout mice, where the number of membrane particles is greatly reduced in the knockout (He et al., 2010). The highly dense membrane particles have also been shown to play a role in compartmentalizing the outer hair cell basolateral plasma membrane (Takahashi et al., 2018). However, these membrane particles do not appear to be randomly organized across the lateral membrane, instead, they have been suggested to aggregate and form microdomains (Kalinec et al., 1992; Kitani, Park, & Kalinec, 2013). The biggest challenge in obtaining a comprehensive understanding of how prestin is expressed and organized in the lateral membrane is the lack of experimentally determined prestin protein structure. Current protein modelling data of prestin is based on the crystal structure of bacterial uracil transporter UraA and a prokaryotic homolog SLC26Dg (Geertsma et al., 2015; Gorbunov et al., 2014). The homology model of prestin contains 14 transmembrane domains configured in a 7 transmembrane domain repeat architecture with both the N- and the C-terminal located on the cytosolic side of the plasma membrane with a dimension of 4.5 x 6 nm (Geertsma et al., 2015; Gorbunov et al., 2014). The difference between the dimension of the membrane particle and the dimension of monomeric prestin suggests that prestin is likely expressed as an oligomer. Biochemical analysis and light microscopy experiments have indicated that prestin forms dimers and tetramers (Hallworth & Nichols, 2012; J. Zheng et al., 2006).

Situated directly beneath the prestin-packed lateral membrane is the actin-spectrin cortical lattice. The lattice contains circumferentially oriented parallel actin filaments that are cross-linked in the axial direction by αII-βV spectrins and they are organized into microdomains up to 10 μm^2 in size (M. C. Holley et al., 1992; Leonova

& Raphael, 1999; Wada et al., 2004). Immunolabelling revealed that the cortical lattice structure shares the same expression pattern as prestin, spanning the length of the lateral plasma membrane (Legendre, Safieddine, Kussel-Andermann, Petit, & El-Amraoui, 2008). The cortical lattice is directly connected to the lateral membrane through pillar-shaped proteins of unknown molecular identity and makeup (A. Forge, 1991; M. C. Holley & Ashmore, 1990; M. C. Holley et al., 1992). These pillars are believed to play a critical role in transmitting the force generated by prestin molecules in the membrane to the underlying cytoskeleton to generate whole-cell shape change (W. E. Brownell, Spector, Raphael, & Popel, 2001). The actin filaments and spectrin molecules within the cortical lattice have different mechanical properties with spectrin likely being the more flexible of the two, as spectrin repeats can undergo reversible folding when stressed (Discher & Carl, 2001). This difference is reflected in the stiffness of the outer hair cell as circumferential stiffness is higher than the axial stiffness (Tolomeo, Steele, & Holley, 1996). The anisotropic stiffness of the cortical lattice likely underlies how outer hair cells maintain their cylindrical shape while spectrin molecules respond to the force generated by prestin motors in the axial direction by undergoing reversible folding (W. E. Brownell et al., 2001; M. C. Holley & Ashmore, 1990).

The lateral cisternae is the most prominent component with this trilaminar system, however, much of its role in outer hair cell function remains elusive. A recent ultrastructural study has revealed that the lateral cisternae is directly attached to the cortical lattice through unknown linker proteins and the lumen of the cisternae contains repeating structures (Triffo et al., 2019). In addition, the lateral cisternae exhibit regular intra- and intercisternal spacing. The innermost layer of the lateral cisternae is often accompanied with mitochondria, the close association between the two organelles suggests a potential function for the lateral cisternae involving ER-mitochondria interaction and mitochondrial bioenergetics.

1.4.2 – Nano-organization of the Electromotile Machinery in Near-native State

Great strides have been made in elucidating cellular structures and their components that enable outer hair cell electromotility over the past several decades, however, many unresolved questions remain. Ultrastructural studies are often limited by sample preparation techniques, available technology and imaging modality. For instance, TEM has been the standard imaging modality for obtaining ultrastructure with nanometer-scaled details, however, conventional TEM imaging method produces micrographs that are a 2D projection of a 3D structure. This means that molecules or structural features may superimpose on top of each other that leads to the loss of the correct spatial information. Sample preparation is another critical step as artifacts can be introduced during one or more of the many steps, including the type of fixation, quality of reagents, contrast staining, dehydration, embedding and others. Improper sample preparation could lead to misinterpreting artifacts as naturally occurring structural features that could result in falsifying a valid hypothesis and more.

Proper characterization of the outer hair cell lateral wall complex requires a detailed understanding of its 3D nano- and molecular architecture *in vivo*. The 3D nano-architecture can be obtained through the use of electron tomography, a method for reconstructing structural features of an object with the correct spatial distribution from projection images (Frank, 2006). While it is currently not possible to evaluate the ultrastructure *in vivo*, cryofixation offers the ability to preserve the sample in a state that is near its *in vivo* state through vitrification of the water content (Marko, Hsieh, & Mannella, 2006). By combining cryofixation and electron tomography, one can visualize and examine an ultrastructure in 3D in its near-native state.

This body of work details my endeavor on obtaining a detailed structure of the outer hair cell electromotile machinery. Chapter 2 provides in-depth background on the techniques that are used in my studies and the materials and methods of experiments that took place. Chapter 3 describes my contribution to the development of a novel imaging modality of cryogenically prepared samples, the proof of principle and improving image & quantitative analysis methods. Chapter 4 presents my examination of the 3D organization of the lateral wall complex in its near-native state with nanometer-level detail and how these newfound ultrastructural insights can help answer whether the trilaminar system with its interconnected components operates as the functional unit for electromotility. Finally, chapter 5 provides a summary that details the layout of an up-to-date nanoarchitecture of the lateral wall complex and how that can be used as a blueprint to better understand the cellular and molecular basis of outer hair cell electromotility and its role in cochlear amplification.

Chapter 2: Methods for Imaging the Nanoarchitecture of Cellular Organizations at Near-Native State

2.1 – Introduction

In electron microscopy, the use of chemical fixatives to preserve the underlying ultrastructure of biological samples is a routine procedure. However, chemical fixatives take time to diffuse through a sample to form chemical crosslinks, making it difficult to capture biological structures in a near-native state. In addition, chemical fixatives can introduce perturbations to biological structures due to the specificity of the chemical crosslinks formed. Therefore, an alternative preservation method that is capable of rapidly fixing samples without introducing structure-altering artifacts is needed. To overcome these challenges, rapid freeze techniques that enable fast immobilization of biological structures while introducing minimal artifacts have been developed. Rapid freezing techniques also allow visualization of the underlying macromolecular complexes in 3D in a close-to-life state through electron tomography. This chapter provides the background on cryogenic sample preparation methods and 3D visualization of ultrastructures via electron tomography and image segmentation.

2.2 – Cryogenic Electron Microscopy Methods

Biological structures are intimately tied with their functions. For instance, the length of hair cell stereocilia, regulated by the actin filament organization within the organelle, is critically important for normal hearing (Manor et al., 2011). Electron microscopy (EM) has been the standard imaging method for elucidating structure-function relationships due to its ability to visualize molecular architectures with nanometer & sub-nanometer resolution. In order to preserve biological structures, samples prepared for conventional EM typically are chemically crosslinked by undergoing aldehyde-based chemical fixation. While chemical fixation is effective in stabilizing cellular organizations, it can also introduce fixation artifacts. Fixatives such as formaldehyde and glutaraldehyde readily interact with a specific chemical group, the amines, within proteins and other cellular components. These aldehydes also have well-defined dimensions (Sutherland, Toews, & Kast, 2008) and in combination with reaction specificity, aldehyde fixation crosslinks cellular components together to generate a still frame of the dynamic biological sample to highlight potential molecular interactions, co-localization and two- or three-dimensional cellular organizations. However, immobilization of cellular components through chemical fixation takes time because fixatives have to diffuse across the sample and biological structures may undergo changes during the fixation process. Therefore, it is challenging to discern what information is and is not physiologically relevant. Misinterpretation of the results could lead to a faulty conclusion. Chemical fixation also introduces obstacles for immunolabelling-based experiments as specific interactions between fixatives and chemical groups within proteins could alter the epitopes. In addition to chemical fixation artifacts, conventional EM sample preparation involves dehydrating the sample for resin embedding, another step that can introduce ultrastructure-altering artifacts. Proper infiltration of resin throughout the sample and polymerization requires the removal of water contents within the sample. This is typically carried out by displacing water with organic solvents such as acetone and methanol. However, given that biological samples are largely composed of water, this dehydration step could affect native biological structures such as the organization of highly hydrophilic cellular components.

An alternative preservation method to chemical fixation that avoids artifacts associated with fixatives is cryofixation, which preserves biological structures through freezing. Cryofixation takes advantage of the fact that biological samples are largely composed of water and rapidly immobilizing the water content within a sample can preserve the underlying cellular organizations without the need of crosslinkers. However, under normal temperature and pressure, water forms ice crystals and increases the amount of space it occupies when transitioning from liquid to solid phase. The presence of crystalline ice in a sample is detrimental to the underlying structures as ice crystals can severely disrupt and displace cellular components. There are various cryofixation methods such as plunge freezing, slam freezing and high-pressure freezing (Marko et al., 2006). These methods can preserve biological structures with minimal to no disruption by achieving vitrification—transitioning water into an amorphous solid. To attain vitrification, the different types of freezing utilize various physical parameters such as increasing the rate of heat transfer and pressure to minimize ice crystal formation. Plunge freezing (Gilkey & Staehelin, 1986; Sitte, Edelmann, & Neumann, 1987) involves submerging the sample into a cryogen with a fast cooling rate, typically liquid ethane at ~ -180 ºC, and can yield a good freezing region < 5 μm from the border of the sample. Slam freezing (Gilkey & Staehelin, 1986; Luther, 2006; Marko et al., 2006) brings the sample into direct contact with the polished surface of a liquid nitrogen cooled (< -180 ºC) metal block (typically made of copper) that has an extremely high cooling rate and can vitrify a region ~10 - 30 μm deep from the impact site. High-pressure freezing (Bullen et al., 2014; Marko et al., 2006) vitrifies the sample by applying liquid nitrogen at high pressure ($\geq 2 \times 10^8$ Pa). The high-pressure environment significantly decreases the chance of ice crystal formation and enables vitrification at greater depth, ~100 - 300 μm from the sample border.

Cryofixation offers unparalleled preservation of biological structures because the sample stays hydrated, the process requires no additional fixatives and is very fast (on the millisecond to the second scale). On the other hand, chemical fixation can induce fixative-associated artifacts and the time it takes (from minutes to hours) the fixative to penetrate the sample would lead to capturing biological structures that have deviated away from their physiological state. The aforementioned rapid freezing methods in combination with freeze substitution, embedding samples into plastic in low-temperature conditions (-90 ~ 0 ºC), have been demonstrated to produce plastic-embedded samples with the best sample preservation for inner ear tissue and a wide range of samples (Bullen et al., 2014; Echlin, 1992; Giddings et al., 2001). While rapidly frozen, freeze-substituted, plastic-embedded samples can provide many insights on interaction, localization and ultrastructural organization, the method is not particularly well suited for examining transmembrane proteins, membrane-associated structures and components that are embedded in the lipid bilayer. These challenges associated with classical thin-section of plastic-embedded samples can be overcome using a unique replica-based cryogenic method, freeze-fracture/freeze-etching electron microscopy (John E. Heuser, 2011). This technique can help maintain structural integrities of hydrophilic cellular components as the sample is rapidly frozen in a fully hydrated state. Fracturing and etching of the sample are carried out in a low-temperature (typically between -120 ~ -100 ºC) and high vacuum environment. This condition helps with the separation of the two leaflets of the lipid bilayer, allowing close examination of the constituents within the plasma membrane. In addition, the removal of ice through etching can help reveal the topographical details of the plasma membrane and its associated organizations (J. E. Heuser & Reese, 1981; Kachar et al., 1999; Kachar, Parakkal, Kurc, Zhao, & Gillespie, 2000).

This body of work utilizes the combination of cryofixed, freeze-substituted, plastic-embedded samples and replica-based freeze-fracture/freeze-etching electron microscopy to reveal the nanoarchitecture of complex cellular organization such as the trilaminar outer hair cell lateral wall system in a near-native state. Advanced imaging methodology such as electron tomography is employed to elucidate the ultrastructural information contained within these well-preserved biological structures.

2.3 – Electron Tomography

Transmission electron microscopy (TEM) enables visualization of biological structures at the nano- to sub-nanometer length scales. In addition, TEM has sufficient depth of field that structural features within an ultra-thin section that is typically 100 nm or less will be in focus. This means that TEM produces images that are projections of all structures present in the section. The superposition of different structures of a 3-dimensional (3D) specimen in a 2-dimensional (2D) image makes it difficult or impossible to determine depth information from a single TEM image. However, it is possible to reconstruct a 3D object from 2D projections. Electron tomography is a method for reconstructing a 3D object from its projections by using the mathematical principle of Fourier-slice theorem (Crowther, DeRosier, & Klug, 1970), where the Fourier transform of a 2D projection is equivalent to the central slice of the Fourier transform of the 3D object. This means that a 3D object's Fourier transform is a compilation of the individual Fourier transform of 2D projection and by using the Fourier inversion theorem, the 3D object can be reconstructed from projection images. The current workflow of electron tomography involves the acquisition of a series of 2D projections of the 3D specimen by incrementally tilting the sample to obtain sufficient 2D projections for the subsequent image processing. Advancements in specimen holders, digital detectors and image acquisition and processing software have greatly reduced the time need to acquire large image data sets and considerably improved the tomographic volumes reconstruction process (Kremer, Mastronarde, & McIntosh, 1996; Mastronarde, 2005).

Electron tomography enables the retrieval of depth information within a 3D specimen but the ability to elucidate spatial information in the Z plane is limited. For symmetrical 3D objects such as the helical-shaped bacteriophage T4 (De Rosier & Klug, 1968), the 3D Fourier transform of the object can be readily extrapolated from a small set of 2D projection views. However, most biological samples are not symmetrical and need a series of 2D projections to minimize or prevent information loss. In electron tomography, different 2D projections are generated by tilting the specimen around a single axis against a fixed direction electron beam. To accurately reconstruct the 3D Fourier transform of a non-symmetrical specimen, we need to obtain 2D projections of the sample through a range of ± 90º. However, the actual tilt range of a sample is restricted by the support of the specimen, such as a metal mesh grid, the specimen holder and the sample itself. At high tilt angles, the metal mesh grid and the specimen holder could obstruct the path of the electron beam. In addition, tilting the sample away from 0º increases the mean path length that electrons have to traverse through the sample. This effectively reduces the number of electrons reaching the detector and degrades image quality. In practice, commercially available equipment allows a tilt range about ± 75º depending on sample thickness, which means that for biological structures without symmetry, creating the “missing wedge problem” as a substantial portion of the 3D Fourier transform cannot be measured. However, the loss of information at higher tilt angles can be partially recovered by collecting 2D projections over multi-axis tilt series (Lanzavecchia et al., 2005).

To elucidate the detailed 3D structural information from directly frozen, freeze-substituted, plastic-embedded samples and freeze-fracture/freeze-etching replicas, I utilized dual-axis electron tomography where the two sets of 2D projections are collected ± 60° along orthogonal tilting axes (Penczek, Marko, Buttle, & Frank, 1995).

2.4 – Tomographic Data Analysis and Segmentation

A tomographic data set is very similar to that of a Z-stack from light microscopy. The Fourier transform of 2D projections is reconstructed into slices containing the proper spatial information and compiled into a volume. Objects within the volume can be examined by going through the stack of tomographic slices. However, it is difficult to fully comprehend the three-dimensionality of the tomographic data as details of individual structures or interactions within a complex organization might be difficult to distinguish in slice-view due to object-of-interest being obscured by surrounding elements. To extract independent objects within a tomographic volume, individual slices can be segmented and compiled to produce a 3D view of objects. Segmentation is a method of compartmentalizing an image to identify unique components and structures base on parameters such as intensity, texture, shape and pattern (Frangakis & Hegerl, 2006). Image segmentation can be done manually, relying on the expert knowledge of researchers, or with the help of specialized algorithms such as edge detection, shape recognition and filament tracing. In addition to the visualization of tomographic data in 3D, segmentation is an important tool for quantitative analysis as segmented data can be used for measuring dimensions, identifying sites of interaction and determining spatial relationships with other elements.

While segmentation is a powerful tool for 3D visualization and quantitative analysis, it is a difficult technique to master and can be labor-intensive. Currently, most segmentation is done manually, a time-consuming process as researchers have to manually trace object-of-interest throughout the tomographic volume (Jiang, Ji, Wang, & McEwen, 2006). In addition, identification of independent structures, unique interactions or specific patterns depends on researchers' experience, making the process prone to operator error for complex structures or biases from prior knowledge (Jiang et al., 2006; Marsh, Mastronarde, Buttle, Howell, & McIntosh, 2001). Recent advancements in machine learning and the development of specific and general-purpose segmentation software have greatly improved the segmentation workflow (Lučič, Rigort, & Baumeister, 2013).

Segmentation is a key aspect of my research as I am using segmentation to highlight structural details within tomographic volumes that I obtained from electron tomography on plastic sections of directly frozen and freeze-substituted samples. Moreover, segmentation is being used to elucidate the fine topographical features of freeze-etching replicas, a novel qualitative analysis of replicas and is part of the freeze-etching electron tomography technique that I helped develop.

2.5 – Materials and Methods

2.5.1 – Using the intestinal epithelium to develop freeze-etching electron tomography

2.5.1.1 – Animals

All experiments carried out on animals adhere to the Guide for the Care and Use of Laboratory Animals by NIH and approved by Animal Care and Use Committees for the National Institute on Deafness and Other Communication Disorders (NIDCD ACUC, protocol #1215) and the National Cancer Institute (NCI ACUC, protocol #LCMB-031). Transgenic mouse strain expressing plasma membrane-targeted mTomato/mGFP (Muzumdar, Tasic, Miyamichi, Li, & Luo, 2007) was acquired from the Jackson Laboratory (stock #: 007576).

Mouse small intestinal tissues were collected from C57BL/6 mice of both sexes and ages between 1 to 3 months. Mice were euthanized by CO_2 asphyxiation and then decapitated. The mouse abdomen was dissected open and segments of the small intestine were quickly excised and placed into phosphate-buffered saline (PBS) or Medium 199 (ThermoFisher). These small intestine segments were fine dissected to expose the luminal surface of the small intestine and were either directly frozen or fixed for downstream processing.

For intravital microscopy, transgenic mice expressing membrane-targeted mTomato/mGFP were anesthetized by intraperitoneal injection of a mixture of ketamine (100 mg/kg) and xylazine (20 mg/kg). The abdomen of the mouse was cleaned and dissected open to externalize a segment of the small intestine. During the experiment, the body temperature of the mice was controlled and maintained at 37 ºC.

2.5.1.2 – Fast freezing and electron microscopy

Samples were fixed with 2% glutaraldehyde for 2 hours while rocking and then washed extensively in ddH_2O. Samples were then fast frozen by rapid contact with the surface of a liquid nitrogen-cooled sapphire block using a Life Cell CF-100 freezing machine. Unfixed samples were directly frozen as described in Medium 199 (ThermoFisher) or the media was replaced with ddH_2O immediately prior to freezing to reduce the amount of salts frozen with the tissue. Frozen tissues were either directly transferred to a Balzers freeze-fracture apparatus under liquid nitrogen condition for freeze-fracture/freeze-etching or they are stored in liquid nitrogen.

2.5.1.3 – Freeze-etching electron microscopy

Frozen samples were transferred in liquid nitrogen to a Balzers freeze-fracture apparatus equipped with a turbo molecular pump (Pfieffer) and a scroll pump (Edwards). Samples were inserted into the specimen holding stage that had been pre-cooled to liquid nitrogen temperature (< -180 ºC). After sample insertion, the vacuum chamber was allowed to recover to 5×10^{-6} mbar or better before the fracturing microtome was cooled to liquid nitrogen temperature. After the knife's temperature stabilized and the vacuum chamber reaches below 10^{-7} mbar, the specimen stage temperature was raised to -110 ºC. Samples were then freeze-fractured followed by freeze-etching under the microtome at a specimen stage temperature of -100 ºC for 10 minutes. Freeze-etched samples were rotary shadowed at an angle of 25º with platinum/carbon and stabilized with carbon (deposition at 90º) using electron-beam metal-evaporation guns (Cressington Scientific) to create replicas of the exposed surfaces. Samples were retrieved from the freeze-fracture machine and cleaned with sodium hypochlorite to remove the biological tissues. Replicas were then washed with distilled water and collected onto 300 mesh hexagonal copper grids (Electron Microscopy Sciences). 20 replicas from 6 different mice aged between 1 to 3 months were produced and examined.

2.5.1.4 – Freeze substitution

Samples were fixed as described and then equilibrated to 30% glycerol for cryoprotection. Tissues were then plunge-frozen in liquid ethane at -180 ºC using a Leica Biosystems grid plunger. Frozen samples were transferred to a Leica Biosystems AFS for freeze substitution. Tissues were submerged in 1.5% uranyl acetate in absolute methanol at -90 ºC for 2 days and infiltrated with HM20 Lowicryl resin (Electron Microscopy Sciences) over 2 days at -45 ºC. The resin was polymerized with ultraviolet light for 3 days at temperatures between -45 ºC to 0 ºC. Ultrathin sections at 70 nm were generated using a Leica ultramicrotome and collected onto 300 mesh hexagonal copper grids (Electron Microscopy Sciences).

2.5.1.5 – Transmission electron microscopy imaging and electron tomography

Replicas and ultrathin sections were examined using a 200 kV JEOL 2100 electron microscope equipped with an Orius 832 CCD camera (Gatan) or a OneView CMOS camera (Gatan). Single images were acquired with DigitalMicrograph (Gatan). Dual-axis tilt series from -60º to +60º at 1º increments and montages of replicas were captured using SerialEM [114]. Montage blending and tomogram reconstruction were done using the IMOD software suite (Kremer et al., 1996). 13 sets of double-tilt tilt series and 19 montages were collected, processed and analyzed.

2.5.1.6 – Quantitative image analysis

Analysis of glycocalyx packing was done using the fast Fourier transform function in DigitalMicrograph (Gatan) or FIJI (Schindelin et al., 2012). 3D analysis of the distance between glycocalyx filament termini was performed using a custom MATLAB (Mathworks) script. 3D coordinates of the individual terminal from a large tomographic volume were manually collected using FIJI. These coordinates were imported into MATLAB where the standard distance between two points formula for the Cartesian coordinate system was used to calculate the nearest neighbor for each terminal and the average and standard deviation for the distance between two termini. The histogram with a Gaussian fit overlay showing the distribution of nearest neighbor distances was generated using the MATLAB histfit function.

2.5.1.7 – Segmentation

Segmentation and visualization of tomograms were carried in Amira (ThermoFisher). The electron-dense platinum deposition replicating the glycocalyx filaments was segmented out via manual thresholding. 3D renderings of these segmented filaments were generated by using the isosurface module.

2.5.1.8 – Immunofluorescenct labelling of mouse small intestine

Mouse small intestinal tissues were dissected and collected from C57BL/6 mice aged between 1 to 3 months. Samples were fixed with 4% paraformaldehyde and then underwent graded sucrose steps (10% > 20% > 30%) for cryoprotection. After the tissue equilibrates with the 30% sucrose solution, it was placed into a mold containing Optimal Cutting Temperature compound (O.C.T) and then frozen on dry ice. Cryosections (10 to 15 µm thick) were cut and collected onto positively charged glass slides (Electron Microscopy Sciences). Sections were stored at -80 ºC before use. For immunolabelling, sections were first washed with 1x PBS and permeabilized with 0.5% Triton. Human anti-MUC17 (1:100; Abcam, ab122184) was used to stain for the murine structural homolog MUC3. The human anti-MUC17 targets the n-terminal side of the SEA domain (Thaher Pelaseyed, Gustafsson, Gustafsson, Ermund, & Hansson, 2013). Alexa-488-conjugated secondary antibody (1:400; ThermoFisher)) was applied to visualize the mucin labelling. Wheat germ agglutinin conjugated with Alexa Fluor 488 (WGA; TermoFisher, W11261) was used to label the glycocalyx layer. All samples were counterstained with fluorophore-conjugated phalloidin.

2.5.1.9 – Intravital microscopy

The anesthetized mouse was placed onto the microscopic stage and covered with a heating pad (37 ºC) to maintain body temperature. The externalized segment of the small intestine was constantly moistened by applying saline during imaging. Fixable fluorescent dextran conjugates of 3 or 2000 kDa in size (ThermoFisher, D-3305/D7137) were injected directly into the intestinal lumen via a small incision on the exposed small intestine. The externalized segment was then positioned onto a coverslip mounted on the stage above the objective and immobilized using custom-made specimen holders. The blood flow was assessed visually by using the eyepiece and only regions near blood vessels were imaged. A Nikon TiE inverted fluorescence microscope equipped with a Yokogawa CSU-21 spinning disk head and an Andor DU-897 camera was used for the experiment. Nikon Elements software was used for image acquisition and image analysis. At least three animals were imaged per condition tested.

2.5.2 – Structural correlates of outer hair cell electromotility

2.5.2.1 – Animals

All animal usage was in accordance with the Guide for the Care and Use of Laboratory Animals by NIH and approved by the Animal Care and Use Committee for the National Institute on Deafness and Other Communication Disorders (NIDCD ACUC, protocol #1215). The prestin-YFP mouse strain was obtained from Dr. Jian Zhou (Creighton University). This transgenic mouse strain expresses prestin with monomeric venus YFP fused to the C-terminus (Yamashita et al., 2015).

Cochlear tissues were collected from mice, rats and guinea pigs. For mice and rats, tissues were obtained from animals with ages post onset of hearing (on or later than P15). For guinea pigs, tissues were collected from adults (older than 1 month). Animals were euthanized by CO_2 asphyxiation and followed by decapitation. The temporal bones were removed from the skull and were either fixed for downstream processing or were placed into Medium 199 (ThermoFisher) for immediate fine dissection for direct freezing.

2.5.2.2 – Samples prepared for freeze-etching electron microscopy

The temporal bones were fixed with 2% glutaraldehyde for 2 hours and followed by microdissection to isolate the organ of Corti. Samples were then washed extensively with ddH_2O and fast frozen as described in section 2.5.1.3. Samples were transferred to a Balzers freeze-fracture machine and freeze-fracture was carried out at

-110 ºC and freeze-etched for 10 min at -100 ºC. The surfaces of freeze-etched samples were rotary shadowed with platinum/carbon and reinforced with a layer of carbon. The deposition angle of platinum/carbon was at 15º – 30º and the carbon backing was deposited from 90º. Replicas were cleaned with sodium hypochlorite, washed with distilled water and collected onto 300 mesh hexagonal copper grids (Electron Microscopy Sciences).

2.5.2.3 – Samples preparation for freeze substitution

For fixed samples, after the temporal bones were removed from the skull, they were placed into 2% glutaraldehyde. Holes were made on the cochlear bony capsule to facilitate fixative penetrance. Samples were fixed for 2 hours while rocking. Post-fixation, the cochlea was dissected to expose the organ of Corti. The samples were then slowly equilibrated with 30% glycerol for cryoprotection. Plunge freezing, freeze substitution and sectioning of cochlear tissues were carried out as described in section 2.5.1.4.

For unfixed samples, the temporal bones were placed into Medium 199 (ThermoFisher) and quickly microdissected. The isolated cochlear tissues were then transferred onto gelatin support that is mounted atop an aluminum specimen holder. The samples were rapidly brought against the surface of a liquid nitrogen-cooled sapphire block using a Life Cell CF-100 freezing machine. Samples were first transferred into liquid nitrogen then into the Leica Biosystems AFS for freeze substitution. The frozen tissues then underwent freeze substitution and sectioning as described in section 2.5.1.4.

2.5.2.4 – Data acquisition

Imaging of samples was carried out on a 200kV JEOL 2100 electron microscope equipped with an Orius 832 CCD camera (Gatan) or a OneView CMOS camera (Gatan) or on an 80 kV Zeiss EM 902 electron microscope equipped with an energy filter for zero-loss imaging and images were captured onto films. Film negatives were digitized using a Leaf 45 scanner (Leaf Systems). Dual-axis tilt series from -60º to +60º at 1º increments were acquired using SerialEM (Mastronarde, 2005) and processed using IMOD (Kremer et al., 1996). More than 15 sets of dual-axis tilt series were acquired, processed and analyzed.

Based on existing quantitative data, the lateral wall complex contains repeating structural components that are ~50 nm x ~50 nm (the spacing of actin filaments) (M. C. Holley et al., 1992), which indicates that to visualize such repeating structural feature in 3D within a section, a minimal volume of 50 nm x 50 nm x 50 nm would be required. To that effect, electron tomography was performed on ~70 nm thick sections of unfix, directly frozen and freeze-substituted guinea pig cochlear tissues to capture the 3D ultrastructure of the lateral wall complex and the repeating structural features within.

2.5.2.5 – Quantitative image analysis

The distance from the lateral plasma membrane (LM) to the lateral cisternae (LC), from the LM to the cortical lattice (CL), from the CL to the LC, the luminal width of the ER sheets within the LC, the distance between ER sheets within the LC, the distance between the LC ER membrane to the outer mitochondrial membrane (OMM) and the length of filaments connecting LC ER membrane to OMM were measured from tomogram slices in FIJI. Measurements were processed in Microsoft Excel (Microsoft) to generate the average and standard deviation.

The organization of membrane particles in the LM was analyzed using Gaussian blur in FIJI and fast Fourier transform (FFT) function in DigitalMicrograph (Gatan) or in FIJI. Gaussian blur is a low-pass filter where noise and high-frequency information are attenuated and low-frequency information is made more prominent (Haddad & Akansu, 1991). FFT produces a power spectrum of the image where the intensities of all the sine waves that make up the image are plotted in the reciprocal space. The power spectrum was filtered with Fourier spot masks to pass high-intensity spatial frequencies. Inverse-FFT was applied to the masked power spectrum to create the Fourier filtered real space images.

2.5.2.6 – Protein modelling of prestin

The transmembrane region (aa 74 – 504) of rat prestin protein (full length contains 744 amino acids, Uniprot: Q9EPH0) was submitted to the SWISS-MODEL web server using the crystal structure of SLC26Dg as the template (PDB: 5DA0)

(Geertsma et al., 2015; Gorbunov et al., 2014; Waterhouse et al., 2018). The resulting homology model of the transmembrane domain of prestin was then joined with the crystal structure of the cytoplasmic portion of rat prestin (PDB: 3LLO) in Chimera (UCSF) to produce a protein model of prestin (Pasqualetto et al., 2010). The orientation and positioning of the prestin protein model in a standard lipid bilayer were first determined using the PPM web server (Lomize, Pogozheva, Joo, Mosberg, & Lomize, 2012). The positional information was then submitted to CHARMM-GUI to build the lipid bilayer [226]. Visualization of the ribbon view of the prestin protein model, SLC26A9 (PDB: 6RTC) (Walter, Sawicka, & Dutzler, 2019), the dimeric protein model of the SLC26 family (PDBDEV_00000031) (Chang et al., 2019) and rendering of the prestin protein model in lipid bilayer was carried out in Chimera (UCSF) (Pettersen et al., 2004).

2.5.2.7 – Segmentation of tomograms

Tomograms from ultrathin sections of guinea pig outer hair cells were segmented. The tomographic volume was first processed in FIJI to create a stack of reversed images (using the invert function) and then filtered using 3D Gaussian blur (radius 4 by 4 by 4 pixels) to reduce image noise and to smooth the volume. The inverted and filtered volume was then imported into Amira (ThermoFisher) where electron densities were segmented by a combination of manual tracing and thresholding. The segmented electron densities were visualized using the isosurface module in Amira.

2.5.2.8 – Single particle averaging

Preliminary replica single particle averaging was done in collaboration with Dr. Benes Trus (NIH/CIT). The PIC system-III (NIH) was used to generate the three-dimensional surface plot of the projected average (Trus, Kocsis, Conway, & Steven, 1996).

2.5.2.9 – Light microscopy

The multilayered outer hair cell lateral wall complex was visualized with fluorescence microscopy. Post-onset of hearing prestin-YFP mice (on and after P15) were used for immunolabelling. The temporal bones were removed from the mouse and put into 4% paraformaldehyde to fix for 20 minutes. The cochleae were microdissected out and were permeabilized in 0.5% Triton X-100 in 1x PBS for 20 minutes. Samples were then blocked in 10% normal goat serum in 1x PBS (ThermoFisher) overnight at 4 ºC. Tissues were incubated with primary antibodies for 4 hours at room temperature then washed three times with 1x PBS. Fluorophore conjugated secondary antibodies were applied onto the samples for 1 hour and then rinsed with 1x PBS. Samples were also counterstained for actin using fluorophore-tagged phalloidin (ThermoFisher). Tissues were mounted in 1x PBS to preserve their native shape and imaged immediately after mounting. Samples were imaged using a Nikon Ti inverted fluorescence microscope equipped with a Yokogawa spinning-disk system and an Andor DU-888 camera. Images were acquired using Nikon Elements software. FIJI was used to produce single channel and composite images. FIJI was also used to generate line plots that show the distribution of fluorescence intensities. Microsoft Excel was used to normalize fluorescence intensities and to graph them.

Primary antibodies used: mouse COX IV (1:400; Abcam, ab33985), rabbit AQP11 (1:400; Covance, PB536) and mouse αII-spectrin (1:200; Abcam, ab11755).

Secondary antibodies used (ThermoFisher): goat anti mouse Alexa Fluor 405 (1:1000), goat anti mouse Alexa Fluor 647 (1:1000) and goat anti rabbit Alexa Fluor 568 (1:1000).

2.5.2.10 – Inclusion of prior data and the use of existing samples

The project on obtaining a comprehensive understanding of the structural basis of outer hair cell electromotility is an ongoing area of research within the Kachar lab. Former members of the lab and Dr. Kachar have accumulated samples on various stages of preparation, including tissue blocks, thin sections, and some raw micrographs. Since I started this project, I have been examining these orphan samples and preliminary raw micrographs in combination with the new samples I generated and images and tomograms I made. The analysis and quantification of the data were entirely performed by me. Representative images from the pool of micrographs that were analyzed are used in the figures.

Per the thesis proposal, plans were made for 2020 to generate additional replicas to obtain views of the outer hair cell lateral plasma suitable for freeze-etching electron tomography. I prepared a substantial amount of new frozen samples and made replicas. However, due to the pandemic, I could not examine all my samples. My efforts shifted to finish the analysis of data obtained prior to the pandemic.

Here is a list of data/images generated by former members, Dr. Kachar or a collaborator:

Figure 4.1 – Electrophysiological experiment was carried out by Dr. Gregory Frolenkov.

Figure 4.4, 5, 6, 9, and 13 – Original raw micrographs from the Kachar archive.

Figure 4.9 – Particle picking and preliminary single particle averaging was done by Dr. Benes Trus (NIH/CIT).

Chapter 3: Using the Intestinal Epithelium to Develop Freeze-etching Electron Tomography

3.1 – Introduction

3.1.1 – 3D imaging of freeze-etching replicas

The outer hair cell electromotile complex features extensive membrane-based components such as the transmembrane motor protein prestin and the pillar-shaped structure that connects cortical lattice to the lateral plasma membrane. While electron tomography on ultra-thin sections of the cryo-preserved, freeze-substituted organ of Corti helps with the elucidation of the 3D ultrastructure, it is not a robust technique for visualizing component within lipid bilayers and subtle membrane surface structural features. Previous studies using replica-based techniques have revealed that the outer hair cell lateral plasma membrane is densely populated with membrane particles (A. Forge, 1991; He et al., 2010; Kalinec et al., 1992). However, due to technical limitations, especially in the earlier studies (A. Forge, 1991; Kalinec et al., 1992), the relationship between the precise membrane particle organization, the topography of the lateral plasma membrane and outer hair cell electromotility was not explored further. Improvements in detector technology, tomographic reconstruction algorithms and increases in computational power over the last several decades have made examining the 3D topographical details of replicas possible.

To reexamine the structure-function relationship between outer hair cell lateral wall complex and electromotility using replica-based techniques, I need to first demonstrate that electron tomography on freeze-fracture/freeze-etching replicas can reveal the detailed 3D topography of membrane-based and membrane-associated cellular structures. Our lab routinely utilizes the intestinal epithelium and intestinal epithelial cell line as a model system because of the tissue's accessibility, abundance and microvilli at the apical surface of the intestinal epithelium share a high degree of similarity to the stereocilia of the auditory epithelium (Crawley, Mooseker, & Tyska, 2014; Crawley, Shifrin, et al., 2014; Schwander et al., 2010). While examining freeze-etching replicas of the mouse small intestine, I identified a prominent regular filamentous structural complex at the apical ends of microvilli. This apical surface feature corresponds to the intestinal glycocalyx (Ito, 1965), a polysaccharide-rich component decorating the apical surface of the intestinal epithelium. The glycocalyx is a ubiquitous cellular organization found across many different types of cell surfaces and in the intestine, the intestinal glycocalyx has been hypothesized to serve as a protective diffusion barrier and its composition has been characterized through genetics and biochemistry (Egberts, Koninkx, van Dijk, & Mouwen, 1984; Ito, 1974; Johansson & Hansson, 2016). However, precisely how this surface glycoprotein organization relates to its biological functions is not clear, as preserving and visualizing the intestinal glycocalyx is challenging using conventional TEM sample preparation techniques. Our lab has previously examined the bladder epithelium and was able to visualize the bladder glycocalyx using the freeze-etching replica technique but there was no in-depth ultrastructural analysis as elucidating 3D organizational information was not possible with 2D projections (Kachar et al., 1999). In this proof of concept study for freeze-etching electron tomography, we demonstrated that 3D information can be extracted by combining freeze-etching replicas and electron tomography. This technique helped unravel the relationship between the intestinal glycocalyx 3D arrangement and the protective diffusion barrier function.

3.1.2 – The Intestinal Glycocalyx: A Structure Difficult to Examine with Conventional Electron Microscopy Methods

The intestinal glycocalyx is a dominant cellular organization that blankets the apical surface of the intestinal epithelium (Figure 3.1a) (Sun et al., 2020) and it has been hypothesized to have wide-ranging functions including lubrication, digestion, regulating the intestinal microbiota, cell signaling and defense against pathogens (Johansson & Hansson, 2016; T. Pelaseyed et al., 2014). Genetic and biochemical analyses have revealed that the enteric glycocalyx is composed of glycoproteins and glycolipids with transmembrane mucins being the major constituent (Figure 3.1b & c) (T. Pelaseyed et al., 2014; Sun et al., 2020). Transmembrane mucins are single-pass transmembrane proteins rich in heavily glycosylated PTS domains (proline, threonine and serine) and the polypeptide backbone can reach up to 1 μm in length (Johansson, Sjovall, & Hansson, 2013). The extensive glycan decoration on transmembrane mucins suggests that individual membrane-tethered mucin would be shaped like a bottle brush that occupies a defined space and has limited ability to interact with other cellular components due to steric hindrance (Hattrup & Gendler, 2008). Ultrastructural examination of the intestinal glycocalyx using conventional electron microscopy revealed a dense filamentous meshwork approximately 0.1~0.5 μm in thickness that appears as a "fuzzy coat" atop the enteric microvilli (Ito, 1965, 1974). Moreover, intestinal tissue that underwent different post-fixation heavy metal staining protocols yields different glycocalyx morphology (Chevalier et al., 2017; Ito, 1974). The discrepancies in glycocalyx structural organization between different sample preparation protocols suggest that glycocalyx morphology is sensitive to chemical treatment and the appearance of the fuzzy coat may be an artifact (Figure 3.2). Ultrastructural data is also inconsistent with the biochemically predicted glycocalyx layer thickness, as the measured thickness of the glycocalyx layer in thin sections is 0.1~0.5 μm (Ito, 1974), which is less than the 0.5~1 μm thickness suggested by protein analysis (Johansson et al., 2013). The extensive glycosylation of transmembrane mucins makes the glycocalyx highly hydrophilic indicating that the shrinking of the glycocalyx layer in conventionally prepared samples may be the result of the dehydration step. The hydrophilic nature of the intestinal glycocalyx suggests that hydration level, in addition to post-fixation treatments, can change the morphology of the glycocalyx.

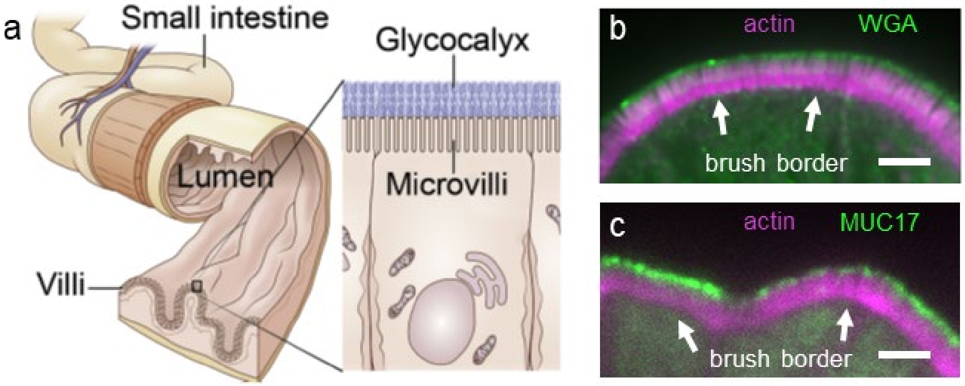

Figure 3.1 The enteric glycocalyx covers the apical surface of the intestinal tract. (a) Schematic diagrams showing the general organization of the small intestine and the molecular organization at the luminal surface. **(b)** Immunolabelling showing the glycocalyx layer situated atop the microvilli-rich brush border. Scale bars = 2 μm. Illustration by Ethan Tyler and Alan Hoofring, NIH Medical Arts Design Section.

Figure 3.2 (page 62) Organization of the intestinal glycocalyx is affected by conventional electron microscopy sample preparation techniques. A transmission electron micrograph showing an ultrathin section from glutaraldehyde-fixed, freeze-substituted, Lowicryl-embedded mouse small intestine. Black arrows point to the remnant of the glycocalyx layer, a thin coat atop the brush border. Scale bar = 500 nm.

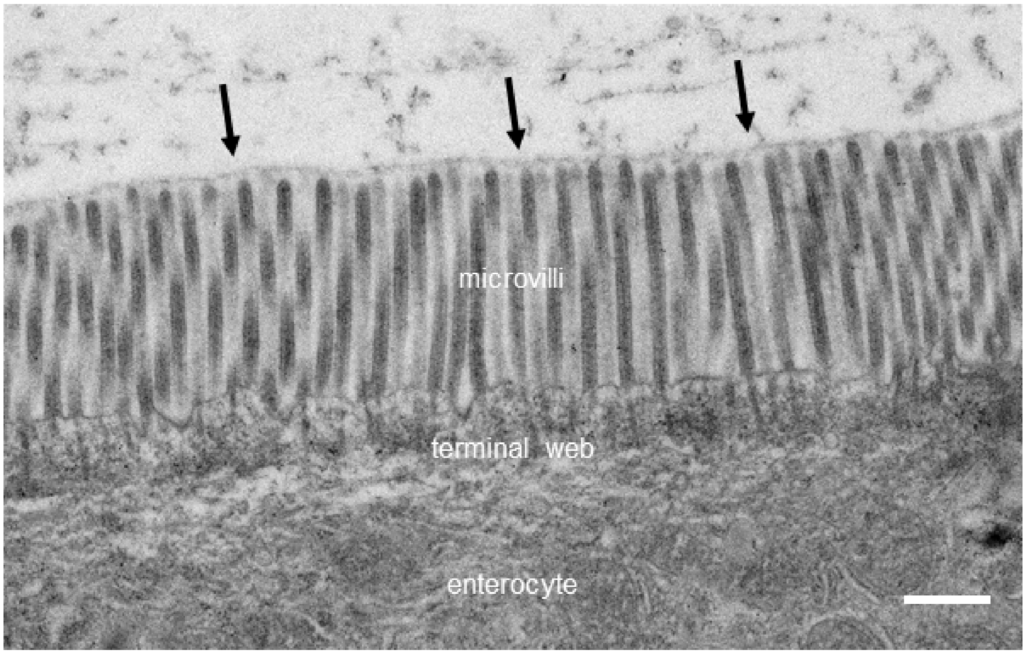

Figure 3.2 (legend on page 61)

The dense carbohydrate decoration within the intestinal glycocalyx creates a hydrophilic environment that is ideal for hydration, suggesting that under physiological conditions, the intestinal glycocalyx is highly hydrated. However, dehydration is required for conventional chemical-fixed, plastic-embedded samples. This removal of water likely altered the intestinal glycocalyx organization and caused the collapse of the filamentous meshwork. Based on previous studies from our lab and others (Kachar et al., 1999; Swift & Mukherjee, 1976), we know that replica-based cryogenic techniques such as freeze-etching can help preserve glycocalyx organization as the tissue experiences no additional post-fixation treatments and stays fully hydrated during sample preparation where water (in ice form) is only removed (through etching/sublimation) immediately before replicating the exposed ultrastructure. However, it is worth noting that not all freeze-etching replicas are created equal, as the amount of depth that is revealed by etching varies based on the duration of etching. In lightly-etched samples, a 2D array of filamentous proteins can be observed to project from the tips of microvilli but with minimal depth information (Swift & Mukherjee, 1976)[134]. This observation suggests that to examine the glycocalyx structure in full, deep etching of the sample will be needed.

In this study, I used the combination of freeze-etching replicas and electron tomography to reveal the detailed 3D organization of the intestinal glycocalyx (Sun et al., 2020). In addition, the ultrastructural data was complemented with intravital imaging of the glycocalyx in the intestinal lumen of live, anesthetized mice to better understand the physiology of this multifunctional layer *in vivo* (Sun et al., 2020).

3.2 – Results

3.2.1 – The intestinal glycocalyx is a uniform transcellular layer covering the microvilli-rich apical surface of enterocytes

To preserve and visualize the ultrastructure of the intestinal glycocalyx, freeze-etching replicas were generated from the deep-etched apical surface of the mouse small intestine. Deep-etching replicas reveal that the glycocalyx is a fully extended dense filamentous meshwork when the sample remains hydrated during preparation and experiences no post-fixation heavy metal treatment (Figure 3.3a). The measured thickness of the glycocalyx layer is 1.0 ± 0.1 μm (*n* = 53), consistent with the predicted dimension from protein analysis (Johansson et al., 2013). The fully extended meshwork is in stark contrast to the conventionally prepared samples that showed a 0.1~0.5 μm thick fuzzy coat (Ito, 1974). The intestinal glycocalyx appears to be a continuous network (Figure 3.4), consistent with the mucin labelling (Figure 3.1c). The glycocalyx layer is composed of columnar filaments that emerge from the very distal ends of enterocyte microvilli (Figure 3.3a & f). The number of filaments that projects from the tips of microvilli varies, with an average number of 7.1 ± 1.5 (*n* = 54) filaments per microvilli. These filaments are also distinct from horizontal linkers that connect the microvilli (Figure 3.3e). The glycocalyx filaments exhibit large-scale inter-filament interactions, with anastomoses and branching taking place from near tips of the microvilli to the luminal interface (Figure 3.3a, b & e). The extensive filament-filament interactions result in a sieve-like structure with varying mesh sizes (Figure 3.3b & c) with the maximal distance between neighboring filaments being 29 ± 10 nm (*n* = 101). This densely intertwined meshwork is observed in both glutaraldehyde-fixed and unfix mouse small intestine, suggesting that inter-filament interactions are not an artifact of sample processing (Figure 3.3a, b & e).

Figure 3.3 (page 66) The intestinal glycocalyx is a dense filamentous network that covers the microvilli-rich brush border. (a) Electron micrograph of a freeze-etching replica showing different layers of structures at the apical portion of an enterocyte. **(b)** A close-up view of the rectangle region in **(a)**. **(c)** This filamentous network has a mesh size of 29 ± 10 nm (*n* = 101). **(d)** High-magnification view of the microvilli-glycocalyx interface. Objects of varying sizes can be found within the dense network (arrow and arrowhead). **(e)** A micrograph showing of a freeze-etching replica from unfixed tissue. Glycocalyx filaments emerge exclusively from the very distal ends of microvilli and are distinct from the lateral connectors (arrowhead). **(f)** Single 2 nm tomographic slice through a microvilli-glycocalyx interface showing that filaments project from the microvilli membrane (arrow), consistent with transmembrane mucins. Scale bars: **(a)** = 1 μm; **(b)** = 200 nm; **(d & e)** = 100 nm; **(f)** = 50 nm.

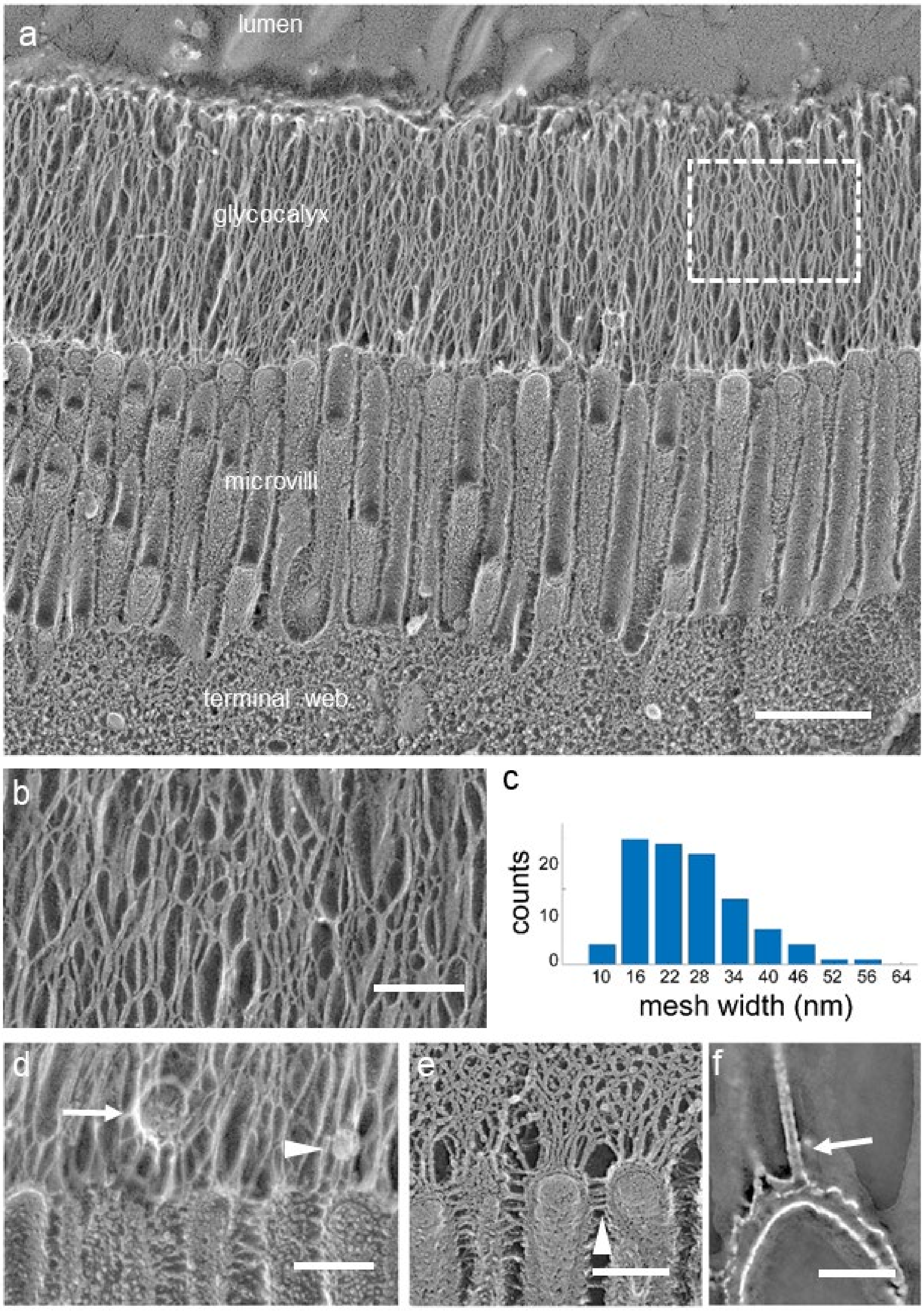

Figure 3.3 (legend on page 65)

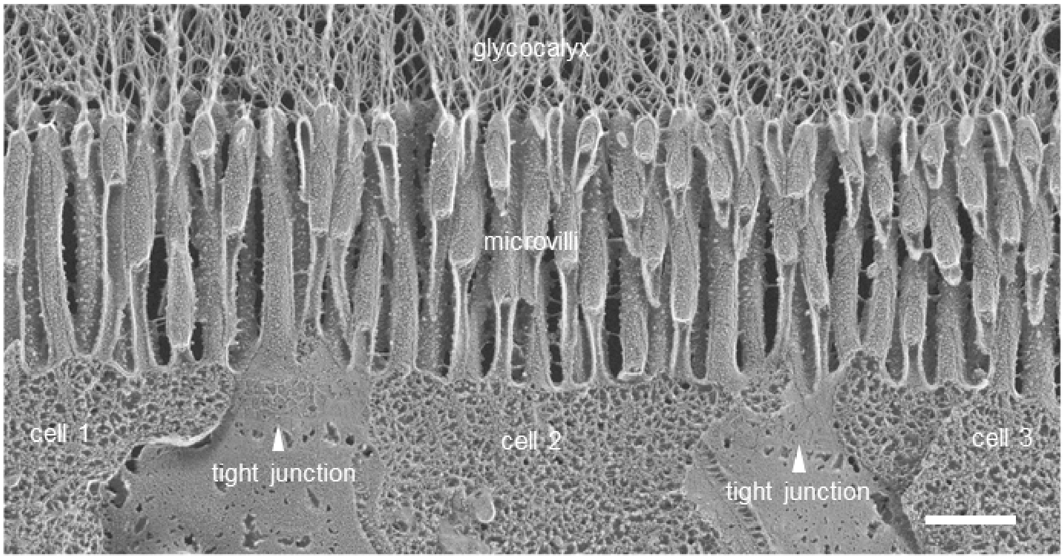

Figure 3.4 The intestinal glycocalyx is a transcellular organization. An image of a freeze-etching replica showing that the intestinal glycocalyx organization extends across multiple cells that are closely connected via tight junctions (arrowheads). The glycocalyx network does not show a definitive boundary between cells. Scale bar = 500 nm.

3.2.2 – Extensive inter-filament interactions result in a complex 3D meshwork

The 2D projection images of deep-etching replicas of the apical surface of the mouse small intestine reveal many details that were previously not observed with conventional TEM. However, the 3D organizational information of the glycocalyx cannot be fully extracted from conventional 2D projections. To elucidate how the glycocalyx filaments form a 3D structure, I utilized electron tomography on these replicas to visualize the 3D topography of the deep-etched glycocalyx. A stereoscopic image derived from a reconstructed tomogram of the intestinal glycocalyx showed clearly the 3D nature of the glycocalyx layer (Figure 3.5a). Glycocalyx filaments from deeper regions of the replica were observed to make contact with filaments at shallower regions, indicating that inter-filament interactions occur in all three dimensions (Figure 3.5a, arrowheads). Moreover, tomographic volumes from deep-etching replicas allow detailed examination of filament-filament interactions. Over the length of an individual glycocalyx filament within the meshwork, it can experience no interactions, make contact with a neighboring filament or it can branch and fuse (Figure 3.5b, c, & d). The combination of deep-etching replicas and electron tomography showed that lateral interactions between columnar filaments within the intestinal glycocalyx helped establish a 3D network.

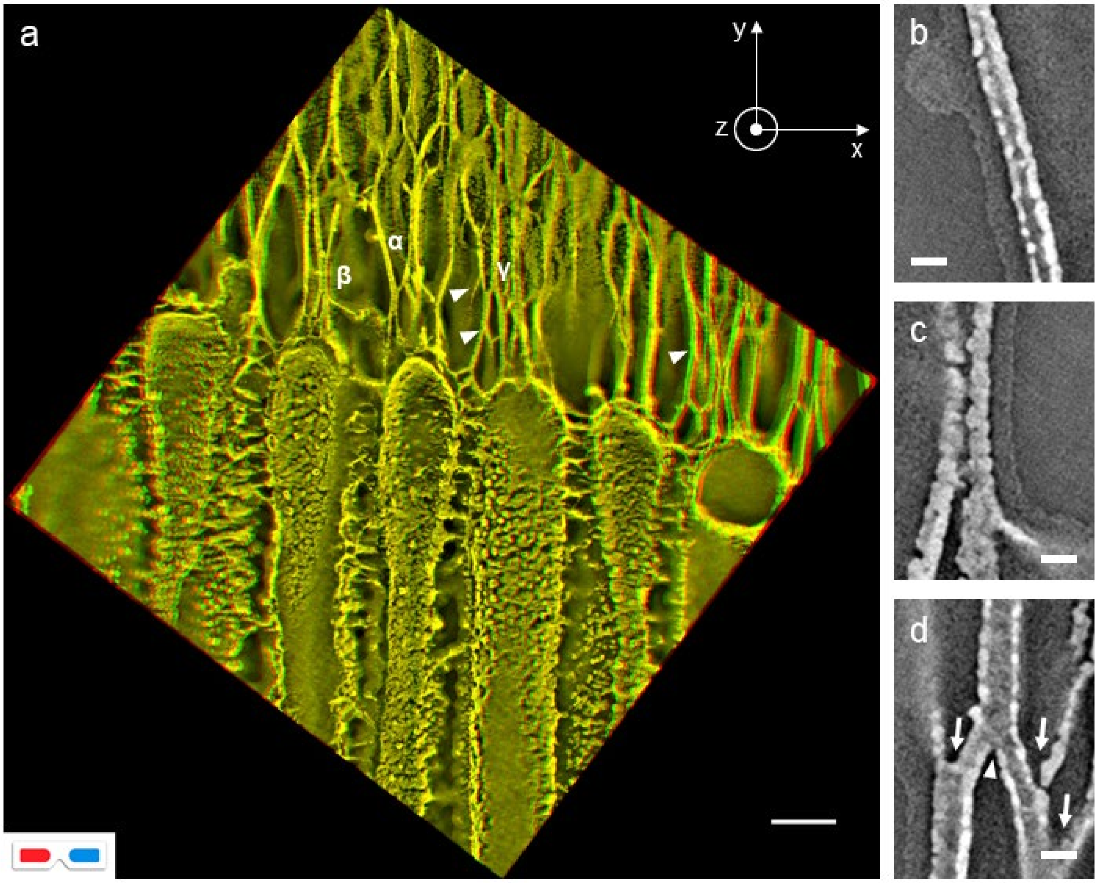

Figure 3.5 Electron tomography of freeze-etching replicas reveals that the intestinal glycocalyx is a complex 3D meshwork. (a) A stereoscopic image derived from a reconstructed tomogram showing a 3D meshwork. Arrowheads point to inter-filament interactions in the z-direction. **(b – d)** Tomographic slices through a reconstructed volume showing different types of inter-filament interactions. **(b)** Location α in **(a)**, showing a stretch of glycocalyx filament without lateral interaction. **(c)** Location β in **(a)**, showing two filaments having side-to-side contact. **(d)** Location γ in **(a)**, showing that filaments can branch (arrows) and fuse (arrowhead). Scale bars: **(a)** = 100 nm; **(b – d)** = 10 nm.

3.2.3 – Segmentation helped refine ultrastructural details of glycocalyx filaments

Electron tomography of deep-etching replicas enabled the examination of the 3D topography of the glycocalyx layer and allowed for more accurate qualitative analysis (Figure 3.5 & 3.6a). However, a replica is only a cast of the surface topography of the specimen. The fidelity of the replication is influenced by several factors, such as replica thickness and crystallization of metal atoms (Krystofiak, Heymann, & Kachar, 2019). Replica thickness artificially inflates the size of the ultrastructure while the crystallization of metal atoms can mask subtle changes in topography. Segmentation of freeze-etching replicas can partially overcome these intrinsic limitations. By carefully tracing the replica through a tomographic volume, the cast of the underlying biological structure is visualized and the interior surface of the replica can be examined (Figure 3.6b & c). The inner replica surface provides a more authentic rendering of the surface topography and contains more accurate dimensions than the conventional 2D projection views of a replica as it represents the impression left by the underlying ultrastructure. Filament diameter was measured from segmented replicas to be 5.3 ± 1.3 nm ($n = 51$) with a range between 3 to 15 nm, suggesting that these filaments may contain one or more mucin strands (Figure 3.6d). The combination of electron tomography, freeze-etching replica and segmentation enabled more accurate quantification of the biological material that was replicated.

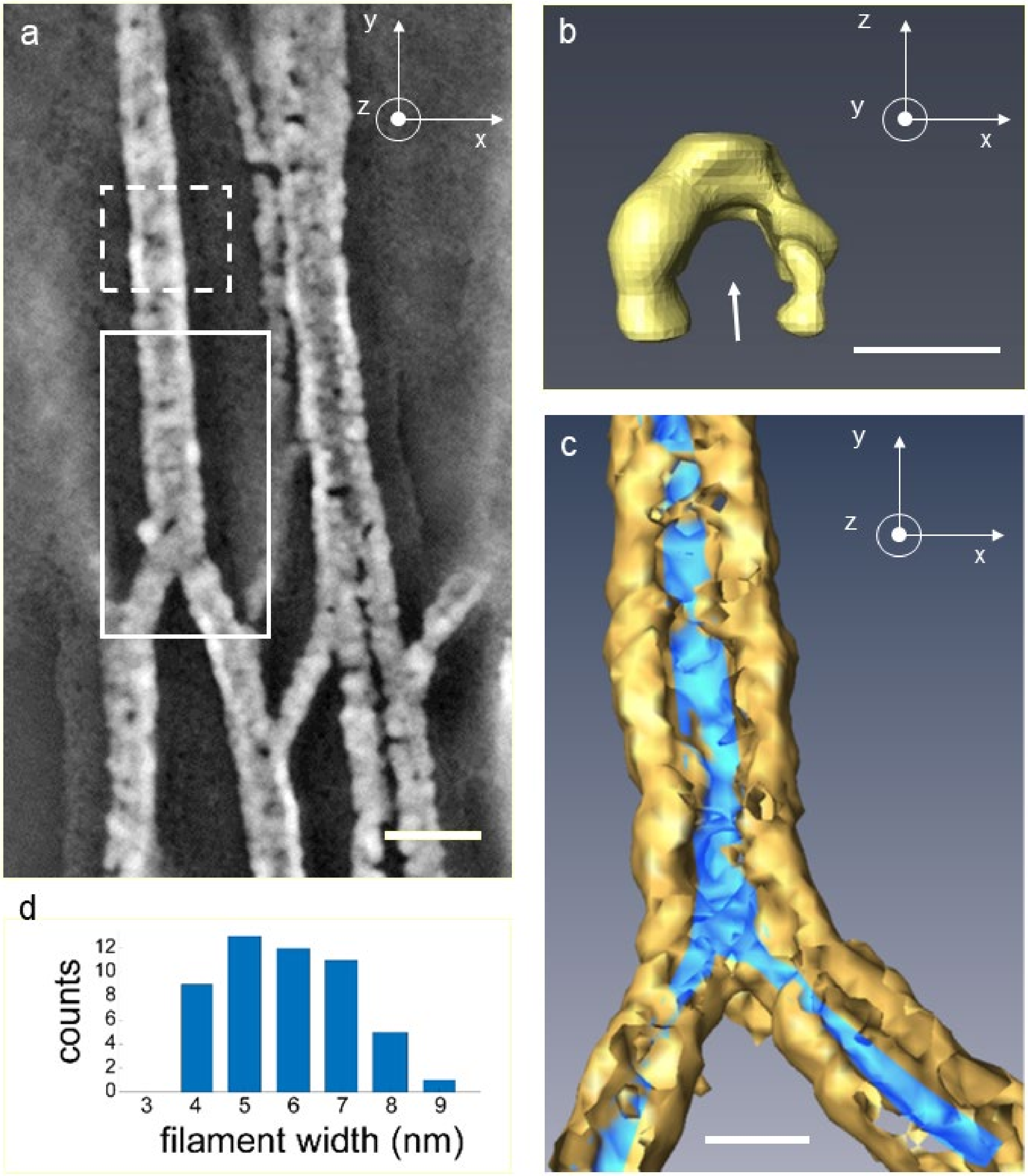

Figure 3.6 (legend on page 72)

Figure 3.6 (page 71) Morphology of glycocalyx filaments revealed by electron tomography and segmentation. (a) A close-up view of location γ in **Figure 3.5a**. The dashed and solid line boxes are regions that were segmented, respectively in **(b)** and **(c)**. **(b)** Segmentation showing a XZ-plane view of the filament. The metal cast is in gold and the white arrow points to the interior space previously occupied by the glycocalyx. **(c)** Segmentation showing a XY-plane view of two filaments fusing. The metal cast ishighlighted in gold and the interior space is highlighted in blue. **(d)** Distribution of filament width after accounting for the thickness of the replica. Mean thickness: 5.3 ± 1.3 nm (*n* = 51). Scale bars: **(a)** = 20 nm; **(b & c)** = 10 nm.

3.2.4 – Planar organization at the intestinal lumen-glycocalyx interface

The lateral view of the intestinal glycocalyx showed that the columnar filaments within the meshwork are uniform in length and terminate in the same region (Figure 3.3a). While tomographic data (Figure 3.5) showed that filament organization is the result of extensive lateral filament-filament interactions, the arrangement of the termini of these filaments remains unresolved. The previously unseen structural organization at the intestinal lumen-glycocalyx interface was visualized in areas where the etching direction was perpendicular to the apical surface of the intestinal tissue. The termini of the uniform columnar glycocalyx filaments appeared to organize into a plane (Figure 3.7a). The terminal ends of glycocalyx filaments were regularly spaced globular structures that are 10.2 ± 1.2 nm (*n* = 82) in diameter (Figure 3.7b). While the size of these terminal globular structures was consistent, they can be composed of an individual or multiple glycocalyx filaments (Figure 3.7c & d). These glycocalyx termini also appeared to resist etching (Figure 3.7b), most likely due to the extensive glycosylation found on mucins (Figure 3.7b) (Hattrup & Gendler, 2008). The planar arrangement of glycocalyx filament termini exhibits variations from hexagonal order to liquid packing (Figure 3.7 e – g), suggesting that the glycocalyx layer is dynamic. Accurate quantification of the spacing between glycocalyx filament termini was done by collecting 3D coordinates of the individual terminal within a large tomographic volume. These coordinates were then fed into a custom MATLAB script to calculate the average nearest neighbor distance (32.0 ± 7.9 nm; *n* = 1188) and a histogram showing the distribution of termini spacing (Figure 3.7h).

Figure 3.7 (page 74) Glycocalyx filament termini coalesce to form regularly spaced globular tips. (a) A Freeze-etching micrograph showing the luminal view of the glycocalyx layer. Glycocalyx filaments terminate into globular structures that form a well-patterned plane. **(b)** A close-up view of the globular structures shows that they are surrounded by a radial gradient of platinum deposition (dashed line circle) indicating resistance to etching. **(c)** An oblique view showing how filaments terminate into a single globular structure (arrowheads). **(d)** High-magnification view showing that multiple filaments (arrowheads) converging before forming the globular structure. **(e – g)** Glycocalyx filament termini exhibit packing ranging from hexagonal **(e & f)** to liquid **(g)**. FFT (inset of **e**) indicating hexagonal organization. **(h)** Nearest neighbor distance distribution of termini with Gaussian fitting. Mean: 32.0 ± 7.9 nm (*n* = 1188). Scale bars: **(a)** = 100 nm; **(b)** = 20 nm; **(c)** = 50 nm; **(d)** = 20 nm; **(e – g)** = 100 nm.

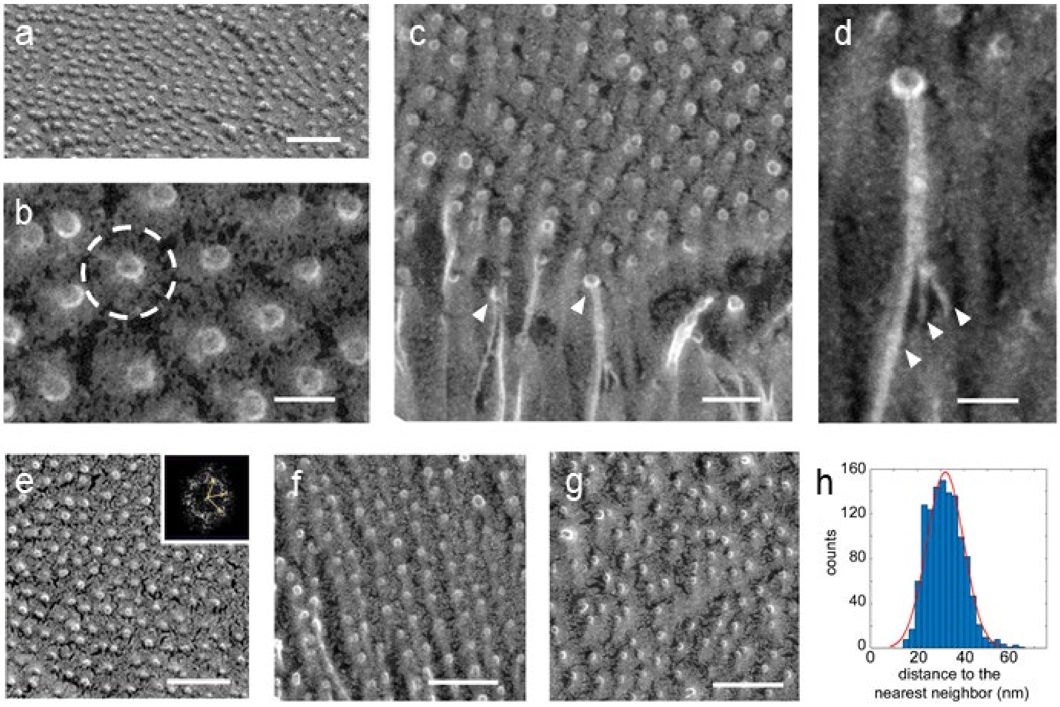

Figure 3.7 (legend on page 73)

3.2.5 – Protective filtering properties of the intestinal glycocalyx

The structural organization of the intestinal glycocalyx, visualized through the combination of electron tomography and freeze-etching replicas, contains a uniform 3D sieve-like network made of densely intertwining glycocalyx filaments (Figure 3.3a, 3.5a). Such structural arrangement suggests that the intestinal glycocalyx likely behaves as a size-exclusion filter that allows a selection of small molecules access to the apical surface of the enterocytes while keeping larger and potentially harmful objects away. Whether protective filtering properties are part of the intestinal glycocalyx's physiological functions are not clear. Electron microscopy-based methods were only capable of providing a static account of the intestinal glycocalyx, making it difficult to interpret how the molecular architecture relates to its proposed functions. To examine whether the ultrastructural assessment of the intestinal glycocalyx relates to the proposed protective diffusion barrier function, a dextran-based macromolecular diffusion assay was performed. Moreover, how the static ultrastructural information translates to intestinal glycocalyx behaviours under physiological conditions was investigated in collaboration with Dr. Seham Ebrahim and Dr. Roberto Weigert of National Cancer Institute's Laboratory of Cellular and Molecular Biology utilizing intravital imaging [141], a live imaging method pioneered by their lab.

Quantitative analysis of the intestinal glycocalyx has shown that the mesh size of the glycocalyx layer based on filament termini spacing and inter-filament distance is ~30 nm, indicating that objects < 30 nm would readily pass through the dense network while objects >30 nm would be impeded. To examine the porosity of the intestinal glycocalyx, two different molecular weight fluorescent dextrans, 2000kDa and 3kDa with respective radial dimensions of ~27 nm and ~1.2 nm [129], were applied to mouse small intestinal tissues processed with the same conditions of the freeze-etching experiments. The 3kDa fluorescent dextran was observed to readily travel across the glycocalyx layer to reach the brush border while the passage of the 2000kDa dextran was hindered by the surface coat (Figure 3.8a & b).

To investigate how the intestinal glycocalyx behaves *in vivo*, intravital microscopy was employed to directly image the intestinal lumen of live, anesthetized reporter mice expressing mTomato at the plasma membrane. The surgically exposed small intestine was injected with 3kDa fluorescent dextran and live imaging showed that the small-sized dextran molecules traveled across the glycocalyx layer and filled the brush border (Figure 3.8c & d), corroborating the ultrastructural data and the diffusion assay. The injection of the fluorescent dextran created a wound at the injection site that led to red blood cells entering the intestinal lumen. The presence of erythrocytes in the intestinal lumen presented a unique opportunity to evaluate how the intestinal glycocalyx offers protection to the intestinal epithelium. Erythrocytes flowing in the intestinal lumen were observed to glide along the intestinal tract and never directly come into contact with the apical surface of the intestinal epithelium (Figure 3.8c & d), suggesting that the glycocalyx layer acts as a physical barrier. In addition, when luminal space narrows, red blood cells can be seen to deform while passing through the channel but still maintain a minimum distance away from the apical intestinal surface, indicating that the intestinal glycocalyx may be a deformable structure (Figure 3.8c). To confirm the deformability of the glycocalyx organization, freeze-etching of unfixed small intestinal tissues was performed. The lumen of the unfixed small intestine was fully occupied with luminal contents that were in direct contact with the intestinal glycocalyx and the meshwork was compressed (Figure 3.8d). In the fixed and extensively washed samples, there was no luminal content and the glycocalyx layer was observed to be fully extended (Figure 3.3a). Observations from live imaging and freeze-etching replicas of fixed & unfixed samples suggest that the meshwork undergoes deformation *in vivo* to minimize physical disruption to the underlying apical surface of the intestinal epithelium in addition to acting as a size-exclusion filter.

Figure 3.8 (page 78) Confocal microscopy reveals that the intestinal glycocalyx is a deformable filter. (a) Confocal image of the brush border of a fixed intestinal segment exposed to fixable fluorescent dextrans with different molecular weights. 3 kDa dextran (magenta) has a Stokes radius of ~1.2 nm and permeates the glycocalyx layer (gly) and reaches the microvilli (mic). 2000 kDa dextran (green) has a Stokes radius of ~27 nm and is excluded from both layers. **(b)** Fluorescent intensity line plot along the dashed line in (a) showing the distribution of the different sized dextrans from the cytoplasm (cy) to the lumen (lu). **(c – d)** Intravital microscopy images showing live mouse small intestine filled with 3 kDa fluorescent dextran. Red blood cells introduced during surgical incision are not able to make contact with the microvilli layer due to the presence of the glycocalyx. **(e)** Image from freeze-etching replica of unfixed, directly frozen mouse small intestine showing that the glycocalyx is flexible. Yellow arrows point to local deformation. Scale bars: **(a)** = 2 μm; **(c & d)** = 5 μm; **(e)** = 500 nm.

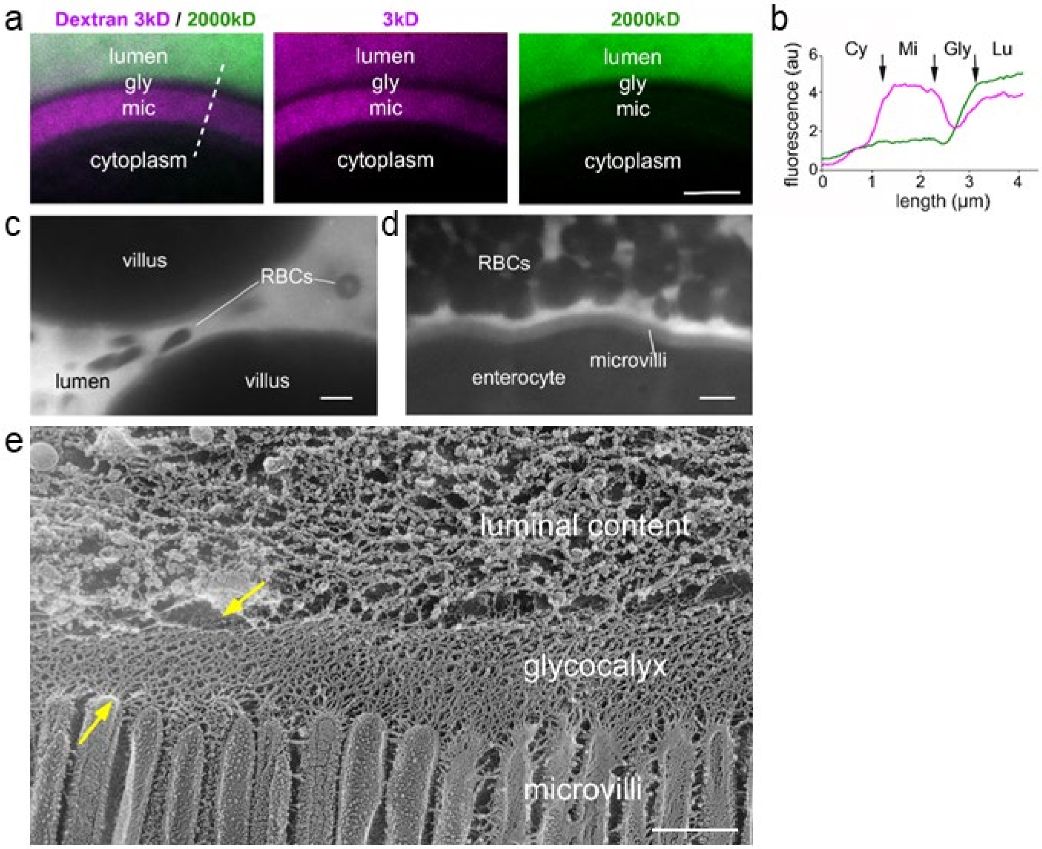

Figure 3.8 (legend on page 77)

3.3 – Summary and discussion

The primary function of the intestinal glycocalyx has been suggested to act as a size-selective diffusion barrier, preventing harmful particles such as bacteria to interact with the enterocyte plasma membrane (Egberts et al., 1984; T. Pelaseyed et al., 2014). While the main constituents of the intestinal glycocalyx, transmembrane mucins, are known, how the ultrastructural organization and the resulting architecture affect the porosity and penetrability of the glycocalyx layer remain unresolved. The main challenge is understanding the relationship between glycocalyx structure and function. However, the ultrastructural details of glycocalyx are severely disrupted in conventional transmission electron microscopy as the native structure depends on hydration. Moreover, the extensive glycosylation of the proteins that make up the glycocalyx makes it default to infer information about their structures and protein-protein interactions from protein sequence information. By combining freeze-etching and electron tomography, I was able to preserve and visualize the three-dimensional intestinal glycocalyx network and resolve its nano-scale organization. In addition, fluorescent dextran permeability assay and intravital imaging were utilized to assess the porosity and penetrability of the glycocalyx layer.

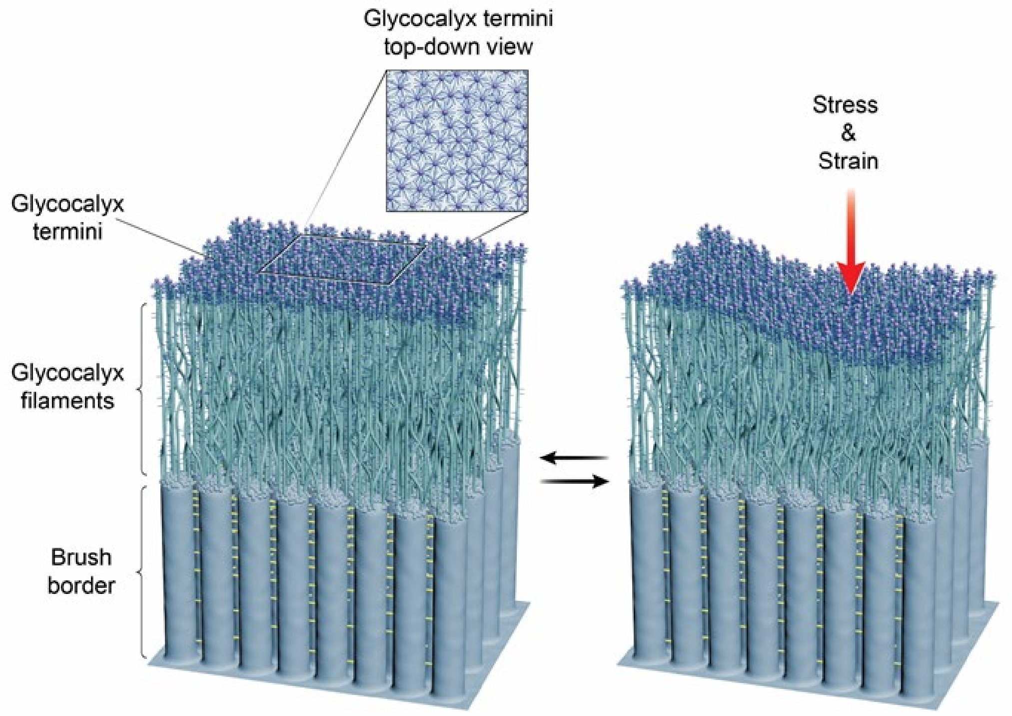

Figure 3.9 A model of the intestinal glycocalyx architecture. Schematics of the intestinal glycocalyx based on freeze-etching replicas and intravital imaging data. The intestinal glycocalyx is composed of columnar filaments emerging at the tips of microvilli and form a dense meshwork through lateral interactions that results in a deformable filter. Images are drawn to scale. Illustration by Ethan Tyler and Alan Hoofring, NIH Medical Arts Design Section.

Our data indicate that the intestinal glycocalyx is composed predominantly of columnar filamentous glycoproteins that laterally interact to form a 3D meshwork with an average pore size of 29 nm. These filamentous glycoproteins terminate into globular structures with strong water retention. These globular termini form a plane facing the intestinal lumen and have an average spacing of 32 nm. The spacing between glycocalyx filament termini and the ability to withstand deep etching may be due to the extensive glycosylation. Transmembrane mucins, major constituents of the intestinal glycocalyx, undergo extensive *O*- and *N*-glycosylation during protein synthesis and post-translational modification with sialic acids (*N*-acetylneuraminic acids) being a common modification at the terminal positions of glycans (Corfield, 2018; Varki, Schnaar, & Schauer, 2015). Sialic acids have been shown to play a critical role in water retention and are involved in the long-range structuring of water molecules (Espinosa-Marzal et al., 2013). This information suggests that glycocalyx termini may have more extensive glycosylation than along the length of the filament. This stronger sugar-water interaction likely reduced the rate of water sublimation at the terminal regions compared to the filament-body regions (Figure 3.3b, Figure 3.7b). Furthermore, the dense glycosylation introduces steric hindrance and causes transmembrane mucins to be negatively charged (Hattrup & Gendler, 2008), suggesting that structural interferences and charge repulsion may contribute to the spacing between filament termini and different types of inter-filament interactions. In addition, glycosylation at filament termini likely affects the packing of these globular structures as the planar organization exhibits a range of termini packing from crystalline to liquid. These spatial arrangements are consistent with a molecular sieve that prevents objects with a Stokes radius greater than 30 nm from having direct access to the apical surface of the enterocytes.

While our ultrastructural data strongly support the intestinal glycocalyx functions as a size-selective diffusion barrier, whether these static accounts of the glycoprotein meshwork are physiologically relevant is unclear. To better understand the physical properties of the intestinal glycocalyx *in vivo*, we used intravital imaging, which allowed direct visualization of the lumen of mouse small intestine in live animals. Red blood cells that were incidentally released into the lumen during the surgical opening of the small intestine were seen to glide along the intestinal epithelium without coming into direct contact with the brush border, indicating that under physiological conditions, the intestinal glycocalyx is dynamic and flexible (Figure 3.8).

The combination of freeze-etching, electron tomography and intravital imaging helped establish a renewed structural understanding of the intestinal glycocalyx (Figure 3.9) and outlined a blueprint for future investigations on how the structure of this surface coat correlates with intestinal physiology.

Chapter 4: Structural Correlates of Outer Hair Cell Electromotility

4.1 – Introduction

4.1.1 – Improving the understanding of the structural basis of outer hair cell electromotility

The elucidation of the structural and molecular basis of outer hair cell electromotility and how this unique motor response is involved in cochlear amplification has been an active area of research across multiple disciplines since the initial observations that mammalian outer hair cells are capable of undergoing axial length changes (Kachar et al., 1986). Ultrastructural data has revealed that the lateral wall region of outer hair cells contains a highly specialized trilaminar cellular organization composed of the prestin-rich lateral plasma membrane, an actin-spectrin based cortical lattice and a single layer or multilayered smooth endoplasmic reticulum system known as the lateral cisternae (He et al., 2010; M. C. Holley et al., 1992; Kachar et al., 1986; Kalinec et al., 1992; Saito, 1983). Electrophysiological approaches (Joseph Santos-Sacchi et al., 2017) have elucidated key biophysical features of outer hair cell electromotility including identifying the characteristic nonlinear capacitance associated with prestin activities, demonstrating that the motor response is driven by the changing membrane potential, the regulation of prestin activity by intracellular chloride and prestin behaving as an incomplete anion transporter. Biochemistry and molecular genetics methodologies helped identify the motor protein prestin (J. Zheng et al., 2000), generate different prestin variants for functional evaluation (Homma et al., 2013) and elucidate potential interacting partners of prestin (Homma et al., 2010).

Recent advancements in the molecular understanding of outer hair cell electromotility have been driven by innovative sequencing technologies that allow for cell-type specific transcriptome analysis at the single-cell level (Burns, Kelly, Hoa, Morell, & Kelley, 2015; Chessum et al., 2018). In addition, continual improvement of electrophysiological methodologies and recording instruments helps refine biophysical measurements of the outer hair cell electromotile responses. In contrast, progress at the ultrastructural front has been lagging due to challenges associated with preserving and visualizing the delicate and limited cochlear tissue. The elucidation of the molecular basis of electromotility and how the concerted activity of components within the electromotile machinery results in measurable biophysical events depend on being able to accurately localize the molecular building blocks and detail their interactions. However, obtaining accurate localization and inter-component interaction data may be difficult using conventional TEM as it is hard to differentiate physiologically relevant ultrastructural information from artifacts associated with chemical fixation and dehydration. Suboptimally prepared cochlear tissues may lead to incomplete or inaccurate structure-function relationship assessment and improper correlation of electrophysiological and ultrastructural data.

To understand how structural data influences functional interpretation, we can examine the two major biophysical models for outer hair cell electromotility. The prevailing area motor model suggests that the area of the plasma membrane changes when molecular structures in the plane of the lateral plasma membrane undergo membrane potential induced conformational changes (Iwasa, 1994). Freeze-fracture/freeze-etching data have revealed that the lateral plasma membrane contains a dense array of particles where the motor protein prestin is the dominant constituent (He et al., 2010; Kalinec et al., 1992). The tight packing of prestin in the lateral plasma membrane suggests that any small change in its molecular structure, when occurring *en masse*, could change the surface area of the plasma membrane. On the other hand, the competing model argues that the area motor model is too simplified and did not take into account contributions from the cortical lattice and the underlying lateral cisternae. The membrane-bending model proposes that the thin plasma membrane becomes flexible when electrically stimulated and the integration of the cortical lattice to the lateral plasma membrane through pillar-shaped structures creates constrain points that causes local membrane double leaflets to experience differential stress that results in the bending or curving of the membrane (Raphael, Popel, & Brownell, 2000). This membrane curvature then deforms the spectrin crosslinkers within the cortical lattice that leads to the observed whole cell length change. The ultrastructural observation that the lateral plasma membrane appears ruffled between pillars was used to support the membrane-bending model of electromotility (M. C. Holley et al., 1992). However, the images referenced were conventionally prepared samples and we cannot rule out that the observed membrane folding may be artifacts from chemical fixation, dehydration and plastic embedding.

It is well established that turgor pressure (internal pressure) and membrane tension affect both outer hair cell electromotility and the characteristic nonlinear capacitance (Iwasa, 1993; J. Santos-Sacchi, 1991; Shehata et al., 1991). Outer hair cells have been shown to possess a slight positive intracellular pressure and that decrease in this turgor pressure leads to a reduced evoked response or the loss of electromotility (Chertoff & Brownell, 1994; J. Santos-Sacchi, 1991; Shehata et al., 1991). The electrically evoked motile response being attuned to the turgor pressure and membrane tension indicates that outer hair cell electromotility operates under very specific physiological conditions and the fine structural integrity of the outer hair cell lateral wall is critical (Figure 4.1). Therefore, accurate characterization of the relationship between the trilaminar cellular organization and outer hair cell electromotility would depend on preserving the structural integrity of the entire lateral wall nanoarchitecture during sample preparation. Vitrification of unfixed cochlear tissue in combination with freeze-substitution and low-temperature embedding offers a means to mitigate artifacts associated with conventional sample preparation and provides an opportunity to examine cochlear tissue in a near-native state (Figure 4.2). In vitrified regions, where the ice is amorphous, the lateral plasma membrane and the underlying structures are well preserved (Figure 4.2a & c). On the other hand, the lateral wall organization is disrupted by crystalline ice in poorly frozen areas (Figure 4.2b). In the transition zone between good to bad freezing, subtle changes in morphology can readily be noticed, suggesting that the native lateral wall organization is a delicate structure (Figure 4.2b). Hence, preserving and visualizing outer hair cells in a near-native state is of paramount importance for the accurate characterization of the molecular architecture of the outer hair cell lateral wall complex and in understanding how this multilayered organization enables outer hair cell electromotility.

To elucidate the detailed 3D nanoarchitecture that underlies outer hair cell electromotility in a near-native state, electron tomography was performed on ultrathin sections of fast frozen, freeze-substituted unfixed cochleae. However, such a technique is not suitable for visualizing membrane-based or membrane-associated components within the lateral wall complex. To overcome this limitation, freeze-fracture/freeze-etching replicas were generated to help visualize topographical details of membrane-based and membrane-associated structural elements such as the transmembrane protein prestin. The combination of electron tomography of freeze-substituted unfixed samples with freeze-etching replicas outlined a structural blueprint that details individual constituents and their arrangements within the outer hair cell lateral wall organization that underlies electromotility (Figure 4.3).

Figure 4.1 (page 89) Outer hair cell structural integrity is important for proper electromotility. (a – d) Isolated guinea pig outer hair cell imaged from normal turgor pressure **(a)** through a series of turgor pressure reduction **(b – d)**. **(e)** Prestin operation remains normal as evident by the invariance of its signature nonlinear capacitance measurements across different cell turgor states. **(f)** The ability for outer hair cell to undergo length changes is disrupted when cell turgor is reduced.

Figure 4.2 (page 89) Preserving and visualizing the outer hair cell lateral wall organization in a near-native state with cryogenic methods. (a – c) Low to high-magnification micrographs of ultrathin sections from unfixed guinea pig cochlear tissue that was slam-frozen, freeze-substituted and low-temperature embedded. **(a)** A low-mag view showing the slam-frozen tissue. Below the white dashed line is the poorly frozen zone as indicated by the rough texture. Black arrowhead indicates the direction of freezing. White arrowhead points to the stereocilia. **(b)** A higher magnification image showing the good freezing area (above the yellow dashed line), a transition zone between good and bad freezing (between two dashed lines) and a poorly frozen region (below the white dashed line). The good freezing area has a smooth texture and well-preserved lipid bilayers (white arrowheads). **(c)** Close-up view of a well-preserved area. Cristae of mitochondria are also well-preserved (white arrow). The lateral plasma membrane remains consistent even in a region without the lateral cisternae (yellow arrowheads). OHC: outer hair cell; LM: lateral plasma membrane; CL: cortical lattice; LC: lateral cisternae. Scale bars: **(a – b)** = 1 µm; **(c)** = 100 nm.

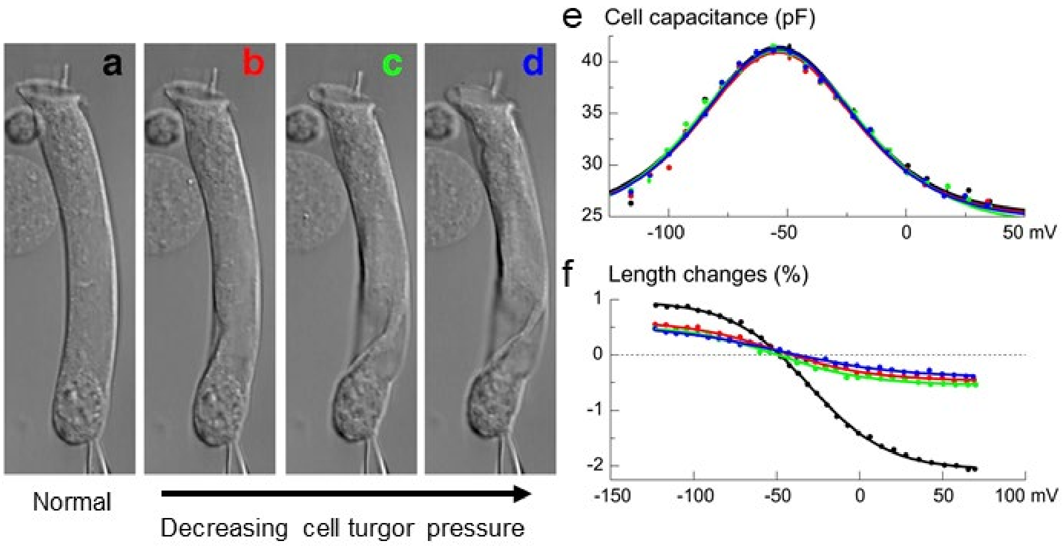

Figure 4.1 (legend on page 88)

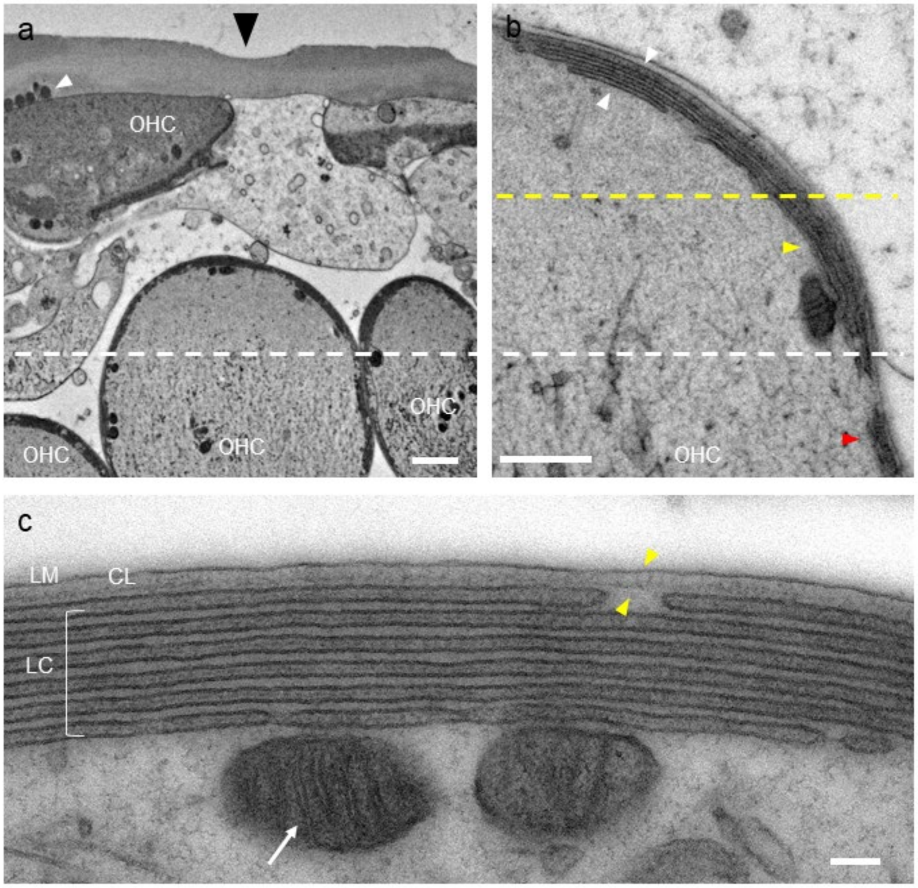

Figure 4.2 (legend on page 88)

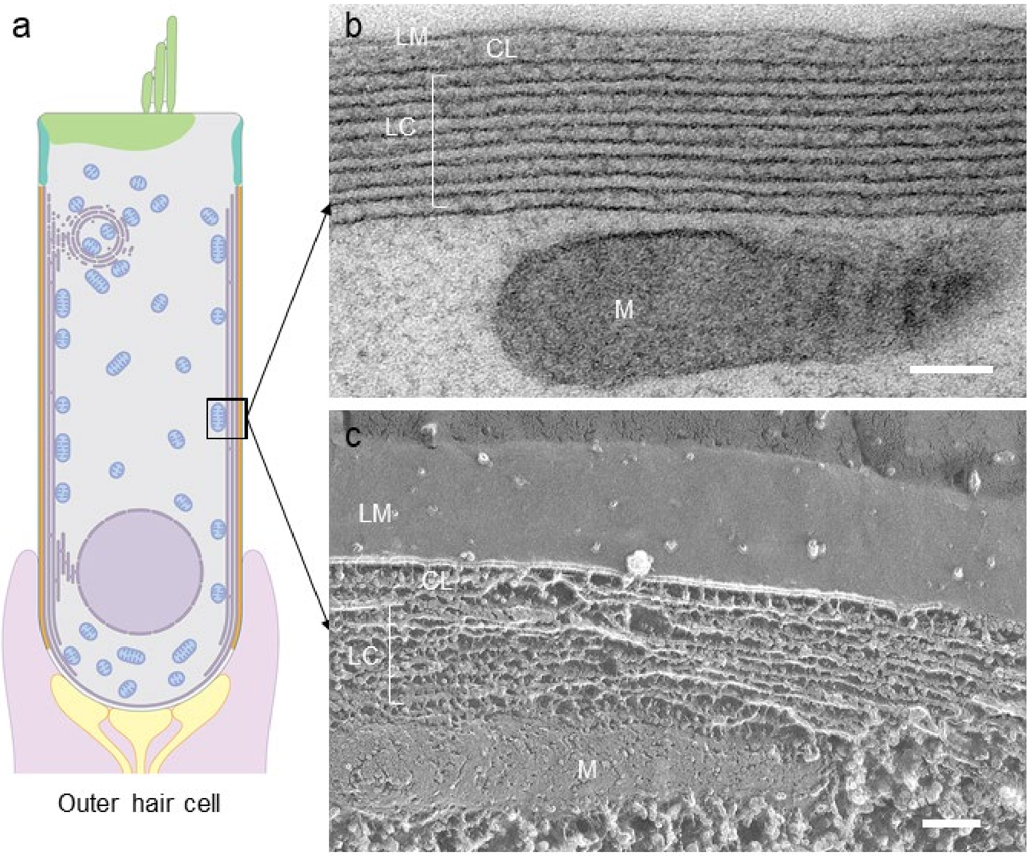

Figure 4.3 Complementary freeze-substitution and freeze-etching views of the outer hair cell lateral wall. (a) A schematic diagram of an outer hair cell. **(b)** Ultrastructural details of the lateral wall complex revealed with slam-frozen, freeze-substituted and low-temperature embedded unfixed sample. **(c)** The same structural organization without dehydration is visualized in a freeze-fracture/freeze-etching replica. The major components of the lateral wall complex include the lateral plasma membrane (LM), the cortical lattice (CL), the lateral cisternae (LC) and the associated mitochondria (M). Scale bars = 100 nm.

4.2 – Results

4.2.1 – Organization of prestin molecules in the lateral plasma membrane

The motor protein prestin is the major constituent of the outer hair cell lateral plasma membrane (He et al., 2010; J. Zheng et al., 2000). However, the precise organization of prestin molecules in the membrane and the relationship between protein organization and electromotility are still not well understood. Stimulation of isolated patches of the guinea pig lateral plasma membrane within a patch electrode demonstrated that the motor activity is distributed throughout the outer hair cell lateral plasma membrane (Kalinec et al., 1992). Consistent with the patch electrode mapping experiment, high-speed visualization of microspheres placed on the surface of the lateral plasma membrane of an isolated guinea pig outer hair cell showed movements throughout the hair cell lateral surface when electrically stimulated (Kitani et al., 2013). In addition, the observed local microsphere movements are not uniform, instead, the orientation of microsphere movements is variable along the lateral plasma membrane during initial electrical stimulation and undergoes rapid reorientation toward the axial axis of the outer hair cell during continuous stimulation (Kitani et al., 2013). Based on the anisotropic motor response and the ability to reorient the local membrane, Kitani and colleagues hypothesized that the motor elements within the lateral plasma membrane were organized in a mosaic of microdomains throughout the lateral plasma membrane. To elucidate the organization of prestin molecules in the lateral plasma membrane and to examine if prestin molecules aggregate into microdomains, we examined the fine surface topography of the lateral plasma membrane in freeze-etching replicas of guinea pig outer hair cells.

Freeze-etching replicas of the guinea pig cochleae provided a detailed visualization of the stratified lateral wall complex (Figure 4.4). The lateral plasma membrane is densely populated with membrane particles and they are distinctly visible in the area where the exoplasmic leaflet of the lipid bilayer has been fractured away (Figure 4.4 white arrow). The majority of these membrane particles are likely to represent prestin molecules (He et al., 2010). However, the splitting of the bilayer during freeze-fracture causes transmembrane proteins to undergo plastic deformation that alters their shape and makes it difficult to assess their structures accurately. The freeze-etching portion of the replica, where the true outer or inner surface of the plasma membrane was exposed, enables direct viewing of the membrane protein organization. Most of the topography of the membrane is made of protein particles presumed to be integral membrane proteins embedded in the lipid bilayer (Figure 4.4 white arrowhead).

Close examination of the surface of the lateral plasma membrane showed that it consists of microdomains with variable orientation (Figure 4.5a). Filtering the image with Gaussian blur (image smoothing and noise reduction) revealed that these microdomains are aggregates of membrane particles that are orthogonally packed (Figure 4.5c, d & e). Image analysis using fast Fourier transform (FFT), which plots in the reciprocal space the intensity of all the sine waves that make up an image, showed that there are distinct sets of orthogonally arranged sine waves in the image that correspond to the orthogonal pattern of the membrane particles (Figure 4.5b, c & d). In addition, by using inverse-FFT to filter noise and feature only these two sets of sine waves in the real space, we visualized just the organization of membrane particle where we measured these particles to have a center-to-center spacing of 13 nm (Figure 4.5b, c & d).

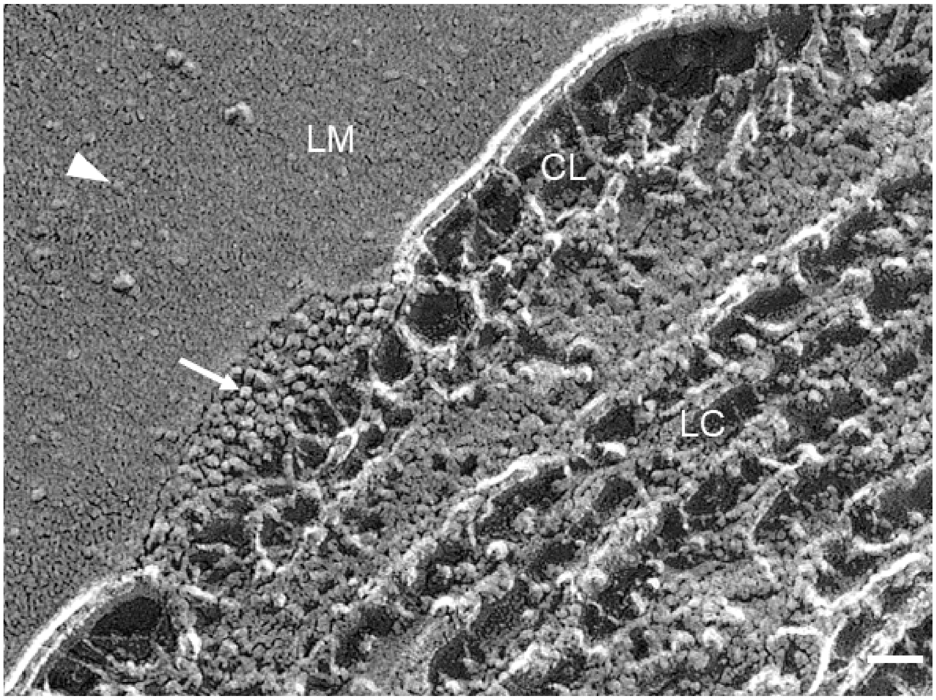

Figure 4.4 Surface topography view of the lateral wall complex. A high magnification micrograph of a freeze-fracture/freeze-etching replica of the guinea pig outer hair cell showing the multilayered lateral wall complex. The complex contains the lateral plasma membrane (LM), the cortical lattice (CL) and the lateral cisternae (LC). The lateral plasma membrane is densely populated with membrane protein complexes that appear as membrane particles (arrow). In the area where the exoplasmic leaflet of the lipid bilayer is fractured off (arrow), membrane particles can be readily observed. In the region where membrane remains intact (experienced only etching), membrane particles have a more subtle appearance due to how the area is shadowed by the platinum atoms (arrowhead). Scale bar = 20 nm.

Figure 4.5 (page 95) Membrane particles are orthogonally packed into microdomains that tile the lateral plasma membrane. (a) A close-up view at the freeze-etching replica of the outer hair cell lateral wall showing the extracellular surface topography of the lateral plasma membrane (LM). Microdomains can be observed to span the LM (dashed line and solid line boxes highlight microdomains). **(b – d)** Regions in **(a)** that underwent different image processing to highlight membrane particle spatial organization in the replica. The first column contains the close-up raw images of select regions in **(a)**. The second column shows the Gaussian blurred raw images. The third column shows the fast Fourier transform (FFT) of the raw images. Arrowheads point to the high-intensity spatial frequencies, highlighting the dominant orthogonal organization within the raw images. Fourier spot mask was applied to the third column to pass the four high-intensity spatial frequencies. Inverse-FFT was applied to the mask power spectrum to visualize the Fourier filtered real space images (fourth column). Scale bars: **(a)** = 100 nm; **(b)** = 20 nm, **(b – d)** share the same scale.

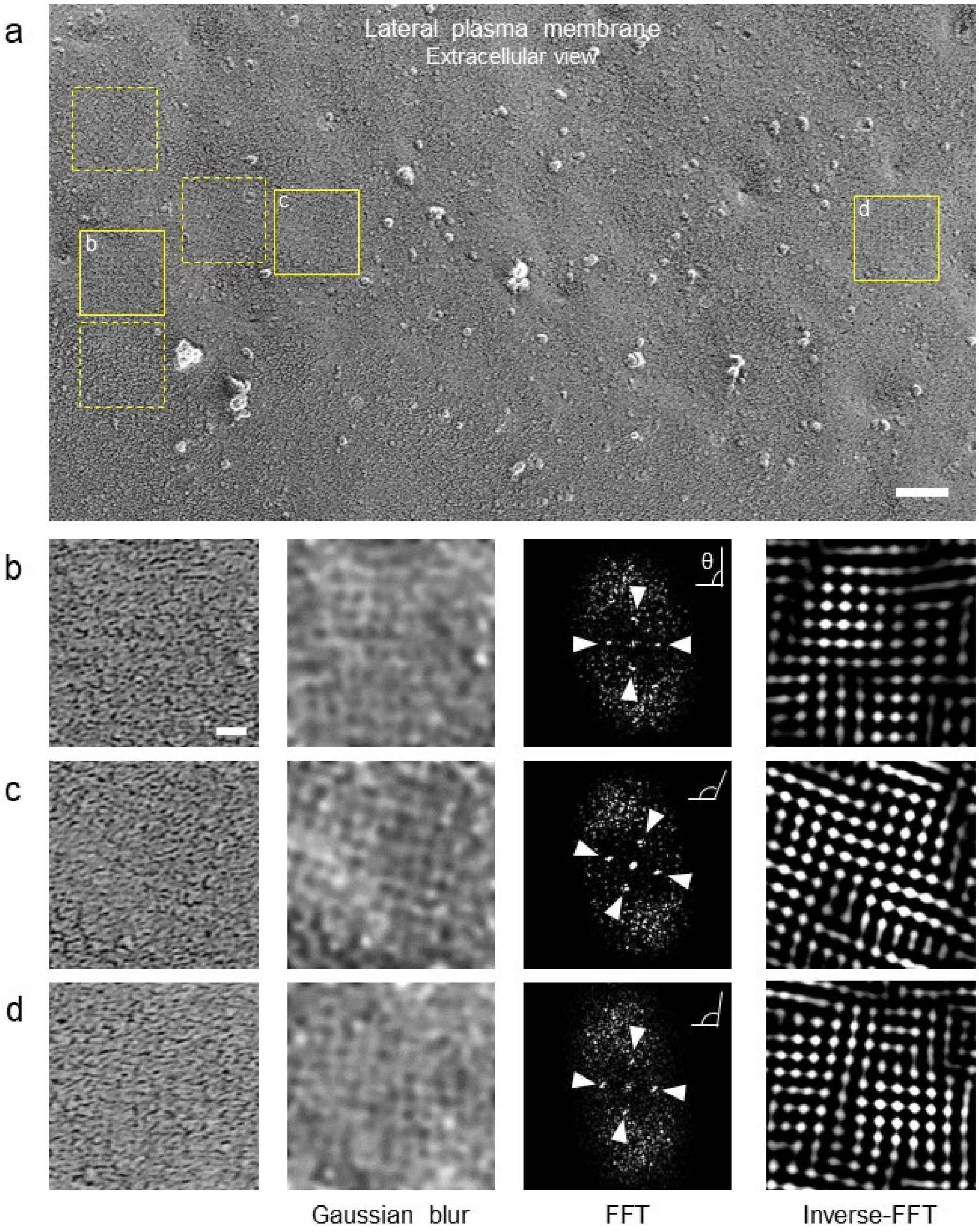

Figure 4.5 (legend on page 94)

4.2.2 – Membrane particle organization associated with the cortical lattice

In addition to the prestin-based microdomains of orthogonally arranged membrane particles, another distinct set of membrane particles forming linear arrays was observed in the lateral plasma membrane (Figure 4.6a, green-colored particles). The identity of this set of membrane particles and their role in the lateral wall structural complex is unclear. Cross-sectional and cytoplasmic views of the outer hair cell lateral wall complex show that these membrane particles appeared to be putatively associated with the pillar-shaped proteins of the cortical lattice (Figure 4.6b & c). Also, the linear arrangement of these particles is likely due to pillar-shaped proteins' distribution along the actin filaments that make up the cortical lattice (Figure 4.6c). The apparent interaction between this set of membrane particles and the pillar-shaped proteins suggests that they may either represent the membrane portion of these pillars or be a closely interacting protein.

Figure 4.6 (page 98) Linear membrane particle arrays are closely associated with pillar-shaped proteins. (a) Different shadowing of the freeze-etched outer hair cell lateral plasma membrane (LM) surface revealed arrays of linearly arranged membrane particles (highlighted in green). **(b)** Cross-sectional and **(c)** cytoplasmic view of the lateral wall complex showing the LM and the cortical lattice (CL). The pillar-shaped proteins (yellow arrowheads in **b** and **c**) are distributed along actin filaments (white arrow) within the CL and connect the CL to the LM via physical insertion (white arrowheads in **c**). The insertion of these pillars into the LM and the linear arrangement indicates that this set of membrane particles is likely the membrane portion of the pillar-shape proteins. Scale bars = 100 nm.

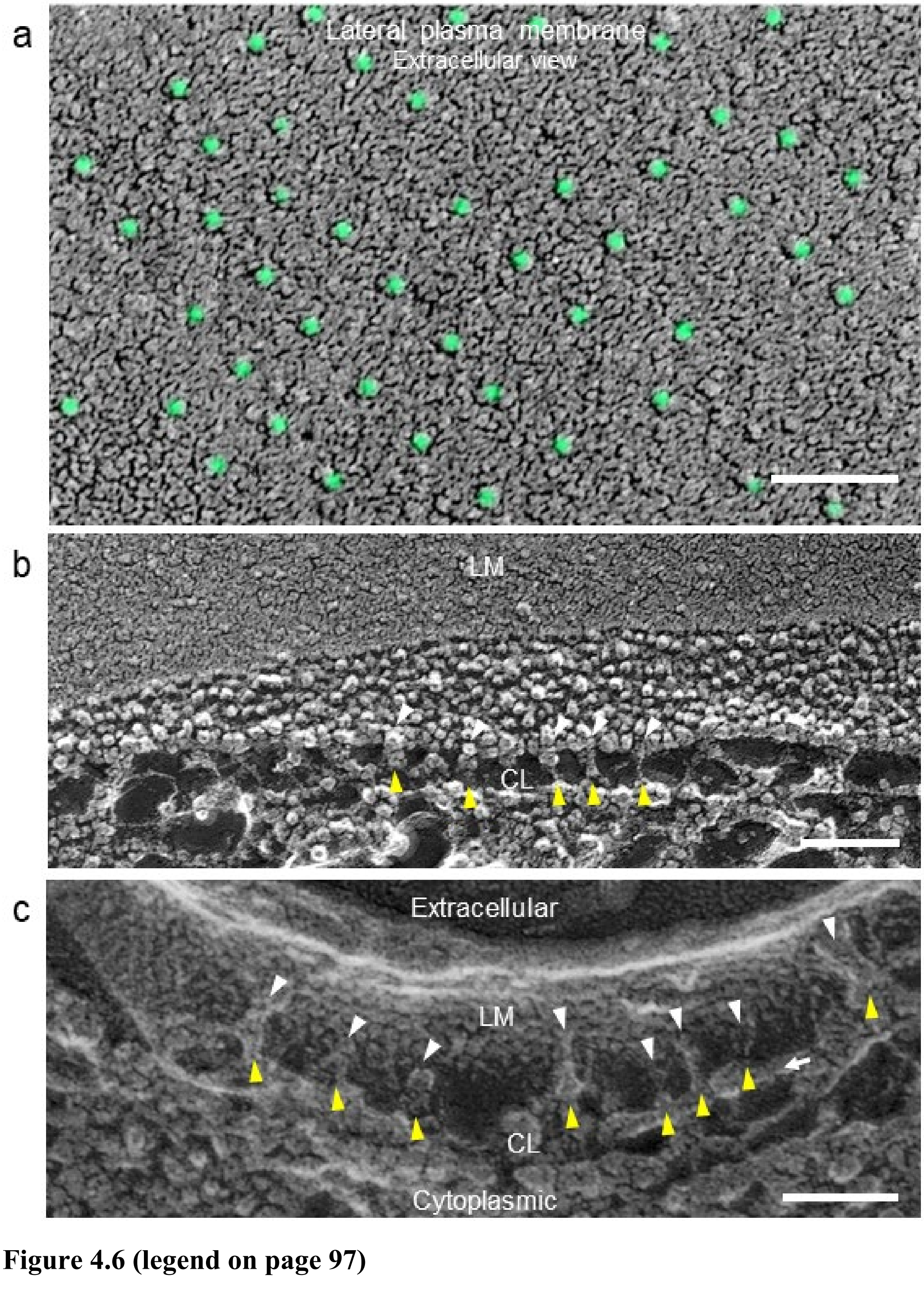

Figure 4.6 (legend on page 97)

4.2.3 – The cortical lattice is physically connected to both the lateral plasma membrane and the lateral cisternae

The interaction between the pillar-shaped proteins of the cortical lattice and the lateral plasma membrane revealed by our replica-based data indicates that different layers of the lateral wall complex are physically connected. To resolve whether the lateral wall complex is an integrated structural organization, electron tomography was performed and tomographic volumes were segmented to visualize the 3D ultrastructure of the lateral wall complex. The layout of the lateral wall complex shows an organization with regular spacing between different layers (Figure 4.7). The cortical lattice resides in between the lateral plasma membrane and the lateral cisternae in a well-defined space that is 38.4 ± 4.0 nm ($n = 59$) wide. Based on previous data, the pillar structures were estimated to be ~25 nm in length (M. C. Holley et al., 1992), indicating that the cortical lattice is situated closer to the lateral cisternae. From the reconstructed tomograms, we identified the electron densities that represent the cortical lattice and measured its position relative to the plasma membrane and the lateral cisternae (Figure 4.7a). The distance from the lateral plasma membrane to the cortical lattice is 22.2 ± 2.1 nm ($n = 72$), matching the estimated ~25 nm pillar length from replicas (M. C. Holley et al., 1992). The cortical lattice is positioned closer to the lateral cisternae with a spacing of 17.2 ± 2.5 nm ($n = 64$). The tomograms also revealed that there are electron densities in between the cortical lattice and the lateral cisternae (Figure 4.7a), similar to the data from a recent tomographic study on the outer hair cell lateral wall [96]. These electron densities suggest that the cortical lattice and the lateral cisternae are physically connected (Figure 4.7a & c). While the ER network that makes up the lateral cisternae is extensive, fenestrations of the ER sheet can break the network's continuity (Figure 4.7a, red box). However, the morphology of the cortical lattice and the lateral plasma membrane remains consistent in regions with no cortical lattice-lateral cisternae interaction (Figure 4.7b). This observation suggests that the cortical lattice is providing substantial, if not the majority, of the structural support for the plasma membrane. Segmentations of the cortical lattice show that there is no obvious register between the lattice's connection to the lateral plasma membrane and the lateral cisternae (Figure 4.7b & c). This observation indicates that the cortical lattice-lateral cisternae interconnection and the cortical lattice-plasma membrane integration involve two independent molecular components and mechanisms.

Figure 4.7 (page 102) The cortical lattice is physically connected to both the lateral plasma membrane and the lateral cisternae. (a) A 6-nm tomographic slice of unfix and directly frozen guinea pig organ of Corti showing the multilayered lateral wall complex and an associated mitochondrion (M). White arrowheads point to locations of electron-dense filaments projecting from the cortical lattice (CL) to the lateral plasma membrane (LM) or the lateral cisternae (LC). **(b – c)** Segmentation of the tomographic volume in select regions (yellow line box and red line box in **a**, respectively). **(b)** Segmentation showing the LM in cyan and the membrane of LC in magenta. The cortical lattice (CL) was segmented in yellow. Two parallel actin filaments (black dashed lines) within the CL were found in this region of interest. White arrowheads point to electron densities connecting the CL to the LM and the LC, indicating physical interactions. **(c)** Segmentation showing two parallel actin filaments (left panel, black dashed lines) of the CL with one interacting with the LC while the other has no underlying LC and only interacts with the LM (right panel, rotated view, black arrowhead). The LM remains consistent when the CL is not interacting with the LC. White arrowheads point to LM-CL and CL-LC linkers. Scale bar = 100 nm.

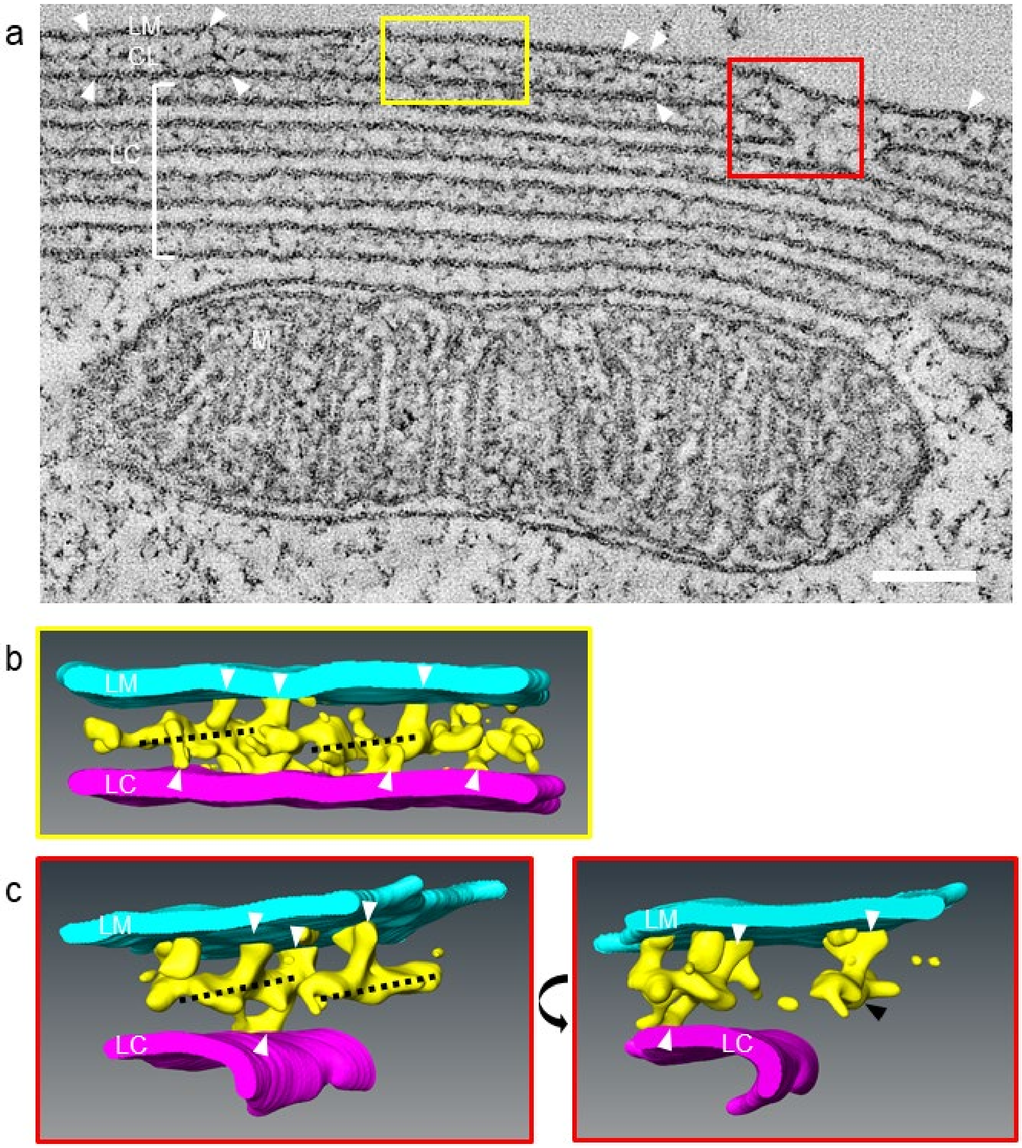

Figure 4.7 (legend on page 101)

4.2.4 – Structural organization of the lateral cisternae

The lateral cisternae is an elaborate system of smooth ER that is physically connected to the cortical lattice (Figure 4.7 & 4.8). It has been suggested to be part of the peripheral ER (Andrew Forge, Zajic, Li, Nevill, & Schacht, 1993), an extensive cytosolic network of membrane comprised of interconnected cisternae and tubules that share a continuous lumen (English & Voeltz, 2013). The organization of the outer hair cell lateral cisternae has also been shown to vary from species to species. Amongst mammals, the lateral cisternae in human, rat and mouse outer hair cells contains a single layer of ER (Arnold & Anniko, 1989; Iurato, 1961; Yamashita et al., 2015). On the other hand, the lateral cisternae in guinea pig outer hair cells are multilayered (Figure 4.8) (Saito, 1983). How the lateral cisternae maintain the ER membrane arrangement within the lateral wall complex is unclear. We examined the lateral cisternae in guinea pig outer hair cells using electron tomography to better understand what structural elements help define the regular spatial organization of the lateral cisternae. In guinea pig outer hair cells, the lateral cisternae are organized into a stack of extended sheets with regular structural arrangements (Figure 4.3, 4.7 & 4.8). The luminal width and the distance between individual ER sheets were measured to be 22.7 ± 3.2 nm (n = 114) and 18.8 ± 3.3 nm (n = 111), respectively. Electron tomography data revealed that the lumen of the lateral cisternae contains repeating electron densities and there are electron-dense links in between each ER sheet (Figure 4.8). The presence of these periodic electron densities suggests that they may be structural elements contributing to the regular organization of the lateral cisternae.

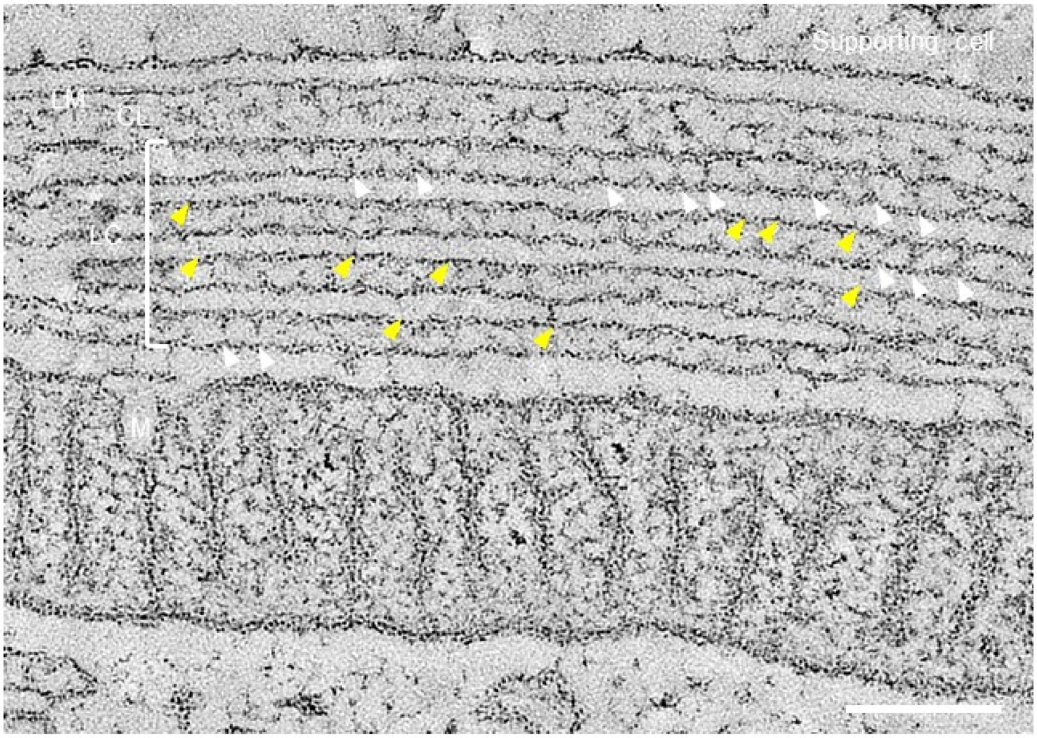

Figure 4.8 The lateral cisternae is an organized ER network with regular inter- and intra-cisternal electron-dense links. A 3-nm tomographic slice of unfix and directly frozen guinea pig organ of Corti showing that the lateral cisternae is composed of a stack of extended ER sheets with consistent and regular spacings. Repeating electron-dense links are found within the lumen of these ER sheets (white arrows). Individual ER sheets appear to be connected via electron-dense filaments. Scale bar = 100 nm.

To better understand the role of these repeating elements in the lateral cisternae ER membrane organization, freeze-etching replicas of the lateral wall complex were generated. Replicas showing the lumen of the lateral cisternae, a challenging view to obtain, revealed that large regular protein particles or complexes populate both membranes of the ER sheet (Figure 4.9a). These membrane particles often appear as

11 to 13 periodic subunits arranged into a ring pattern (Figure 4.9b). However, we could not determine if the variation in the number of subunits within these protein complexes is an inherent property or an artifact caused by the intrinsic granularity of the platinum replica (Krystofiak et al., 2019). The height of these large protein particles or complexes protruding into the ER lumen suggests that they might correspond to the repeating electron densities that were observed in our tomograms of thin sections (Figure 4.8). Preliminary analysis of these particles using class averaging, a collaboration with Dr. Benes Trus (NIH/CIT), showed that these ring-shaped particles or complexes are ~25 nm in diameter but with no perfect symmetry and could not be further resolved by class averaging methods (Figure 4.9b). Our replicas showed dense particle packing but no two-dimensional packing configuration could be detected by either simple visualization or by FFT analysis. The presence of these integral ER membrane particles on both cisternal membranes suggests that they are likely involved in the form and function of the lateral cisternae.

Figure 4.9 (page 106) Large and regular ring-like protein complexes populate the lumen of the lateral cisternae. (a) A freeze-fracture/freeze-etching replica showing the different layers of the guinea pig outer hair cell lateral wall complex. The exposed lumen of the lateral cisternae reveal a dense population of regular protein complexes in both membranes of the ER sheet. The yellow arrow points to the upper ER membrane and the white arrow points to the lower ER membrane. **(b)** Selected particles (left panel) were processed for class averaging and the averaged particle was plotted to show the 3D contour of the complex (right panel). These complexes appear to contain 11 to 13 subunits (highlighted by the red peaks). Scale bars: **(a)** = 100 nm; **(b)** = 50 nm.

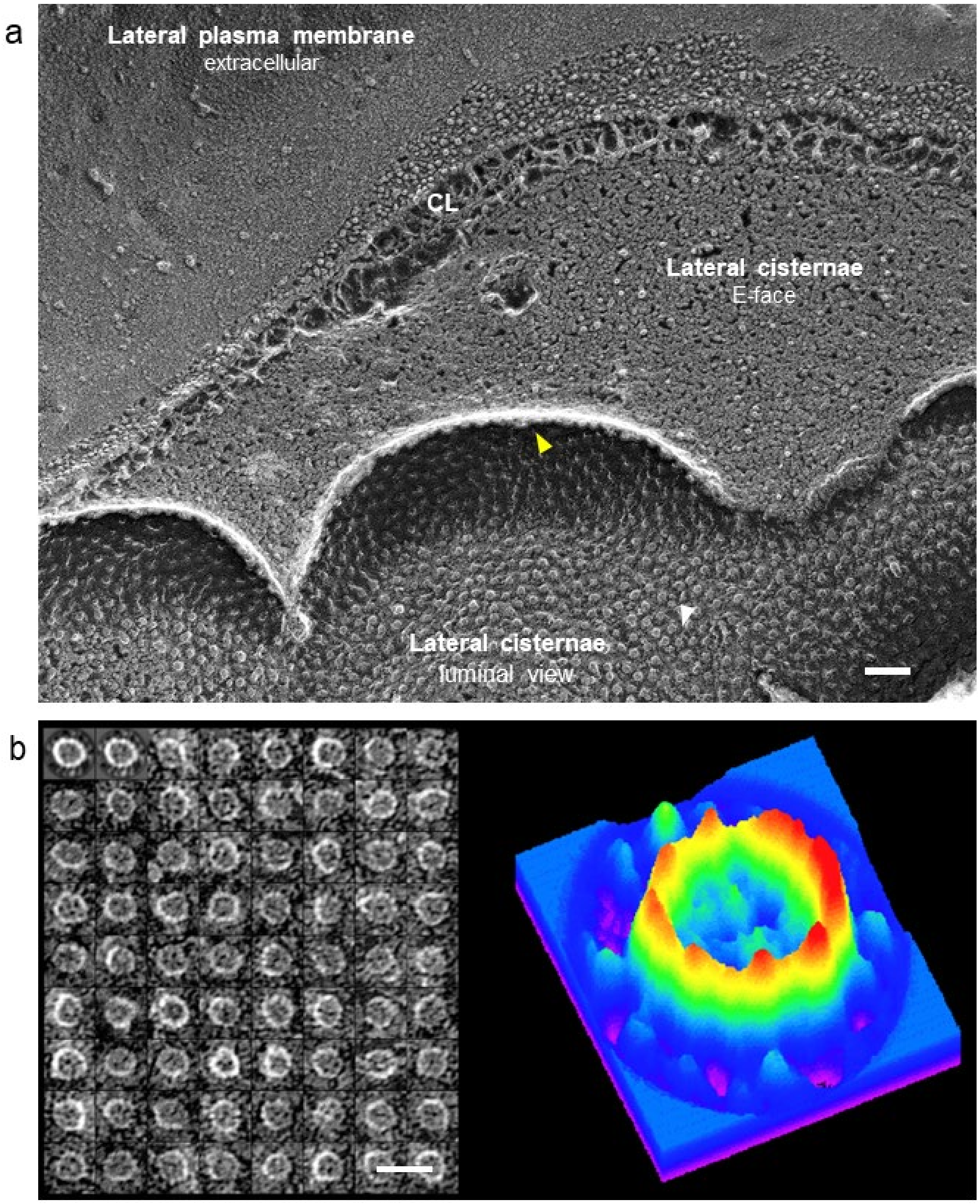

Figure 4.9 (legend on page 105)

While ER sheets predominate the lateral cisternae, ER tubules are also observed within the lateral cisternae (Figure 4.10). And because we used direct freezing, we expect that the different ER membrane organizations that we observe to reflect the natural lateral cisternae configuration at the moment of the rapid freezing and not artifacts induced by slow chemical fixation. The presence of ER tubules within the lateral cisternae suggests that the lateral cisternae structure is dynamic and can shift between sheets and tubules.

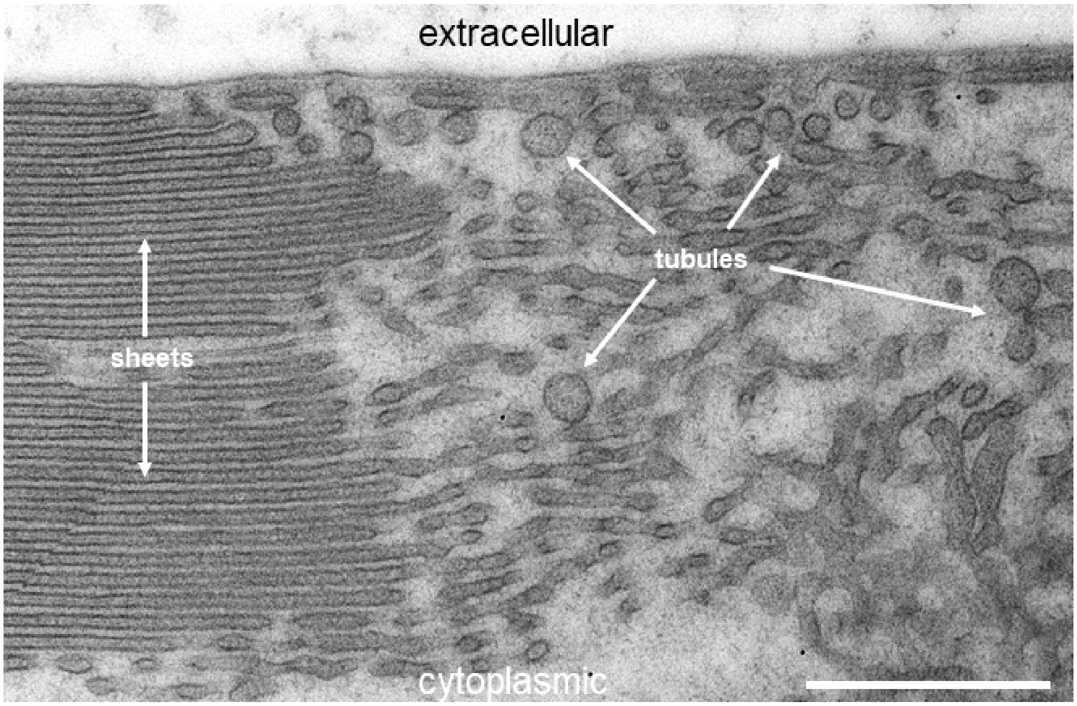

Figure 4.10 The lateral cisternae contains both ER sheets and tubules. A micrograph from unfix and directly frozen guinea pig organ of Corti showing a close-up view of the organization lateral cisternae (LC) in a near-native state. The ER membrane configuration within the LC contains both ER sheets and tubules, indicating that the membrane organization within the LC is dynamic. Scale bar = 500 nm.

4.2.5 – Mitochondrial association to the lateral cisternae

Our data has shown that the lateral wall complex is an integrated structure where the lateral plasma membrane, the cortical lattice and the lateral cisternae are mechanically interconnected (Figure 4.7a, 4.8 & 4.9). In addition to these major structural components, a population of mitochondria has been consistently observed to be in close association with the inner surface of the lateral cisternae (Figure 4.11a). The role of this mitochondrial population in outer hair cell electromotility and whether these mitochondria have a structural relationship with the lateral wall complex is unclear. We used electron tomography to resolve whether these mitochondria have physical interactions with the lateral cisternae. Our tomographic data revealed that the mitochondria positioned close to the lateral cisternae are physically tethered to the ER membrane via electron-dense links (Figure 4.11b). The mitochondria along the lateral wall complex are positioned ~30 or less nm away from the lateral cisternae and we measured the length of ER-mitochondria electron-dense links at 23.0 ± 4.1 nm ($n = 13$). The mitochondrial population's physical connection to the lateral cisternae suggests the mitochondria are an integral part of the lateral wall complex and contribute to electromotility.

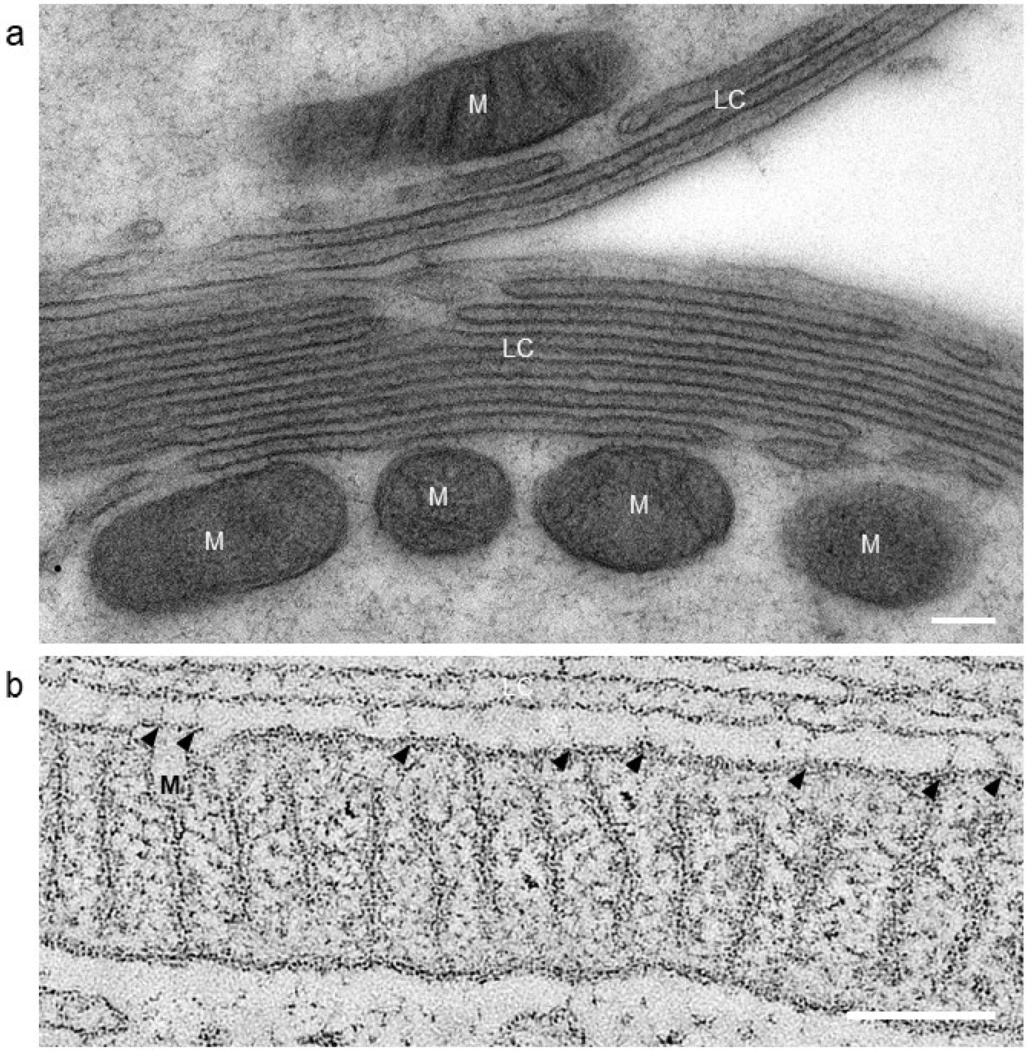

Figure 4.11 Mitochondria are closely associated with the lateral cisternae. (a) A micrograph showing the lateral wall complexes in two adjacent outer hair cells from unfix and directly frozen guinea pig cochlear tissue. A population of mitochondria (M) is observed to be closely associated with the cytoplasm-facing portion of the lateral cisternae (LC). **(b)** A focused view of the LC-M interface from the tomogram projection image of **Figure 4.8**. Electron-dense filaments (black arrowheads) connect the M and the LC. Scale bars = 100 nm.

4.2.6 – Hensen’s body complex

The physical tethering of mitochondria to the lateral cisternae indicates that ER-mitochondria interactions have a role in the structure and function of the lateral wall complex (Figure 4.11). Hensen’s body, a concentrically arranged lamellar and tubular ER flanked by mitochondria, is commonly observed in the outer hair cell apical cytoplasm (Figure 4.12a). In addition, Hensen’s body can be seen to form a continuous ER network with the lateral cisternae (Figure 4.12b). The structural organization of ER membranes and the associated mitochondrial population within the Hensen’s body is similar to the organization of the lateral cisternae and the connected mitochondria. While Hensen’s body complex is structurally similar to the lateral cisternae, its role in the outer hair cell is not well defined. We employed electron tomography to get a better understanding of the spatial arrangement of the ER network and the associated mitochondria within these Hensen’s bodies. Our quantifications suggest that the spatial arrangements within Hensen’s bodies are comparable to that of the lateral cisternae. The luminal width of the ER sheets is 21.2 ± 1.9 nm ($n = 30$) and the spacing between sheets is 16.2 ± 2.0 nm ($n = 25$), in the lateral cisternae, the measurements were ~23 nm and ~19 nm, respectively. The mitochondria associated with the Hensen’s bodies are also positioned less than 30 nm (24.2 ± 5.9 nm, $n = 21$) to the ER membranes. Tomographic data of Hensen’s body reveals that there are repeating electron densities within the lumen of the ER sheets, electron-dense links are found to interconnect the sheets and mitochondria are tethered to the ER membrane via electron-dense connectors (Figure 4.13b). These features match the observations from tomograms of the lateral cisternae (Figure 4.8). These lines of evidence suggest that Hensen's body complex likely has a close structural relationship with the later wall complex and may play a role in outer hair cell electromotility.

Figure 4.12 (page 111) Hensen's bodies are found in the outer hair cell apical cytoplasm and form a continuous ER network with the lateral cisternae. (a) A micrograph from a fixed guinea pig organ of Corti showing the apical region of outer hair cells where Hensen's bodies (HB) are found (dashed line circles). The white dashed line circle region shows ER membranes of HB forming a continuous network with the lateral cisternae (LC). **(b)** A lower-mag view of the same region in **Figure 4.10** showing that the ER network is continuous between the LC and the HB in the native environment (sample is unfixed and directly frozen). SC: stereocilia; CP: cuticular plate; M: mitochondria. Scale bars = 500 nm.

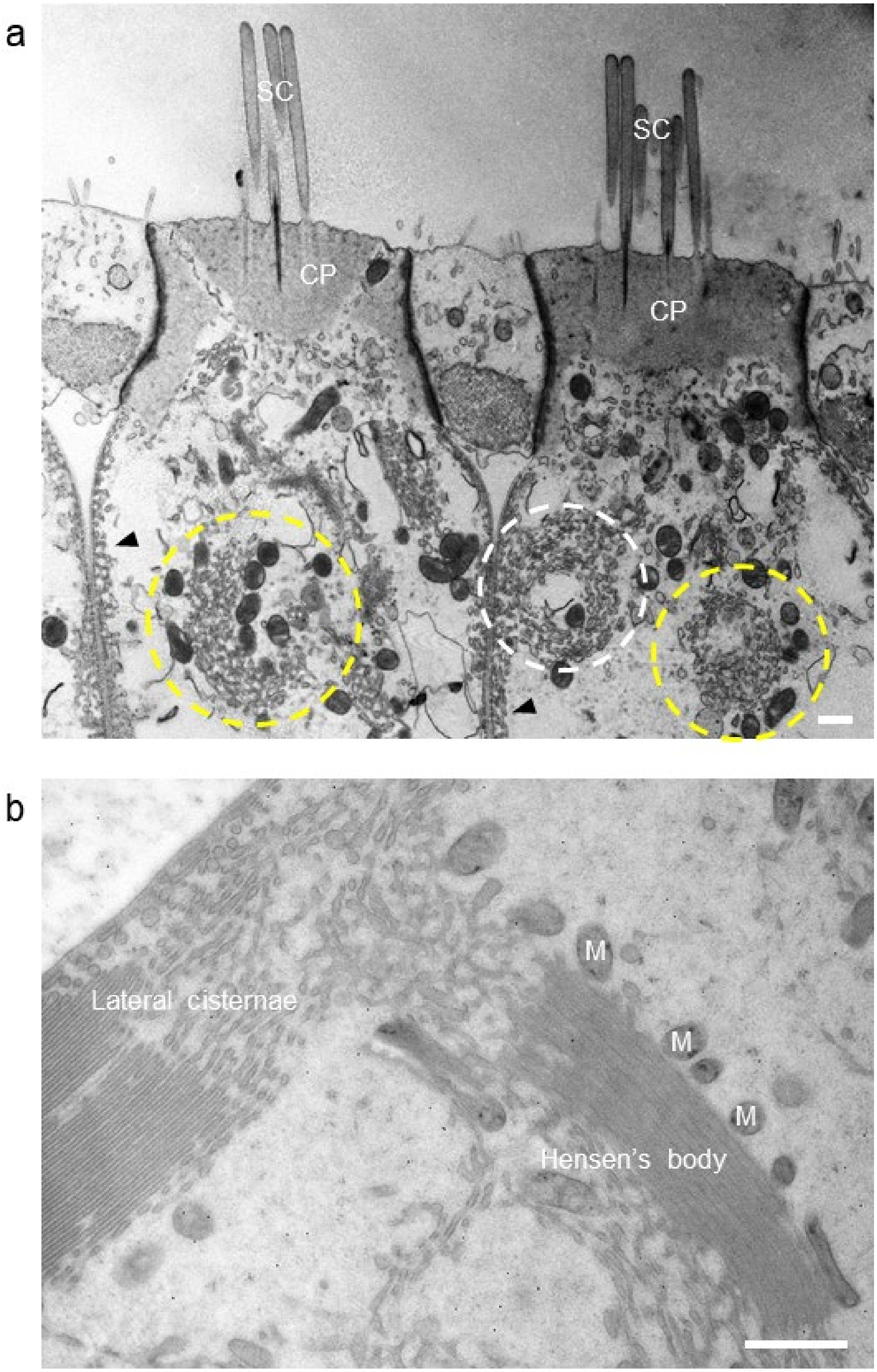

Figure 4.12 (legend on page 112)

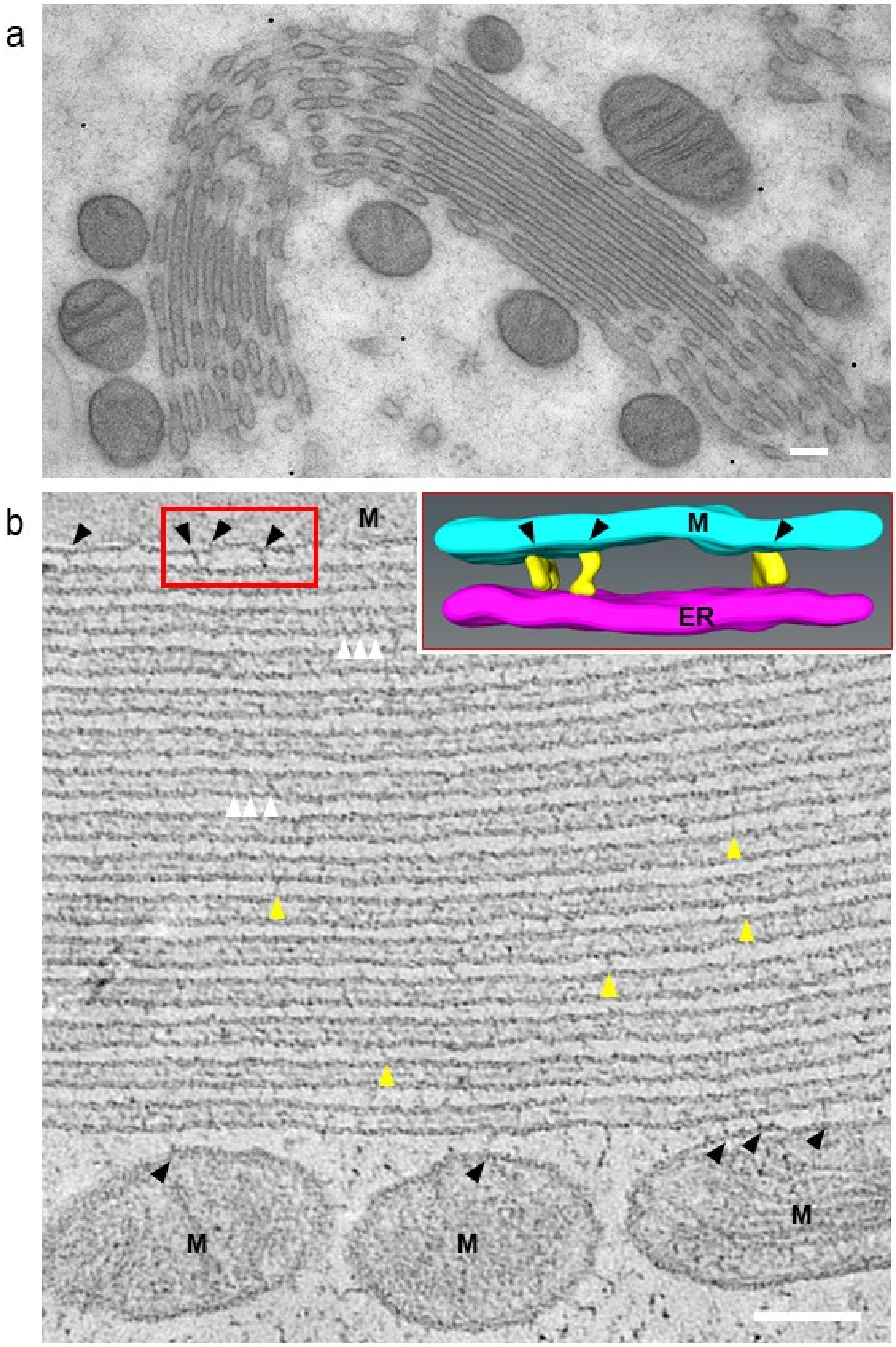

Figure 4.13 (legend on page 114)

Figure 4.13 (page 113) Hensen's body is structurally similar to the lateral cisternae. (a) A high-mag view of a Hensen's body (HB) from an unfix and directly frozen sample showing concentrically arranged ER membrane in sheets and tubules that is flanked by mitochondria. **(b)** A 7-nm tomographic slice from an unfixed sample showing that the lumen of the ER sheets within HB contain repeating electron-dense links (white arrowheads) and the sheets are connected by electron-dense filaments (yellow arrowheads). Electron-dense filaments (black arrowheads) are also observed between the mitochondria (M) and the ER membrane. Segmentation of the red box region is shown in the inset. Mitochondrial membrane is in cyan, ER membrane is in magenta and linkers are in yellow. These structural features within HB are comparable to the features observed within the lateral cisternae (**Figure 4.8** and **4.11b**). Scale bars = 100 nm.

4.3 – Discussion

4.3.1 – Tetrameric prestin at the lateral plasma membrane

The spacing of particles in the orthogonal arrangement (Figure 4.5), the 11 ~ 15 nm particle diameter measured from platinum replicas (Kalinec et al., 1992) and the estimated dimensions of monomeric prestin (Figure 4.14a & b) in the membrane being 4.5 x 6 nm (Geertsma et al., 2015; Gorbunov et al., 2014) suggest that a single particle within the microdomain contains multiple prestin molecules. Evidence from western blots and light microscopy experiments suggests that prestin oligomerizes and a tetramer is likely a common form(Hallworth & Nichols, 2012; J. Zheng et al., 2006). Furthermore, single-particle analysis of negative-stained purified prestin protein complex showed that prestin molecules form a particle that is ~8 nm in diameter with a four-fold symmetry that is consistent with tetrameric stoichiometry (Mio et al., 2008). The thickness of the platinum replica contributed to the difference in the measured particle diameter between the negative-stained samples and the replicas (see chapter 3.2.3 for additional details). While the dimensions of the membrane particles and their orthogonal arrangement agree with a tetrameric prestin configuration, the precise oligomeric state and the relevance of multimer assembly to prestin motor function remain unresolved as the atomic structure of prestin has yet to be directly determined.

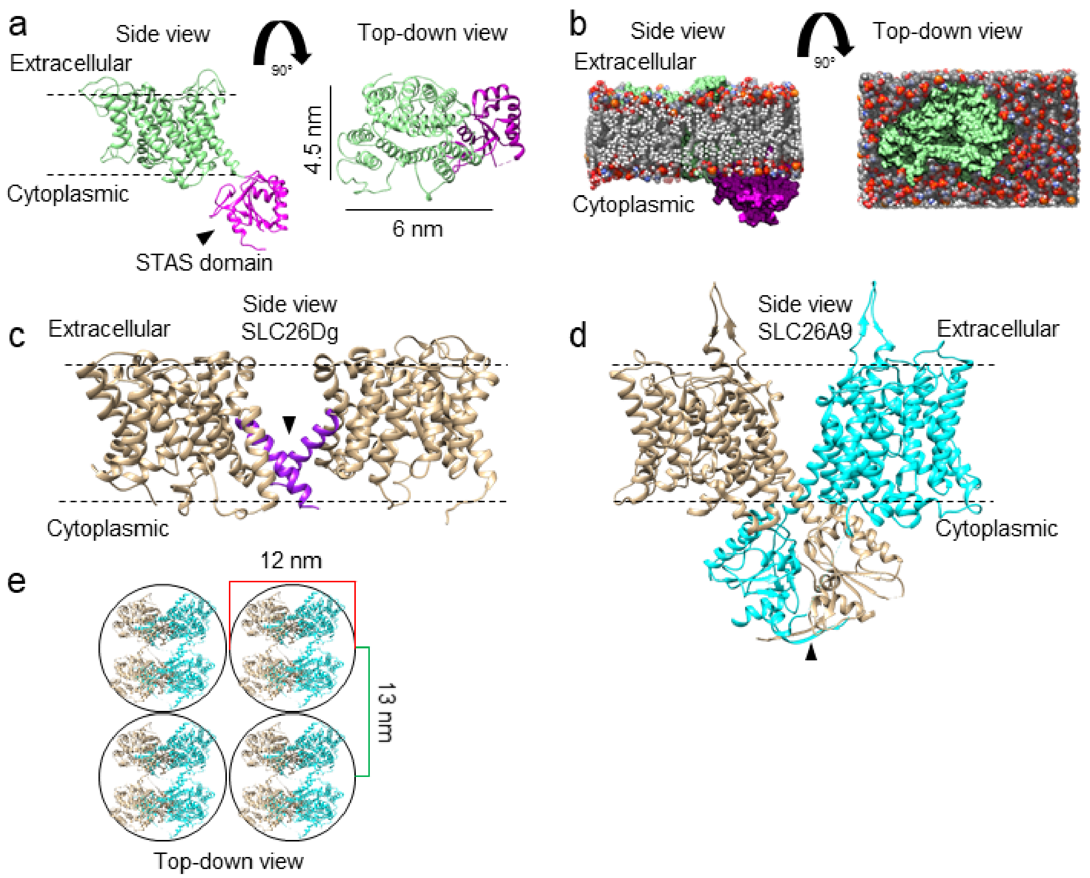

Figure 4.14 Protein models of prestin suggest a dimeric configuration. (a) A protein model of monomeric prestin. The transmembrane portion (in tan) is based on the crystal structure of a prokaryotic homolog SLC26Dg. The cytosolic STAS domain (in magenta) is from the crystal structure of rat SLC26A5's cytosolic domain. **(b)** Surface rendering of the monomeric prestin protein model in the lipid bilayer. **(c)** A possible dimeric configuration of prestin showing the oligomeric interface is between the transmembrane α-helix 14 (black arrowhead, α-helices in blue). **(d)** Another possible dimeric configuration of prestin based on cryo-electron microscopy data of prestin's relative SLC26A9. The dimeric interface is located in the cytosolic domain (black arrowhead). **(e)** A dimer of dimer configuration of prestin can be fitted into the membrane particles observed in freeze-etching replicas. All items are to scale.

The current structural understanding of the mammalian SLC26 family of membrane proteins, where prestin is member A5, is derived from the X-ray crystal structure of the bacterial homolog SLC26Dg and Cryo-EM structure of murine SLC26A9 (Geertsma et al., 2015; Walter et al., 2019). The crystal structure of SLC26Dg helped reveal the general architecture of the transport domain of SLC26, which consists of 14 membrane-inserted α-helices in a 7 + 7 inverted repeat configuration (Geertsma et al., 2015). In addition, SLC26 shares a C-terminal cytosolic STAS (sulfate transporter and anti-sigma factor antagonist) domain (Pasqualetto et al., 2010). Previous studies have described dimeric states for both pro- and eukaryotic members within the SLC26 family suggesting that the conserved oligomeric state for the SLC26 family is dimeric (Compton, Karinou, Naismith, Gabel, & Javelle, 2011; Compton et al., 2014; Detro-Dassen et al., 2008). Most recent studies using a combination of biochemistry, computational simulation and Cryo-EM showed two types of SLC26 dimerization (Chang et al., 2019; Walter et al., 2019). The first type of dimerization is from cross-linking of cysteine residues along the transmembrane domain 14 α-helix between SLC26Dg protomers and is sufficient for SLC26Dg to form a dimer without involving the cytosolic STAS domain (Chang et al., 2019) (Figure 4.14c). On the other hand, the Cryo-EM structure of murine SLC26A9 suggests that the cytosolic STAS domain acts as the primary interface for oligomerization and protomer-protomer transmembrane domain interaction is minimal (Walter et al., 2019) (Figure 4.14d). It is important to note that the intracellular C-terminal region of prestin, including the STAS domain, only shares ~30% homology with other members of the SLC26 family of proteins and it is involved in prestin specific functions such as influencing the characteristic nonlinear capacitance (Bai, Navaratnam, Samaranayake, & Santos-Sacchi, 2006; Keller et al., 2014; Lolli, Pasqualetto, Costanzi, Bonetto, & Battistutta, 2016; J. Zheng et al., 2005). It may be possible that prestin being the unconventional member of the SLC26 with unique motor function does not conform to the general SLC26 protein structure and cytosolic interaction derived from its pro- and eukaryotic homologs. While the dimensions of the membrane particles and their spatial arrangement (Figure 4.5) support prestin tetramerization, dimerization data of SLC26Dg and SLC26A9 indicates the potential of higher order oligomers such as dimers of dimers (Figure 4.14e). The oligomerization of SLC26 may be foundational to the transport function, and in the case of prestin, the motor function. Moreover, subunit cooperativity likely plays a role in the mechanism underlying rapid protein conformational changes. The SLC26Dg crystal structure showed that the complete anion binding site and translocation pathway are both contained within the monomer, suggesting that individual subunit can carry out the canonical transport function without cooperating with other subunits (Geertsma et al., 2015; Homma et al., 2013; Wang, Yang, Jia, & He, 2010). However, examinations of SLC26 dimers showed that one subunit could affect the activity of the other subunit, indicating that dimerization may ultimately be functionally relevant (Detro-Dassen et al., 2008; Gorbunov et al., 2014).

The measured dimensions of the outer hair cell lateral wall membrane particles and their arrangement suggest that prestin is expressed in the membrane as a 4-unit complex, in a tetrameric or dimer of dimer configuration, that is orthogonally packed into microdomains tiling the lateral plasma membrane (Figure 4.14e). Interestingly, the tetrameric oligomerization and the orthogonal packing of prestin resemble the organization of Aquaporin 4 (AQP4). AQP4 is an integral membrane protein channel that mediates cellular water flow and it is highly expressed in the membrane of astrocytes. AQP4 molecules populate the membrane as orthogonal arrays of particles with individual protein particles formed by a tetramer of AQP4 (Nagelhus & Ottersen, 2013). The water permeability of individual AQP4 subunit has also been shown to be independent of tetramerization (Kitchen, Conner, Bill, & Conner, 2016), similar to the self-contained SLC26 monomer (Geertsma et al., 2015). While AQP4 and prestin are structurally and functionally distinct, data on AQP4 oligomerization, subunit behaviour and square array arrangement support the idea that prestin molecules in the outer hair cell lateral plasma membrane are 4-unit complexes with orthogonal microdomain supramolecular structure. To fully resolve the oligomeric state of prestin and to understand how prestin operates to produce outer hair cell electromotility will require the atomic structure of prestin either through Cryo-EM or X-ray crystallography and its direct observation in the lateral plasma membrane by Cryo-EM. Our replica-based data provides a preliminary insight into the structural basis of how prestin molecules are organized in the lateral plasma membrane.

4.3.2 – Structural relationship between the cortical lattice and the lateral plasma membrane

The arrangement of the linear membrane particle arrays closely resembles the pattern of the periodically spaced pillar-shaped proteins that are perpendicularly connected to the actin filaments of the cortical lattice (Figure 4.6) (M. C. Holley et al., 1992). The estimated spacing of these membrane particles is ~50 nm, matching the spacing of the actin filaments (M. C. Holley et al., 1992). These pillar-shaped structures are ~25 nm long and link the outer hair cell cortical lattice, primarily composed of actin filaments cross-linked by αII-βV spectrins, to the lateral plasma membrane (M. C. Holley et al., 1992; Legendre et al., 2008).

The long-range interactions between the cortical lattice and the lateral plasma membrane is distinct from other membrane-associated actin-spectrin lattices such as the pseudohexagonal lattice (short actin filaments cross-linked by αI-βI spectrins) of the erythrocyte and the membrane-associated periodic skeleton (actin filaments in a ring configuration cross-linked primarily by αII-βII spectrins) in neuronal axons (Smith et al., 2018; Unsain, Stefani, & Cáceres, 2018). For both erythrocyte and neuronal axons, the actin-spectrin cytoskeleton is connected to the plasma membrane via ankyrin, an adaptor protein that helps anchor spectrin molecules to the membrane by binding to spectrin repeats 14-15 within β-spectrin through its ZU5 domain (Baines, 2010). However, for outer hair cell cortical lattice, GST-pull down experiments showed that βV spectrin could not bind to the ankyrin ZU5 domain (Cortese et al., 2017). The lack of ankyrin binding sites in βV spectrin and the large distance between the cortical lattice and the lateral plasma membrane suggest that the cortical lattice-lateral plasma membrane association may not involve canonical ankyrin-spectrin interplay. Instead, these pillar structures likely represent a novel form of interaction between the actin-spectrin cytoskeleton and the plasma membrane.

4.3.3 – Differential membrane particle organization results in two interlocking arrays

The close functional relationship between the prestin-populated lateral plasma membrane and the actin-spectrin cortical lattice is supported by several key observations. First, in prestin-KO mice, the cortical lattice is also absent (He et al., 2010). Second, prestin and βV spectrin have matching developmental timeframe (Legendre et al., 2008). Lastly, our replica-based data provided unique views of the lateral wall complex that suggest that the lateral plasma membrane and the cortical lattice are physically connected via the pillar-shaped structures (Figure 4.6).

The expression level, localization and the developmental timeframe of core cortical lattice components such as the βV spectrin coincide with that of prestin (Legendre et al., 2008), suggesting that the membrane-associated pillar structures connecting the cortical lattice to the lateral plasma membrane likely exhibit matching timeline of expression. Moreover, the cortical lattice along with the pillars are absent in prestin-null mice, indicating that the expression and function of prestin and the cortical cytoskeleton are interdependent (He et al., 2010). Prestin moelcules have been shown to be relatively immobile and their organizational stability has been attributed to the underlying structures, especially the cortical lattice (Yamashita et al., 2015). Furthermore, lateral compartmentalization within the outer hair cell plasma membrane likely plays a role in the organization of prestin molecules (Takahashi et al., 2018). In prestin-null mice, efferent terminals have been observed to synapse at locations along the lateral wall region in addition to the typical basal location, an indication that the lack of prestin and the cortical lattice freed up the lateral plasma membrane for other specializations such as forming synapses (Takahashi et al., 2018). These sets of data propose that cooperativity between prestin molecules and the cortical cytoskeleton is critical for specializing the outer hair cell lateral wall for electromotility. Our replica-based observation shows that the array of membrane-associated pillar structures and the array of microdomains of prestin molecules are enmeshed and they are likely to be physically interlocked (Figure 4.15). This mechanical coupling between the lateral plasma membrane and the anisotropic cortical lattice forms the structural basis that underlies the anisotropic elongation and shortening of outer hair cells driven by prestin voltage-dependent conformational changes.

These pieces of evidence indicate that functional-mechanical integration between the lateral plasma membrane and the cortical lattice is an integral part of outer hair cell electromotility. The apparent physical connection between the cortical lattice and the lateral plasma membrane suggests that while individual layers within the lateral wall complex may contain dedicated functions, structural integration of these components gives rise to a cohesive structural unit that underlies electromotility.

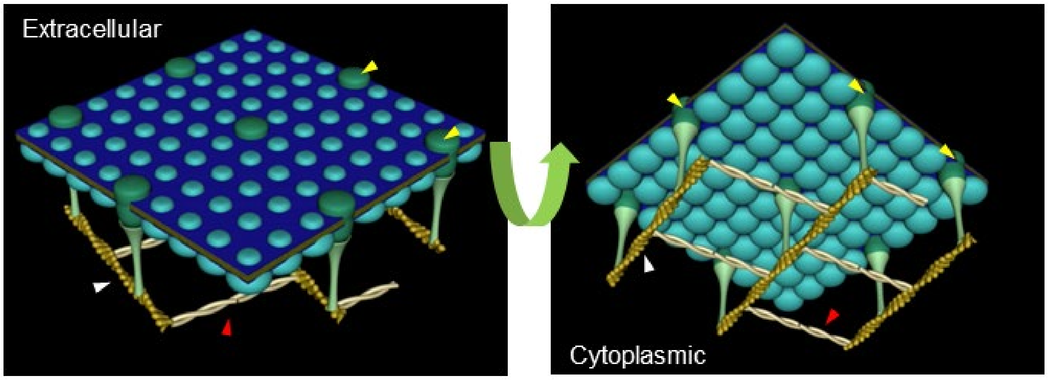

Figure 4.15 Prestin molecules and pillar-shaped proteins intercalate to form two interlocking arrays. Schematic diagrams showing structural integration between the lateral plasma membrane (LM) and the cortical lattice (CL). Membrane particles containing prestin molecules are in teal. Yellow arrowheads point to the membrane portion of the pillar-shaped proteins (in dark green). The cytosolic portion of the pillars is in light green. Red arrowheads point to spectrin molecules that crosslink the parallel actin filaments (white arrowheads). Illustration by Pavel Belyantsev.

4.3.4 – The lateral cisternae: organized ER membranes at the outer hair cell lateral wall

Previous studies on the general ER morphology have shown that abundantly expressed integral ER membrane proteins such as the reticulon proteins and CLIMP-63 (63kD cytoskeleton-linking membrane protein) help regulate the formation and maintenance of different ER membrane organizations (English & Voeltz, 2013). CLIMP-63 is of particular interest as it is an integral membrane protein expressed on both sides of an ER sheet with its coiled-coil domain extending into the lumen (Schweizer, Ericsson, Bächi, Griffiths, & Hauri, 1993). The bridging of the two opposing membranes of an ER sheet and the regular ER luminal spacing have been associated with CLIMP-63 forming homo-oligomers via its luminal coiled-coil domain (Klopfenstein et al., 2001). Ultrastructural experiments using COS-7 cells showed that cells with wild-type CLIMP-63 expression have ER sheets with a luminal width of ~56 nm and RNAi-depletion of CLIMP-63 reduces the spacing to ~28 nm (Y. Shibata et al., 2010). Moreover, overexpression of CLIMP-63 promotes ER sheet formation (Y. Shibata et al., 2010). While CLIMP-63 functions as an ER luminal spacer and acts as a sheet-promoting protein, the dimensions associated with CLIMP-63 do not match the luminal width found in the lateral cisternae. This difference in ER luminal width between CLIMP-63 based ER sheet organization and the lateral cisternae suggests that ER sheet formation and luminal spacing in the lateral cisternae involves other types of molecular components. While it remains unclear what structural elements participate in the organization of the lateral cisternae, our observations with freeze-etching replicas coincided with the tomographic data from Triffo and colleagues where they showed the lateral cisternae membrane contains arrays of electron-dense particles ~19 nm in diameter (Triffo et al., 2019). These sets of data and previous examinations on the general ER morphology lead us to hypothesize that luminal spacing of the lateral cisternae is the result of particle-particle luminal interactions following a mechanism similar to the CLIMP-63 based ER sheet organization.

Besides the regular luminal width, the ER sheets that make up the guinea pig lateral cisternae are also consistently stacked and spaced (Figure 4.8). While tomographic data revealed that there are electron-dense links in between individual ER sheets, it is unclear whether these links are responsible for defining the intercisternal spacing and whether there are additional components or mechanisms involved. Previous studies on the general ER morphology have described two types of spatial organizations for stacked ER sheets. The first type arises from cytosolic interactions between integral smooth ER membrane proteins of adjacent ER tubules that induce ER membranes into tightly packed sheets of smooth ER, resulting in a type of organized smooth ER (OSER) (Lenormand et al., 2013; Snapp et al., 2003). The second type of spatial organization involves unique plasma membrane motifs that interconnect ER sheets within a stack (Terasaki et al., 2013). It is unclear if the guinea pig outer hair cell lateral cisternae is a derivative of the two modes of ER membrane organization described above. We compared the quantified dimensions of the lateral cisternae to the measured spacings of OSER and membrane-connected ER organization to better understand how the guinea pig outer hair cell lateral cisternae is structured.

OSER involves integral smooth ER membrane proteins that induce smooth ER membranes to organize into a stack of sheets such as cytochrome b(5) and Langerin show intercisternal spacing at ~11 nm and 8-9 nm, respectively (Lenormand et al., 2013; Snapp et al., 2003). The intercisternal spacings in these OSER are narrower than our measured OHC lateral cisternae intercisternal spacing at ~19 nm, suggesting that the cytosolic domains of the integral ER membrane proteins involved are larger than the canonical examples given. It is important to note that integral smooth ER membrane protein induced OSER, such as the cytochrome b(5) induced OSER (Snapp et al., 2003), is dependent on the expression level of the protein where once the protein concentration reaches a threshold, ER membranes readily remodel into an OSER structure. While we regularly observe electron-dense links in between ER sheets within the lateral cisternae, it is unclear whether the expression level of these molecules is sufficient to induce the formation of stacked ER sheets and to maintain the regular intercisternal spacing.

Another mechanism that underlies the stacking of ER sheets was elucidated via 3D electron microscopy where Terasaki and colleagues showed that ER sheets are tightly connected through helicoidal membrane motifs (Terasaki et al., 2013). In this mode of ER sheet stacking, an individual ER sheet is linked to the neighboring sheet via a piece of continuous membrane that is twisted clockwise or counterclockwise where the resulting organization resembles a multi-level parking garage and the connecting membranes correspond to the up-down ramps (Terasaki et al., 2013). Such helicoidal architectural ER sheet organization has not been observed in our dataset. Furthermore, comparing the ~23 nm ER sheet spacing of the lateral cisternae to the ~84 – 270 nm distance observed in the helicoidal membrane motif-based multilayered ER sheet organization, it seems unlikely that the lateral cisternae are structured based on this helicoidal membrane architecture. Given our observation of electron-dense links between ER sheets within the lateral cisternae (Figure 4.10), we hypothesize that the regular intercisternal spacing is based on cytosolic interactions of integral ER membrane proteins.

4.3.5 – The outer hair cell lateral cisternae are dynamic

The precise role of different ER membrane organizations (Figure 4.10) in outer hair cell electromotility is not well understood. In addition, the mechanism that underlies lateral cisternae remodeling is not clear. Existing literature on the general ER morphology suggests that proteins related to ER membrane stabilization, such as the reticulon proteins and CLIMP-63, have a central role in the formation of sheets and tubules (Y. Shibata et al., 2010). Shibata and colleagues reported that overexpression of ER luminal spacer CLIMP-63 in COS7 cells leads to the proliferation of ER sheets. On the other hand, overexpression of Rtn4b, a member of the reticulon proteins that is involved in stabilizing ER membrane curvature, promotes ER tubular organizations while decreasing ER sheets in COS7 cells. Interestingly, in COS7 cells that overexpress both CLIMP-63 and Rtn4b exhibited a peripheral ER organization that resembles that of untransfected cells, indicating that the ratio between the sheet-promoting CLIMP-63 and the curvature-stabilizing Rtn4b is important in determining the amount of these two ER membrane configurations. Based on these understandings of how ER membranes could be shaped, we hypothesize that the repeating integral membrane particles present in both ER sheet membranes of the outer hair cell lateral cisternae observed in our freeze-etching replica (Figure 4.9a) are the sheet-promoting factors within the lateral cisternae. These integral membrane particles likely help promote ER sheet formation with the lateral cisternae by stabilizing the distance between the two membranes of an ER sheet. In addition to having stabilizing components within ER sheets, the highly curved membranes of ER tubules and at the edges of ER sheets in the lateral cisternae likely require membrane curvature stabilizing elements to maintain the high membrane curvature. Reticulon proteins, a family of integral membrane proteins that is highly conserved and abundantly expressed in the peripheral ER, are involved in membrane curvature stabilization (Di Sano, Bernardoni, & Piacentini, 2012; English & Voeltz, 2013). Previous experiments have shown that reticulons are enriched at the edges of ER sheets and in ER tubules (Di Sano et al., 2012; Y. Shibata et al., 2010). Moreover, existing data suggest that reticulons are necessary and sufficient in arranging membranes into tubules (Hu et al., 2008). Whether reticulons are part of the lateral cisternae is unclear. The current understanding of ER membrane dynamics from *in vitro* cell line studies (Zhang & Hu, 2016) indicates that lateral cisternae membrane remodeling likely depends on the expression dynamics of luminal spacers and curvature-stabilizing proteins in a manner similar to the mechanism described by Shibata and colleagues (Y. Shibata et al., 2010).

4.3.6 – ER-mitochondria structural arrangement and interactions plays a role in outer hair cell electromotility

In general, ER-mitochondria interaction has been associated with several important functions including Ca^{2+} signaling & homeostasis, lipid synthesis & exchange and mitochondrial division (Jonathan et al., 2011; Osman, Voelker, & Langer, 2011; Rizzuto et al., 1998; Szabadkai et al., 2006; Vance, 1990). Our observations of direct interfacing of ER and mitochondria (Figure 4.11b) are in agreement with existing data from cell (RBL-2H3) and tissue (rat liver) (György Csordás et al., 2006). Csordás and colleagues showed via conventional and cryo-electron tomography the presence of physical tethers between ER membrane and mitochondria. Their measured length of the electron-dense links between ER membrane and mitochondria ranges from ~10 – 25 nm depending on the type of ER and cell's stress level. The measured length of the ER-mitochondria links at the lateral wall complex is 23.0 ± 4.1 nm ($n = 13$).

In the inner ear, mutations in the mitochondrial genome can lead to deafness (Kokotas, Petersen, & Willems, 2007). Moreover, the robustness of outer hair cell functions is closely associated with mitochondrial health and ER-mitochondria interactions (Lyu et al., 2020; Perkins et al., 2020; Someya et al., 2009). In the case of age-related hearing loss, data suggests that mitochondrial energy output, mitochondrial division/fusion, mitochondrial-associated ER membrane and ER/mitochondria-based intracellular Ca^{2+} regulation all degrade with age and put outer hair cells under stress

(Perkins et al., 2020). Experimental data from yeast and CO7 cells has suggested that ER-mitochondrial contacts and ER tubules are important in facilitating the fission process of mitochondria (Jonathan et al., 2011). We have observed that the membranes within the lateral cisternae are dynamic (Figure 4.10, chapter 4.2.4). ER dynamics within the outer hair cell lateral cisternae could be required for outer hair cell cellular homeostasis (Perkins et al., 2020). The sheets within the lateral cisternae act as a site for ER-organelle interactions, such as forming ER-mitochondria interfaces (Figure 4.11b), which could be involved in regulating Ca^{2+} flux and energy production (György Csordás et al., 2006; G. Csordás et al., 2010). Moreover, the tubular ER membrane arrangement at the lateral wall could be facilitating mitochondrial fission (Jonathan et al., 2011), an essential component of mitochondrial homeostasis and an integral part of cellular homeostasis (Cardenas et al., 2010). The dissociation of mitochondria from the lateral cisternae and a decrease in mitochondrial energy output, both of which affect outer hair cell survivability, are likely key contributors to age-related hearing loss (Perkins et al., 2020). Similarities in structure and spatial arrangements between the lateral cisternae and Hensen's body complex suggest that Hensen's body could also be contributing to these ER-mitochondria associated functions. Previous work from our lab has suggested that the Hensen's body may be involved in Ca^{2+} regulation and signaling (Mammano et al., 1999). The observation that the lateral cisternae and Hensen's body complex forming a continuous ER network (Figure 4.12b) indicates that the Hensen's body likely participates in the regulation of the lateral cisternae through shifting ER-mitochondria organization to and from the lateral wall (Saito, 1983; S. B. Yu & Pekkurnaz, 2018). In mice, changes to the structural organization of Hensen's bodies have been associated with aging (Perkins et al., 2020). It is a possibility that Hensen's body supplements the lateral cisternae in activities related to cellular homeostasis and outer hair cell survival as it is structurally set up for functions including Ca^{2+} regulation, energy production and mitochondrial population management. In summary, ER dynamics and ER-mitochondrial interactions at and near the lateral wall complex are likely directly involved in outer hair cell cellular homeostasis and survival that in effect enable outer hair cell electromotility.

4.4 – Summary

4.4.1 – Outlining a structural blueprint that orchestrates outer hair cell electromotility

The data presented in this chapter provides critical updates to the structural framework that underlies outer hair cell electromotility (Figure 4.16 & Table 4.1). The combination of cryogenic sample preparation, electron tomography and freeze-etching electron microscopy helped visualize the multilayered outer hair cell lateral wall complex in 3D at a near-native state and revealed novel structural details in the lateral plasma membrane and the lateral cisternae membrane. From directly frozen, freeze-substituted, plastic-embedded samples, we observed that the lateral plasma membrane is continuously flat with the lipid bilayer exhibiting minimal changes to its shape across the length of the outer hair cell. Consistent with the data from plastic sections, freeze-etching replicas of the outer hair cell lateral wall showed that the lateral plasma membrane has a smooth contour.

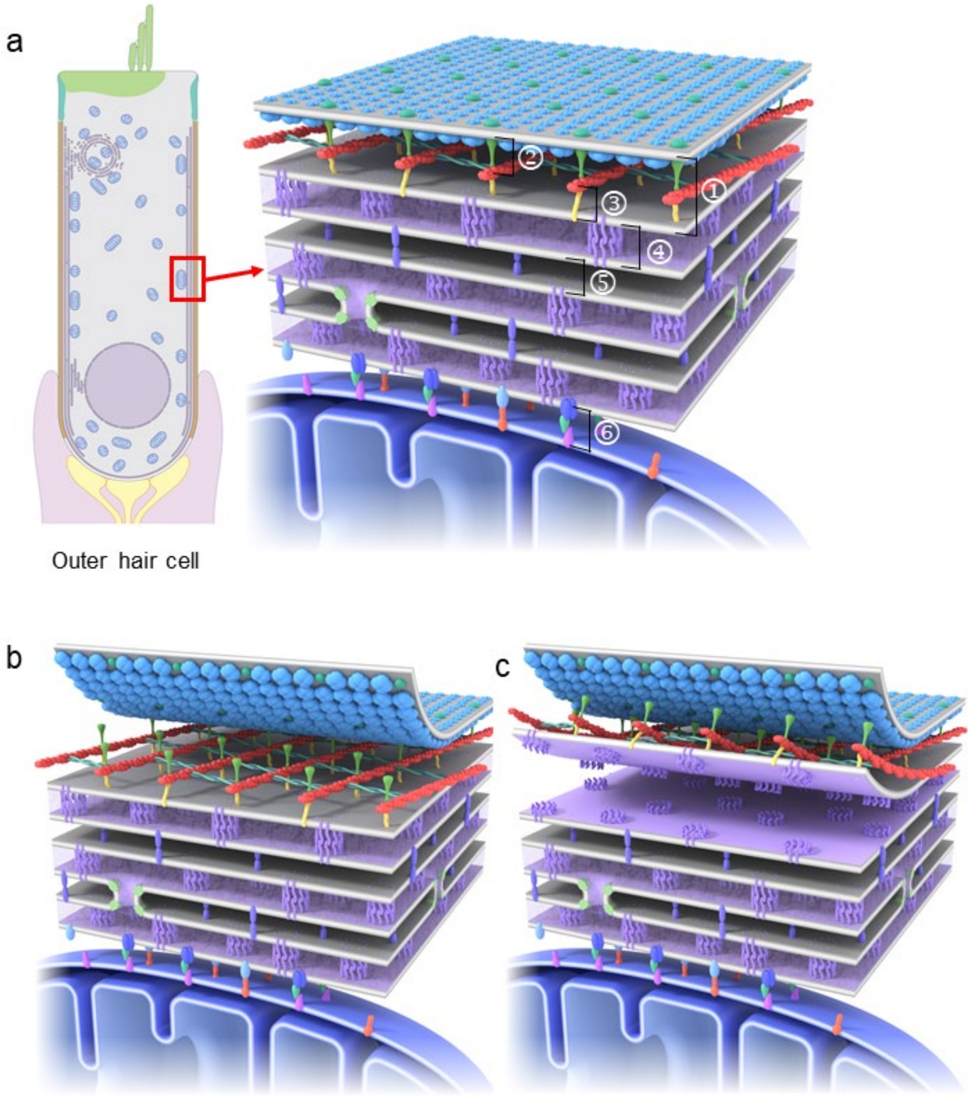

Figure 4.16 Outlining a structural blueprint of the outer hair cell lateral wall complex. (a – c) Schematic diagrams highlighting the spatial arrangements of structural features within the different layers of the lateral wall complex as determined by quantitative analysis of data from near-native state samples. Measurements at the numbered locations in **(a)** are in **Table 4.1**. **(b – c)** Peeled away views revealing structural details of the cortical lattice and the lateral cisternae, respectively. All spatial organizations are drawn to scale. Illustration by Ethan Tyler and Alan Hoofring, NIH Medical Arts Design Section.

Table 4.1 Spatial arrangements of lateral wall complex components.

Location		Measurement (nm)
①	LM to LC	38.4 ± 4.0
②	LM to CL	22.2 ± 2.1
③	CL to LC	17.2 ± 2.5
④	Inter-cisternal space	22.7 ± 3.2
⑤	Intra-cisternal space	18.8 ± 3.3
⑥	LC-M links	23.0 ± 4.1

LM: lateral plasma membrane CL: cortical lattice LC: lateral cisternae M: mitochondria

While the overall appearance of the lateral plasma membrane is uniform, freeze-fracture/freeze-etching replicas helped unveil that the membrane is densely populated with particles. Our replica-based data identified two distinct types of particle arrangement within the lateral plasma membrane. In the first scenario, membrane particles are organized orthogonally and form repeating microdomains throughout the lateral plasma membrane (Figure 4.5). The dimensions, spatial arrangement and abundance of these particles in combination with existing knowledge on structures of proteins related to prestin, led us to hypothesize that prestin molecules are expressed in the lateral plasma membrane as orthogonally interacting tetramers that form repeating microdomains. The contiguity of these microdomains and the tightly packed prestin molecules within each domain would allow for the physical manifestation of the proposed area motor model where prestin conformational change occurring *en masse* would lead to a change in membrane area and result in the observed outer hair cell length change (Iwasa, 1994). The second type of membrane particle arrangement observed in our replicas showed particles in linear arrays with regular spacing (Figure

4.6). The ~50 nm spacing between arrays matches the distance between actin filaments within the cortical lattice (M. C. Holley et al., 1992). Moreover, images from our replica showed the insertion of pillar-shaped structures into the lateral plasma membrane (Figure 4.6c). These observations led us to reason that the regularly spaced linear particle arrays are associated with these pillars. The spatial arrangement of these two types of membrane particle organization results in two interlocking arrays in the lateral plasma membrane (Figure 4.15).

Tomographic data revealed that the different layers of the lateral wall complex have consistent and regular spacings and are integrated via physical connections from the lateral plasma membrane to the associated mitochondria (Figure 4.7, 4.8 & 4.11). In addition, replica-based visualization of the lateral cisternae membranes showed a unique set of proteins are abundantly expressed in the membrane of this ER network (Figure 4.9a). These observations suggest that the precise spatial and structural organization of the components within the lateral wall complex are critical in orchestrating functionally distinct layers to work in concert to achieve outer hair cell electromotility. The well-define space between the lateral plasma membrane and the lateral cisternae compartmentalizes the region to provide an optimal operating environment for both prestin molecules in the plasma membrane and the cortical lattice. This compartmentalization by the extensive plasma membrane facing ER sheet within the lateral cisternae likely has a key role in regulating ions such as Ca^{2+} and Cl^{-}, which have been reported to be involved in prestin functional regulation and operation (Keller et al., 2014; Oliver et al., 2001; J. Santos-Sacchi, Song, Zheng, & Nuttall, 2006; Spicer, Thomopoulos, & Schulte, 1998). On the other hand, the cytoplasmic facing portion of the lateral cisternae along with the associated mitochondria carry out functions related to cellular homeostasis and energy production to support the sustained outer hair cell activity. The cortical lattice bridges the lateral plasma membrane and the lateral cisternae via its associated filamentous linkers. The connections between the cortical lattice and the plasma membrane help in the transmission of the forces generated by prestin molecules to the rest of the cell. The bonds between the cortical lattice and the lateral cisternae help recruit and retain the elaborate ER-mitochondria organization at the lateral wall. This physical integration of all the critical components in one location likely promotes synergistic interactions between different functional layers to achieve and sustain optimal voltage-dependent motility. These results enabled us to outline a structural blueprint that helps us better understand how the organization of the lateral wall complex could drive outer hair cell electromotility (Figure 4.16).

Chapter 5: Summary and Future Directions

5.1 – Summary

This body of work aims to improve our understanding of how spatial organization and structural integration at the outer hair cell lateral wall enable effective channeling of molecular interactions into the observed macroscopic voltage-dependent cellular motility. Our use of cryogenic sample preparation, electron tomography and replica-based techniques helped visualize the structural building blocks of this multilayered cortical structure at the outer hair cell lateral wall in a configuration close to their native state (Figure 4.16). While major elements within the lateral wall complex have been identified, such as prestin and spectrin molecules, our data suggest that a host of structural components remains to be characterized. In addition, how the assembly of these building blocks results in a functional unit for electromotility remains to be determined. Moreover, it is important to note that the structural blueprint outlined here represents only a snapshot of one particular state of the lateral wall complex and it is limited in resolution because of our methods. Our understanding of the dynamic changes that take place throughout electromotility is therefore incomplete. While our structural blueprint is limited in scope, it serves highlights structural components and new features, such as the orthogonal packing of prestin tetramers, the membrane particles embedded in the lumen of the lateral cisternae and the electron-dense links connecting individual ER sheets, which need identification and characterization. We believe that full characterization of these molecular building blocks will increase our overall understanding of the structure-function relationship between the lateral wall complex and the voltage-dependent cellular motility that operates at sound frequencies. Ultimately, improving our understanding of the lateral wall complex will help us better define the role of electromotility in cochlear amplification.

5.2 – Areas of interest for future studies

5.2.1 – Moving towards a molecular and cellular understanding of outer hair cell electromotility

One of the most striking structural features highlighted by our structural blueprint of the lateral wall complex is the repeating membrane-embedded ring-like complex found in the lumen of the lateral cisternae. The role of the lateral cisternae in electromotility remains unclear, however, this ER organization has been suggested to be involved in outer hair cell cellular homeostasis and age-related hearing loss (Perkins et al., 2020). Examining aging mice revealed that the lumen of the lateral cisternae increases in size, a sign of ER stress (Chavez-Valdez, Flock, Martin, & Northington, 2016). The dilation of the lateral cisternae lumen indicates that there is a change in ER morphology and regulation of ER luminal content, such as storage of Ca^{2+}, may be disrupted. The abundantly expressed ring-like protein complexes in the lumen of the lateral cisternae, as shown by our freeze-etching replica, could be involved in either shaping ER morphology by acting as luminal spacers or serving as channels/transporters that facilitate the regulation of solutes, such as Ca^{2+} or Cl^{-}, as postulated in chapter 3. To elucidate the identity of these repeating ER lumen structures, we searched RNA-seq databases to find candidate ER proteins that are highly expressed in outer hair cells (Liu et al., 2018; Liu et al., 2014). Based on the ER swelling phenotype observed in aging mice (Perkins et al., 2020), we narrowed our search to channels and transporters that are highly enriched in the ER. Existing literature indicates that aquaporin-11 (AQP11), an ER-resident protein that is part of the aquaporin family of membrane channels that facilitate the passage of water and other solutes along concentration gradient across the lipid bilayer, is highly enriched in outer hair cells (Liu et al., 2014; Miyoshi et al., 2017). In addition to water molecules, AQP11 has been shown to transport H_2O_2 across the ER membrane (Bestetti et al., 2020).

AQP11's ability to facilitate the movement of H_2O_2 suggests that it could be involved in redox homeostasis and signaling (Bestetti et al., 2020). If these repeating ring-like complexes are AQP11 or associated with AQP11 then that would suggest that the lateral cisternae and the tethered mitochondrial population participate in redox pathways (Yoboue, Sitia, & Simmen, 2018). Cellular stress has been suggested to affect redox homeostasis and mitochondrial dynamics, indicating that dysfunctional redox signaling pathways could underlie the changes to ER morphology and ER-mitochondria interface in aging mice (Perkins et al., 2020; Willems, Rossignol, Dieteren, Murphy, & Koopman, 2015). We immunofluorescently labelled for AQP11 in prestin-YFP mouse (courtesy of Dr. Jian Zuo, Creighton University) to examine AQP11's localization within outer hair cells (Figure 4.1). We observed that AQP11 is expressed throughout the outer hair cell basolateral plasma membrane and the nuclear envelope (Figure 5.1a & b). The AQP11 signal is immediately adjacent to the prestin-YFP signal (Figure 5.1c & d), suggesting it could be located within the lateral cisternae. To further assess the native expression pattern of AQP11 and to more accurately define the location of AQP11 along the outer hair cell lateral wall, immune-gold labelling of AQP11 on plastic sections of directly frozen and unfixed samples is needed.

While AQP11 appears to be located in proximity to the lateral plasma membrane and has the potential to contribute to functions carried out by the lateral cisternae, ABR thresholds of AQP11 knockout mice and wild-type mice were comparable (Miyoshi et al., 2017). This observation suggests that outer hair cells remain functional despite lacking AQP11, in comparison, prestin knockout mice have a significant decrease (~70 dBs) in ABR thresholds (M. C. Liberman et al., 2002). Given that AQP11 knockout mice die within several weeks after birth due to kidney dysfunction (Morishita et al., 2005), generating a hair cell specific AQP11 knockout mouse strain would be needed to better understand the role of AQP11 in outer hair cells. The lack of AQP11 should cause morphological changes to the lateral cisternae and its structural relationship with the mitochondrial population. In addition, if the repeating ring-like complexes within the lateral cisternae lumen are associated with

AQP11, freeze-etching electron microscopy can help visualize structural changes to the lateral cisternae lumen in AQP11 knockout mice.

Figure 5.1 (page 142) AQP11 is a novel lateral cisternae protein. (a – b) Immunofluorescent labeling of the organ of Corti from prestin-YFP mice. **(a)** Immunofluorescent labeling of postnatal day 15 cochlea (post-onset of hearing) with AQP11 (in yellow) and αII-spectrin (in magenta). The lateral plasma membrane is labeled with prestin-YFP (in cyan). AQP11 shows clear labeling throughout the basolateral plasma membrane and the nuclear envelope. **(b)** Immunofluorescent labeling of postnatal day 25 cochlea with AQP11 (in magenta) and COX IV (cytochrome c oxidase subunit 4, a mitochondrial marker, in yellow). Prestin-YFP is in cyan. AQP11 is expressed throughout the basolateral plasma membrane and the nuclear envelope, similar to the labeling at postnatal day 15. **(c – d)** Fluorescent intensity plots of each label at the outer hair cell lateral wall. **(c)** The fluorescent intensity profile of each label from **(a)** shows that prestin, αII-spectrin and AQP11 are adjacent to each other. **(d)** Fluorescent intensity profile for each label in (b) at the lateral wall. AQP11 and prestin-YFP appear to be in closer association at postnatal day 25 compare to postnatal day 15 as shown in **(c)**. Scale bars = 10 μm.

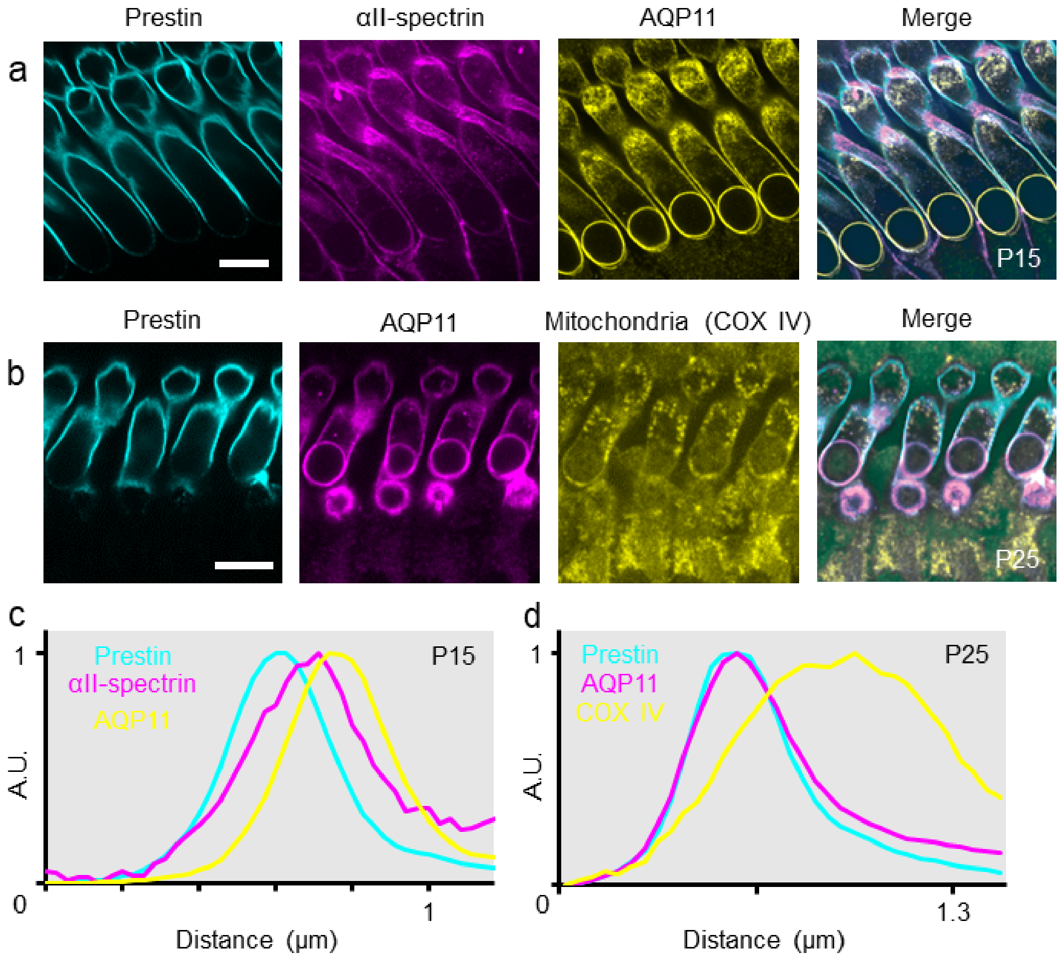

Figure 5.1 (legend on page 141)

5.2.2 – Examining the outer hair cell lateral wall complex with cryo-electron microscopy

Electron tomography and freeze-etching electron microscopy have provided valuable insights into the structures that underlie outer hair cell electromotility. However, the resolution that these techniques can achieve is limited by the heavy metal counterstain. Resolving molecular-level details such as the conformation of spectrin tetramers that crosslink actin filaments and the protein structure of prestin require high-resolution imaging. Cryo-electron microscopy provides a venue to achieve higher resolution by enabling direct imaging of the biological sample in a near-native state and the use of a direct electron detector (Nievergelt, Viar, & Pigino, 2019). One of the outstanding questions in understanding outer hair cell electromotility is the structure of prestin itself. Only recently have experimental data on the structure of relatives of prestin have been obtained (Chi et al., 2020; Geertsma et al., 2015; Walter et al., 2019). These sets of experimental data enable homology modelling of prestin (Figure 4.14) that enable computational analyses of the molecular conformational dynamics of prestin and how it leads to electromotility. To obtain a mechanistic framework for prestin function, an experimentally determined protein structure is needed. Single-particle cryo-electron microscopy will be needed to solve the protein structure of prestin via examining reconstituted prestin molecules in detergents, in lipid nano disk preparations or in their native site in the lateral plasma membrane. Moreover, the same approach can be used to solve the AQP11 protein structure.

In addition to the molecular characterization of individual proteins, such as prestin, we are interested in the supramolecular characterization of major components within the lateral wall complex, such as the actin-spectrin cortical lattice. Current understanding of the cortical lattice suggests that actin filaments are crosslinked by αII-βV spectrins that result in a ~50 nm spacing between filaments (M. C. Holley et al., 1992; Legendre et al., 2008). However, βV spectrin is a very large protein with over 3000 amino acids, weighing more than 400 kDa and contains 30 spectrin repeats (Stabach & Morrow, 2000). The protein conformation of the αII-βV spectrins that would result in a ~50 nm length has not been solved. Cryo-electron tomography can be used to visualize the cortical lattice in mechanically opened outer hair cells using a technique comparable to the Cryo-EM of unroofed cells in culture (Sochacki et al., 2021). If we can solve the conformation of spectrin molecules, we will be able to better understand how the cortical lattice interacts with other parts of the lateral wall complex and how it contributes to electromotility. We anticipate that using cryo-electron microscopy to examine the lateral wall complex will help in the identification of the various structural components highlighted in our blueprint and help reveal subtler elements. The ability to image the lateral wall complex in its native environment at high resolution would help move us closer to a comprehensive understanding of the relationship between the lateral wall complex and outer hair cell electromotility.

Bibliography

Adler, H. J., Belyantseva, I. A., Merritt, R. C., Jr., Frolenkov, G. I., Dougherty, G. W., & Kachar, B. (2003). Expression of prestin, a membrane motor protein, in the mammalian auditory and vestibular periphery. *Hear Res, 184*(1-2), 27-40.

Alper, S. L., & Sharma, A. K. (2013). The SLC26 gene family of anion transporters and channels. *Mol Aspects Med, 34*(2-3), 494-515. doi: 10.1016/j.mam.2012.07.009

Arnold, W., & Anniko, M. (1989). Supporting and membrane structures of human outer hair cells: evidence for an isometric contraction. *ORL J Otorhinolaryngol Relat Spec, 51*(6), 339-353. doi: 10.1159/000276086

Ashmore, J. (2008). Cochlear outer hair cell motility. *Physiol Rev, 88*(1), 173-210. doi: 10.1152/physrev.00044.2006

Ashmore, J. F. (1987). A fast motile response in guinea-pig outer hair cells: the cellular basis of the cochlear amplifier. *J Physiol, 388*, 323-347. doi: 10.1113/jphysiol.1987.sp016617

Bai, J. P., Navaratnam, D., Samaranayake, H., & Santos-Sacchi, J. (2006). En block C-terminal charge cluster reversals in prestin (SLC26A5): effects on voltage-dependent electromechanical activity. *Neurosci Lett, 404*(3), 270-275. doi: 10.1016/j.neulet.2006.05.062

Baines, A. J. (2010). The spectrin–ankyrin–4.1–adducin membrane skeleton: adapting eukaryotic cells to the demands of animal life. *Protoplasma, 244*(1), 99-131. doi: 10.1007/s00709-010-0181-1

Belyantseva, I. A., Frolenkov, G. I., Wade, J. B., Mammano, F., & Kachar, B. (2000). Water permeability of cochlear outer hair cells: characterization and relationship to electromotility. *J Neurosci, 20*(24), 8996-9003.

Bestetti, S., Galli, M., Sorrentino, I., Pinton, P., Rimessi, A., Sitia, R., & Medraño-Fernandez, I. (2020). Human aquaporin-11 guarantees efficient transport of H(2)O(2) across the endoplasmic reticulum membrane. *Redox Biol, 28*, 101326. doi: 10.1016/j.redox.2019.101326

Birkenhäger, R., Otto, E., Schürmann, M. J., Vollmer, M., Ruf, E. M., Maier-Lutz, I., . . . Hildebrandt, F. (2001). Mutation of BSND causes Bartter syndrome with sensorineural deafness and kidney failure. *Nat Genet, 29*(3), 310-314. doi: 10.1038/ng752

Brownell, W. E. (1990). Outer hair cell electromotility and otoacoustic emissions. *Ear Hear, 11*(2), 82-92. doi: 10.1097/00003446-199004000-00003

Brownell, W. E., Bader, C. R., Bertrand, D., & de Ribaupierre, Y. (1985). Evoked mechanical responses of isolated cochlear outer hair cells. *Science, 227*(4683), 194-196. doi: 10.1126/science.3966153

Brownell, W. E., & Kachar, B. (1986). *Outer Hair Cell Motility: A Possible Electro-Kinetic Mechanism*, Berlin, Heidelberg.

Brownell, W. E., Spector, A. A., Raphael, R. M., & Popel, A. S. (2001). Micro- and nanomechanics of the cochlear outer hair cell. *Annu Rev Biomed Eng, 3*, 169-194. doi: 10.1146/annurev.bioeng.3.1.169

Bullen, A., Taylor, R. R., Kachar, B., Moores, C., Fleck, R. A., & Forge, A. (2014). Inner ear tissue preservation by rapid freezing: improving fixation by high-pressure freezing and hybrid methods. *Hear Res, 315*, 49-60. doi: 10.1016/j.heares.2014.06.006

Burns, J. C., Kelly, M. C., Hoa, M., Morell, R. J., & Kelley, M. W. (2015). Single-cell RNA-Seq resolves cellular complexity in sensory organs from the neonatal inner ear. *Nat Commun, 6*, 8557. doi: 10.1038/ncomms9557

Cardenas, C., Miller, R. A., Smith, I., Bui, T., Molgo, J., Muller, M., . . . Foskett, J. K. (2010). Essential regulation of cell bioenergetics by constitutive InsP3 receptor Ca2+ transfer to mitochondria. *Cell, 142*(2), 270-283. doi: 10.1016/j.cell.2010.06.007

Chang, Y.-N., Jaumann, E. A., Reichel, K., Hartmann, J., Oliver, D., Hummer, G., . . . Geertsma, E. R. (2019). Structural basis for functional interactions in dimers of SLC26 transporters. *Nat Commun, 10*(1), 2032. doi: 10.1038/s41467-019-10001-w

Chavez-Valdez, R., Flock, D. L., Martin, L. J., & Northington, F. J. (2016). Endoplasmic reticulum pathology and stress response in neurons precede programmed necrosis after neonatal hypoxia-ischemia. *International journal of developmental neuroscience : the official journal of the International Society for Developmental Neuroscience, 48*, 58-70. doi: 10.1016/j.ijdevneu.2015.11.007

Cheatham, M. A., Huynh, K. H., Gao, J., Zuo, J., & Dallos, P. (2004). Cochlear function in Prestin knockout mice. *J Physiol, 560*(Pt 3), 821-830. doi: 10.1113/jphysiol.2004.069559

Cheatham, M. A., Zheng, J., Huynh, K. H., Du, G. G., Edge, R. M., Anderson, C. T., . . . Dallos, P. (2007). Evaluation of an independent prestin mouse model derived from the 129S1 strain. *Audiol Neurootol, 12*(6), 378-390. doi: 10.1159/000106481

Chertoff, M. E., & Brownell, W. E. (1994). Characterization of cochlear outer hair cell turgor. *Am J Physiol, 266*(2 Pt 1), C467-479. doi: 10.1152/ajpcell.1994.266.2.C467

Chessum, L., Matern, M. S., Kelly, M. C., Johnson, S. L., Ogawa, Y., Milon, B., . . . Hertzano, R. (2018). Helios is a key transcriptional regulator of outer hair cell maturation. *Nature, 563*(7733), 696-700. doi: 10.1038/s41586-018-0728-4

Chevalier, L., Selim, J., Genty, D., Baste, J. M., Piton, N., Boukhalfa, I., . . . Richard, V. (2017). Electron microscopy approach for the visualization of the epithelial and endothelial glycocalyx. *Morphologie, 101*(333), 55-63. doi: 10.1016/j.morpho.2017.04.001

Chi, X., Jin, X., Chen, Y., Lu, X., Tu, X., Li, X., . . . Lei, J. (2020). Structural insights into the gating mechanism of human SLC26A9 mediated by its C-terminal sequence. *6*, 55. doi: 10.1038/s41421-020-00193-7

Compton, E. L., Karinou, E., Naismith, J. H., Gabel, F., & Javelle, A. (2011). Low resolution structure of a bacterial SLC26 transporter reveals dimeric stoichiometry and mobile intracellular domains. *J Biol Chem, 286*(30), 27058-27067. doi: 10.1074/jbc.M111.244533

Compton, E. L., Page, K., Findlay, H. E., Haertlein, M., Moulin, M., Zachariae, U., . . . Javelle, A. (2014). Conserved structure and domain organization among bacterial Slc26 transporters. *Biochem J, 463*(2), 297-307. doi: 10.1042/bj20130619

Corfield, A. P. (2018). The Interaction of the Gut Microbiota with the Mucus Barrier in Health and Disease in Human. *Microorganisms, 6*(3), 78. doi: 10.3390/microorganisms6030078

Cortese, M., Papal, S., Pisciottano, F., Elgoyhen, A. B., Hardelin, J. P., Petit, C., . . . El-Amraoui, A. (2017). Spectrin betaV adaptive mutations and changes in subcellular location correlate with emergence of hair cell electromotility in mammalians. *Proc Natl Acad Sci U S A, 114*(8), 2054-2059. doi: 10.1073/pnas.1618778114

Crawley, S. W., Mooseker, M. S., & Tyska, M. J. (2014). Shaping the intestinal brush border. *J Cell Biol, 207*(4), 441-451. doi: 10.1083/jcb.201407015

Crawley, S. W., Shifrin, D. A., Jr., Grega-Larson, N. E., McConnell, R. E., Benesh, A. E., Mao, S., . . . Tyska, M. J. (2014). Intestinal brush border assembly driven by protocadherin-based intermicrovillar adhesion. *Cell, 157*(2), 433-446. doi: 10.1016/j.cell.2014.01.067

Crowther, R. A., DeRosier, D. J., & Klug, A. (1970). The reconstruction of a three-dimensional structure from projections and its application to electron microscopy. *Proceedings of the Royal Society of London. A. Mathematical and Physical Sciences, 317*(1530), 319-340. doi: doi:10.1098/rspa.1970.0119

Csordás, G., Renken, C., Várnai, P., Walter, L., Weaver, D., Buttle, K. F., . . . Hajnóczky, G. (2006). Structural and functional features and significance of the physical linkage between ER and mitochondria. *J Cell Biol, 174*(7), 915-921. doi: 10.1083/jcb.200604016

Csordás, G., Várnai, P., Golenár, T., Roy, S., Purkins, G., Schneider, T. G., . . . Hajnóczky, G. (2010). Imaging interorganelle contacts and local calcium dynamics at the ER-mitochondrial interface. *Mol Cell, 39*(1), 121-132. doi: 10.1016/j.molcel.2010.06.029

Dallos, P., & Corey, M. E. (1991). The role of outer hair cell motility in cochlear tuning. *Curr Opin Neurobiol, 1*(2), 215-220. doi: 10.1016/0959-4388(91)90081-h

Dallos, P., Evans, B. N., & Hallworth, R. (1991). Nature of the motor element in electrokinetic shape changes of cochlear outer hair cells. *Nature, 350*(6314), 155-157. doi: 10.1038/350155a0

Dallos, P., & Harris, D. (1978). Properties of auditory nerve responses in absence of outer hair cells. *J Neurophysiol, 41*(2), 365-383. doi: 10.1152/jn.1978.41.2.365

Dallos, P., Wu, X., Cheatham, M. A., Gao, J., Zheng, J., Anderson, C. T., . . . Zuo, J. (2008). Prestin-based outer hair cell motility is necessary for mammalian cochlear amplification. *Neuron, 58*(3), 333-339. doi: 10.1016/j.neuron.2008.02.028

De Rosier, D. J., & Klug, A. (1968). Reconstruction of three dimensional structures from electron micrographs. *Nature, 217*(5124), 130-134. doi: 10.1038/217130a0

Delpire, E., Lu, J., England, R., Dull, C., & Thorne, T. (1999). Deafness and imbalance associated with inactivation of the secretory Na-K-2Cl co-transporter. *Nat Genet, 22*(2), 192-195. doi: 10.1038/9713

Denoyelle, F., Lina-Granade, G., Plauchu, H., Bruzzone, R., Chaïb, H., Lévi-Acobas, F., . . . Petit, C. (1998). Connexin 26 gene linked to a dominant deafness. *Nature, 393*(6683), 319-320. doi: 10.1038/30639

Detro-Dassen, S., Schänzler, M., Lauks, H., Martin, I., zu Berstenhorst, S. M., Nothmann, D., . . . Fahlke, C. (2008). Conserved dimeric subunit stoichiometry of SLC26 multifunctional anion exchangers. *J Biol Chem, 283*(7), 4177-4188. doi: 10.1074/jbc.M704924200

Di Sano, F., Bernardoni, P., & Piacentini, M. (2012). The reticulons: guardians of the structure and function of the endoplasmic reticulum. *Exp Cell Res, 318*(11), 1201-1207. doi: 10.1016/j.yexcr.2012.03.002

Discher, D. E., & Carl, P. (2001). New insights into red cell network structure, elasticity, and spectrin unfolding--a current review. *Cell Mol Biol Lett, 6*(3), 593-606.

Dulon, D., Aran, J. M., & Schacht, J. (1987). Osmotically induced motility of outer hair cells: implications for Menière's disease. *Arch Otorhinolaryngol, 244*(2), 104-107. doi: 10.1007/bf00458558

Dulon, D., Zajic, G., & Schacht, J. (1990). Increasing intracellular free calcium induces circumferential contractions in isolated cochlear outer hair cells. *J Neurosci, 10*(4), 1388-1397. doi: 10.1523/jneurosci.10-04-01388.1990

Echlin, P. (1992). Freeze Substitution and Low-Temperature Embedding *Low-Temperature Microscopy and Analysis* (pp. 223-264). Boston, MA: Springer US.

Egberts, H. J., Koninkx, J. F., van Dijk, J. E., & Mouwen, J. M. (1984). Biological and pathobiological aspects of the glycocalyx of the small intestinal epithelium. A review. *Vet Q, 6*(4), 186-199. doi: 10.1080/01652176.1984.9693936

English, A. R., & Voeltz, G. K. (2013). Endoplasmic reticulum structure and interconnections with other organelles. *Cold Spring Harb Perspect Biol, 5*(4), a013227. doi: 10.1101/cshperspect.a013227

Espinosa-Marzal, R. M., Fontani, G., Reusch, F. B., Roba, M., Spencer, N. D., & Crockett, R. (2013). Sugars communicate through water: oriented glycans induce water structuring. *Biophys J, 104*(12), 2686-2694. doi: 10.1016/j.bpj.2013.05.017

Evans, E. F. (1972). The frequency response and other properties of single fibres in the guinea-pig cochlear nerve. *J Physiol, 226*(1), 263-287. doi: 10.1113/jphysiol.1972.sp009984

Evans, E. F., & Wilson, J. P. (1975). Cochlear tuning properties: concurrent basilar membrane and single nerve fiber measurements. *Science, 190*(4220), 1218-1221. doi: 10.1126/science.1198110

Fettiplace, R. (2017). Hair Cell Transduction, Tuning, and Synaptic Transmission in the Mammalian Cochlea. *Compr Physiol, 7*(4), 1197-1227. doi: 10.1002/cphy.c160049

Forge, A. (1991). Structural features of the lateral walls in mammalian cochlear outer hair cells. *Cell Tissue Res, 265*(3), 473-483. doi: 10.1007/bf00340870

Forge, A., Zajic, G., Li, L., Nevill, G., & Schacht, J. (1993). Structural variability of the sub-surface cisternae in intact, isolated outer hair cells shown by fluorescent labelling of intracellular membranes and freeze-fracture. *Hear Res, 64*(2), 175-183. doi: 10.1016/0378-5955(93)90003-J

Frangakis, A. S., & Hegerl, R. (2006). Segmentation of Three-dimensional Electron Tomographic Images. In J. Frank (Ed.), *Electron Tomography: Methods for Three-Dimensional Visualization of Structures in the Cell* (pp. 353-370). New York, NY: Springer New York.

Frank, J. (2006). Introduction: Principles of Electron Tomography. In J. Frank (Ed.), *Electron Tomography: Methods for Three-Dimensional Visualization of Structures in the Cell* (pp. 1-15). New York, NY: Springer New York.

Gaffney, M., Eichwald, J., Grosse, S. D., & Mason, C. A. (2010). Identifying Infants with Hearing Loss - United States, 1999-2007. *Morbidity and Mortality Weekly Report, 59*(8).

Geertsma, E. R., Chang, Y. N., Shaik, F. R., Neldner, Y., Pardon, E., Steyaert, J., & Dutzler, R. (2015). Structure of a prokaryotic fumarate transporter reveals the architecture of the SLC26 family. *Nat Struct Mol Biol, 22*(10), 803-808. doi: 10.1038/nsmb.3091

Giddings, T. H., Jr., O'Toole, E. T., Morphew, M., Mastronarde, D. N., McIntosh, J. R., & Winey, M. (2001). Using rapid freeze and freeze-substitution for the preparation of yeast cells for electron microscopy and three-dimensional analysis. *Methods in cell biology, 67*, 27-42. doi: 10.1016/s0091-679x(01)67003-1

Gilkey, J. C., & Staehelin, L. A. (1986). Advances in ultrarapid freezing for the preservation of cellular ultrastructure. *Journal of Electron Microscopy Technique, 3*(2), 177-210. doi: 10.1002/jemt.1060030206

Gillespie, P. G., & Müller, U. (2009). Mechanotransduction by hair cells: models, molecules, and mechanisms. *Cell, 139*(1), 33-44. doi: 10.1016/j.cell.2009.09.010

Gold, T., & Gray, J. (1948). Hearing. II. The physical basis of the action of the cochlea. *Proceedings of the Royal Society B: Biological Sciences, 135*(881), 492-498. doi: doi:10.1098/rspb.1948.0025

Gorbunov, D., Sturlese, M., Nies, F., Kluge, M., Bellanda, M., Battistutta, R., & Oliver, D. (2014). Molecular architecture and the structural basis for anion interaction in prestin and SLC26 transporters. *Nat Commun, 5*, 3622. doi: 10.1038/ncomms4622

Gulley, R. L., & Reese, T. S. (1977). Regional specialization of the hair cell plasmalemma in the organ of corti. *Anat Rec, 189*(1), 109-123. doi: 10.1002/ar.1091890108

Haddad, R. A., & Akansu, A. N. (1991). A class of fast Gaussian binomial filters for speech and image processing. *IEEE Transactions on Signal Processing, 39*(3), 723-727. doi: 10.1109/78.80892

Hallworth, R., & Nichols, M. G. (2012). Prestin in HEK cells is an obligate tetramer. *107*(1), 5-11. doi: 10.1152/jn.00728.2011

Hattrup, C. L., & Gendler, S. J. (2008). Structure and function of the cell surface (tethered) mucins. *Annu Rev Physiol, 70*, 431-457. doi: 10.1146/annurev.physiol.70.113006.100659

He, D. Z., Jia, S., Sato, T., Zuo, J., Andrade, L. R., Riordan, G. P., & Kachar, B. (2010). Changes in plasma membrane structure and electromotile properties in prestin deficient outer hair cells. *Cytoskeleton (Hoboken), 67*(1), 43-55. doi: 10.1002/cm.20423

Heuser, J. E. (2011). The origins and evolution of freeze-etch electron microscopy. *Journal of electron microscopy, 60 Suppl 1*(Suppl 1), S3-S29. doi: 10.1093/jmicro/dfr044

Heuser, J. E., & Reese, T. S. (1981). Structural changes after transmitter release at the frog neuromuscular junction. *J Cell Biol, 88*(3), 564-580. doi: 10.1083/jcb.88.3.564

Holley, M. C. (1996). Outer Hair Cell Motility. In P. Dallos, A. N. Popper & R. R. Fay (Eds.), *The Cochlea* (pp. 386-434). New York, NY: Springer New York.

Holley, M. C., & Ashmore, J. F. (1988a). A cytoskeletal spring in cochlear outer hair cells. *Nature, 335*(6191), 635. doi: 10.1038/335635a0

Holley, M. C., & Ashmore, J. F. (1988b). On the mechanism of a high-frequency force generator in outer hair cells isolated from the guinea pig cochlea. *Proc R Soc Lond B Biol Sci, 232*(1269), 413-429. doi: 10.1098/rspb.1988.0004

Holley, M. C., & Ashmore, J. F. (1990). Spectrin, actin and the structure of the cortical lattice in mammalian cochlear outer hair cells. *J Cell Sci, 96 (Pt 2)*, 283-291.

Holley, M. C., Kalinec, F., & Kachar, B. (1992). Structure of the cortical cytoskeleton in mammalian outer hair cells. *J Cell Sci, 102 (Pt 3)*, 569-580.

Homma, K., Duan, C., Zheng, J., Cheatham, M. A., & Dallos, P. (2013). The V499G/Y501H mutation impairs fast motor kinetics of prestin and has significance for defining functional independence of individual prestin subunits. *J Biol Chem, 288*(4), 2452-2463. doi: 10.1074/jbc.M112.411579

Homma, K., Miller, K. K., Anderson, C. T., Sengupta, S., Du, G. G., Aguinaga, S., . . . Zheng, J. (2010). Interaction between CFTR and prestin (SLC26A5). *Biochim Biophys Acta, 1798*(6), 1029-1040. doi: 10.1016/j.bbamem.2010.02.001

Hoppe, U., & Hesse, G. (2017). Hearing aids: indications, technology, adaptation, and quality control. *GMS current topics in otorhinolaryngology, head and neck surgery, 16*, Doc08-Doc08. doi: 10.3205/cto000147

Hu, J., Shibata, Y., Voss, C., Shemesh, T., Li, Z., Coughlin, M., . . . Prinz, W. A. (2008). Membrane proteins of the endoplasmic reticulum induce high-curvature tubules. *Science, 319*(5867), 1247-1250. doi: 10.1126/science.1153634

Ito, S. (1965). The enteric surface coat on cat intestinal microvilli. *J Cell Biol, 27*(3), 475-491. doi: 10.1083/jcb.27.3.475

Ito, S. (1974). Form and function of the glycocalyx on free cell surfaces. *Philos Trans R Soc Lond B Biol Sci, 268*(891), 55-66. doi: 10.1098/rstb.1974.0015

Iurato, S. (1961). Submicroscopic structure of the membranous labyrinth. *Zeitschrift für Zellforschung und Mikroskopische Anatomie, 53*(2), 259-298. doi: 10.1007/BF00339444

Iurato, S. (1962). Functional Implications of the Nature and Submicroscopic Structure of the Tectorial and Basilar Membranes. *J Acoust Soc Am, 34*(9B), 1386-1395. doi: 10.1121/1.1918355

Iwasa, K. H. (1993). Effect of stress on the membrane capacitance of the auditory outer hair cell. *Biophys J, 65*(1), 492-498. doi: 10.1016/S0006-3495(93)81053-1

Iwasa, K. H. (1994). A membrane motor model for the fast motility of the outer hair cell. *J Acoust Soc Am, 96*(4), 2216-2224. doi: 10.1121/1.410094

Izumikawa, M., Minoda, R., Kawamoto, K., Abrashkin, K. A., Swiderski, D. L., Dolan, D. F., . . . Raphael, Y. (2005). Auditory hair cell replacement and hearing improvement by Atoh1 gene therapy in deaf mammals. *Nat Med, 11*(3), 271-276. doi: 10.1038/nm1193

Jiang, M., Ji, Q., Wang, X., & McEwen, B. F. (2006). Segmentation of Cell Components Using Prior Knowledge. In J. Frank (Ed.), *Electron Tomography: Methods for Three-Dimensional Visualization of Structures in the Cell* (pp. 371-399). New York, NY: Springer New York.

Johansson, M. E., & Hansson, G. C. (2016). Immunological aspects of intestinal mucus and mucins. *Nat Rev Immunol, 16*(10), 639-649. doi: 10.1038/nri.2016.88

Johansson, M. E., Sjovall, H., & Hansson, G. C. (2013). The gastrointestinal mucus system in health and disease. *Nat Rev Gastroenterol Hepatol, 10*(6), 352-361. doi: 10.1038/nrgastro.2013.35

Johnstone, B. M., & Boyle, A. J. (1967). Basilar membrane vibration examined with the Mossbauer technique. *Science, 158*(3799), 389-390. doi: 10.1126/science.158.3799.389

Johnstone, B. M., Patuzzi, R., Syka, J., & Syková, E. (1989). Stimulus-related potassium changes in the organ of Corti of guinea-pig. *J Physiol, 408*, 77-92. doi: 10.1113/jphysiol.1989.sp017448

Jonathan, R. F., Laura, L. L., Matthew, W., Jared, R. D., Jodi, N., & Gia, K. V. (2011). ER Tubules Mark Sites of Mitochondrial Division. *Science (American Association for the Advancement of Science), 334*(6054), 358-362. doi: 10.1126/science.1207385

Jorgensen, L. E., & Messersmith, J. J. (2015). Impact of Aging and Cognition on Hearing Assistive Technology Use. *Semin Hear, 36*(3), 162-174. doi: 10.1055/s-0035-1555119

Kachar, B., Brownell, W. E., Altschuler, R., & Fex, J. (1986). Electrokinetic shape changes of cochlear outer hair cells. *Nature, 322*(6077), 365-368. doi: 10.1038/322365a0

Kachar, B., Liang, F., Lins, U., Ding, M., Wu, X. R., Stoffler, D., . . . Sun, T. T. (1999). Three-dimensional analysis of the 16 nm urothelial plaque particle: luminal surface exposure, preferential head-to-head interaction, and hinge formation. *J Mol Biol, 285*(2), 595-608. doi: 10.1006/jmbi.1998.2304

Kachar, B., Parakkal, M., Kurc, M., Zhao, Y., & Gillespie, P. G. (2000). High-resolution structure of hair-cell tip links. *Proc Natl Acad Sci U S A, 97*(24), 13336-13341. doi: 10.1073/pnas.97.24.13336

Kalinec, F., Holley, M. C., Iwasa, K. H., Lim, D. J., & Kachar, B. (1992). A membrane-based force generation mechanism in auditory sensory cells. *Proc Natl Acad Sci U S A, 89*(18), 8671-8675. doi: 10.1073/pnas.89.18.8671

Kawamoto, K., Ishimoto, S., Minoda, R., Brough, D. E., & Raphael, Y. (2003). Math1 gene transfer generates new cochlear hair cells in mature guinea pigs in vivo. *J Neurosci, 23*(11), 4395-4400. doi: 10.1523/jneurosci.23-11-04395.2003

Keller, J. P., Homma, K., Duan, C., Zheng, J., Cheatham, M. A., & Dallos, P. (2014). Functional regulation of the SLC26-family protein prestin by calcium/calmodulin. *J Neurosci, 34*(4), 1325-1332. doi: 10.1523/jneurosci.4020-13.2014

Kiang, N. Y., Sachs, M. B., & Peake, W. T. (1967). Shapes of tuning curves for single auditory-nerve fibers. *J Acoust Soc Am, 42*(6), 1341-1342. doi: 10.1121/1.1910723

Kitani, R., Park, C., & Kalinec, F. (2013). Microdomains shift and rotate in the lateral wall of cochlear outer hair cells. *Biophys J, 104*(1), 8-18. doi: 10.1016/j.bpj.2012.11.3828

Kitchen, P., Conner, M. T., Bill, R. M., & Conner, A. C. (2016). Structural Determinants of Oligomerization of the Aquaporin-4 Channel. *J Biol Chem, 291*(13), 6858-6871. doi: 10.1074/jbc.M115.694729

Klopfenstein, D. R., Klumperman, J., Lustig, A., Kammerer, R. A., Oorschot, V., & Hauri, H. P. (2001). Subdomain-specific localization of CLIMP-63 (p63) in the endoplasmic reticulum is mediated by its luminal alpha-helical segment. *J Cell Biol, 153*(6), 1287-1300. doi: 10.1083/jcb.153.6.1287

Ko, S. B., Zeng, W., Dorwart, M. R., Luo, X., Kim, K. H., Millen, L., . . . Muallem, S. (2004). Gating of CFTR by the STAS domain of SLC26 transporters. *Nat Cell Biol, 6*(4), 343-350. doi: 10.1038/ncb1115

Kokotas, Petersen, & Willems. (2007). Mitochondrial deafness. *Clinical genetics, 71*(5), 379-391. doi: 10.1111/j.1399-0004.2007.00800.x

Kraft, S., Hsu, C., Brough, D. E., & Staecker, H. (2013). Atoh1 induces auditory hair cell recovery in mice after ototoxic injury. *Laryngoscope, 123*(4), 992-999. doi: 10.1002/lary.22171

Kremer, J. R., Mastronarde, D. N., & McIntosh, J. R. (1996). Computer visualization of three-dimensional image data using IMOD. *J Struct Biol, 116*(1), 71-76. doi: 10.1006/jsbi.1996.0013

Kros, C. J. (1996). Physiology of Mammalian Cochlear Hair Cells. In P. Dallos, A. N. Popper & R. R. Fay (Eds.), *The Cochlea* (pp. 318-385). New York, NY: Springer New York.

Krystofiak, E. S., Heymann, J. B., & Kachar, B. (2019). Carbon replicas reveal double stranded structure of tight junctions in phase-contrast electron microscopy. *Commun Biol, 2*, 98. doi: 10.1038/s42003-019-0319-4

Lanzavecchia, S., Cantele, F., Bellon, P. L., Zampighi, L., Kreman, M., Wright, E., & Zampighi, G. A. (2005). Conical tomography of freeze-fracture replicas: a method for the study of integral membrane proteins inserted in phospholipid bilayers. *J Struct Biol, 149*(1), 87-98. doi: 10.1016/j.jsb.2004.09.004

Legendre, K., Safieddine, S., Kussel-Andermann, P., Petit, C., & El-Amraoui, A. (2008). alphaII-betaV spectrin bridges the plasma membrane and cortical lattice in the lateral wall of the auditory outer hair cells. *J Cell Sci, 121*(Pt 20), 3347-3356. doi: 10.1242/jcs.028134

Lenarz, T. (2018). Cochlear implant - state of the art. *GMS current topics in otorhinolaryngology, head and neck surgery, 16*, Doc04-Doc04. doi: 10.3205/cto000143

Lenormand, C., Spiegelhalter, C., Cinquin, B., Bardin, S., Bausinger, H., Angénieux, C., . . . de la Salle, H. (2013). Birbeck Granule-Like "Organized Smooth Endoplasmic Reticulum" Resulting from the Expression of a Cytoplasmic YFP-Tagged Langerin. *PLoS One, 8*(4), e60813. doi: 10.1371/journal.pone.0060813

Leonova, E. V., & Raphael, Y. (1999). Application of a platinum replica method to the study of the cytoskeleton of isolated hair cells, supporting cells and whole mounts of the organ of Corti. *Hear Res, 130*(1-2), 137-154. doi: 10.1016/s0378-5955(99)00004-0

Liberman, M. C., & Dodds, L. W. (1984). Single-neuron labeling and chronic cochlear pathology. III. Stereocilia damage and alterations of threshold tuning curves. *Hear Res, 16*(1), 55-74. doi: https://doi.org/10.1016/0378-5955(84)90025-X

Liberman, M. C., Gao, J., He, D. Z., Wu, X., Jia, S., & Zuo, J. (2002). Prestin is required for electromotility of the outer hair cell and for the cochlear amplifier. *Nature, 419*(6904), 300-304. doi: 10.1038/nature01059

Lin, F. R., Niparko, J. K., & Ferrucci, L. (2011). Hearing loss prevalence in the United States. *Archives of internal medicine, 171*(20), 1851-1852. doi: 10.1001/archinternmed.2011.506

Liu, H., Chen, L., Giffen, K. P., Stringham, S. T., Li, Y., Judge, P. D., . . . He, D. Z. Z. (2018). Cell-Specific Transcriptome Analysis Shows That Adult Pillar and Deiters' Cells Express Genes Encoding Machinery for Specializations of

Cochlear Hair Cells. *Front Mol Neurosci, 11*, 356. doi: 10.3389/fnmol.2018.00356

Liu, H., Pecka, J. L., Zhang, Q., Soukup, G. A., Beisel, K. W., & He, D. Z. (2014). Characterization of transcriptomes of cochlear inner and outer hair cells. *J Neurosci, 34*(33), 11085-11095. doi: 10.1523/jneurosci.1690-14.2014

Lohi, H., Kujala, M., Kerkelä, E., Saarialho-Kere, U., Kestilä, M., & Kere, J. (2000). Mapping of five new putative anion transporter genes in human and characterization of SLC26A6, a candidate gene for pancreatic anion exchanger. *Genomics, 70*(1), 102-112. doi: 10.1006/geno.2000.6355

Lolli, G., Pasqualetto, E., Costanzi, E., Bonetto, G., & Battistutta, R. (2016). The STAS domain of mammalian SLC26A5 prestin harbours an anion-binding site. *Biochem J, 473*(4), 365-370. doi: 10.1042/bj20151089

Lomize, M. A., Pogozheva, I. D., Joo, H., Mosberg, H. I., & Lomize, A. L. (2012). OPM database and PPM web server: resources for positioning of proteins in membranes. *Nucleic Acids Res, 40*(Database issue), D370-376. doi: 10.1093/nar/gkr703

Lučič, V., Rigort, A., & Baumeister, W. (2013). Cryo-electron tomography: the challenge of doing structural biology in situ. *J Cell Biol, 202*(3), 407-419. doi: 10.1083/jcb.201304193

Luther, P. K. (2006). Sample Shrinkage and Radiation Damage of Plastic Sections. In J. Frank (Ed.), *Electron Tomography: Methods for Three-Dimensional Visualization of Structures in the Cell* (pp. 17-48). New York, NY: Springer New York.

Lyu, A.-R., Kim, T. H., Park, S. J., Shin, S.-A., Jeong, S.-H., Yu, Y., . . . Park, Y.-H. (2020). Mitochondrial Damage and Necroptosis in Aging Cochlea. *International Journal of Molecular Sciences, 21*(7), 2505.

Mammano, F., Frolenkov, G. I., Lagostena, L., Belyantseva, I. A., Kurc, M., Dodane, V., . . . Kachar, B. (1999). ATP-Induced Ca<sup>2+</sup> Release in Cochlear Outer Hair Cells: Localization of an Inositol Triphosphate-Gated Ca<sup>2+</sup> Store to the Base of the Sensory Hair Bundle. *The Journal of Neuroscience, 19*(16), 6918. doi: 10.1523/JNEUROSCI.19-16-06918.1999

Manor, U., Disanza, A., Grati, M., Andrade, L., Lin, H., Di Fiore, P. P., . . . Kachar, B. (2011). Regulation of stereocilia length by myosin XVa and whirlin depends on the actin-regulatory protein Eps8. *Curr Biol, 21*(2), 167-172. doi: 10.1016/j.cub.2010.12.046

Marko, M., Hsieh, C.-E., & Mannella, C. A. (2006). Electron Tomography of Frozen-hydrated Sections of Cells and Tissues. In J. Frank (Ed.), *Electron Tomography: Methods for Three-Dimensional Visualization of Structures in the Cell* (pp. 49-81). New York, NY: Springer New York.

Marsh, B. J., Mastronarde, D. N., Buttle, K. F., Howell, K. E., & McIntosh, J. R. (2001). Organellar relationships in the Golgi region of the pancreatic beta cell line, HIT-T15, visualized by high resolution electron tomography. *Proceedings of the National Academy of Sciences, 98*(5), 2399-2406. doi: 10.1073/pnas.051631998

Mastronarde, D. N. (2005). Automated electron microscope tomography using robust prediction of specimen movements. *J Struct Biol, 152*(1), 36-51. doi: 10.1016/j.jsb.2005.07.007

Mathers, C., Smith, A., & Concha, M. (2000). Global burden of hearing loss in the year 2000. *Global Burden of Disease*.

McGrath, J., Roy, P., & Perrin, B. J. (2017). Stereocilia morphogenesis and maintenance through regulation of actin stability. *Semin Cell Dev Biol, 65*, 88-95. doi: 10.1016/j.semcdb.2016.08.017

Mio, K., Kubo, Y., Ogura, T., Yamamoto, T., Arisaka, F., & Sato, C. (2008). The motor protein prestin is a bullet-shaped molecule with inner cavities. *J Biol Chem, 283*(2), 1137-1145. doi: 10.1074/jbc.M702681200

Miyoshi, T., Yamaguchi, T., Ogita, K., Tanaka, Y., Ishibashi, K. I., Ito, H., . . . Yamamoto, N. (2017). Quantitative Analysis of Aquaporin Expression Levels during the Development and Maturation of the Inner Ear. *J Assoc Res Otolaryngol, 18*(2), 247-261. doi: 10.1007/s10162-016-0607-3

Morishita, Y., Matsuzaki, T., Hara-chikuma, M., Andoo, A., Shimono, M., Matsuki, A., . . . Ishibashi, K. (2005). Disruption of aquaporin-11 produces polycystic kidneys following vacuolization of the proximal tubule. *Mol Cell Biol, 25*(17), 7770-7779. doi: 10.1128/mcb.25.17.7770-7779.2005

Mutai, H., Suzuki, N., Shimizu, A., Torii, C., Namba, K., Morimoto, N., . . . Matsunaga, T. (2013). Diverse spectrum of rare deafness genes underlies early-childhood hearing loss in Japanese patients: a cross-sectional, multi-center nextgeneration sequencing study. *Orphanet journal of rare diseases, 8*, 172-172. doi: 10.1186/1750-1172-8-172

Muzumdar, M. D., Tasic, B., Miyamichi, K., Li, L., & Luo, L. (2007). A global double-fluorescent Cre reporter mouse. *Genesis, 45*(9), 593-605. doi: 10.1002/dvg.20335

Nagelhus, E. A., & Ottersen, O. P. (2013). Physiological roles of aquaporin-4 in brain. *Physiol Rev, 93*(4), 1543-1562. doi: 10.1152/physrev.00011.2013

Neely, S. T., & Kim, D. O. (1983). An active cochlear model showing sharp tuning and high sensitivity. *Hear Res, 9*(2), 123-130. doi: 10.1016/0378-5955(83)90022-9

Nievergelt, A. P., Viar, G. A., & Pigino, G. (2019). Towards a mechanistic understanding of cellular processes by cryoEM. *Current Opinion in Structural Biology, 58*, 149-158. doi: https://doi.org/10.1016/j.sbi.2019.06.008

Oliver, D., He, D. Z., Klocker, N., Ludwig, J., Schulte, U., Waldegger, S., . . . Fakler, B. (2001). Intracellular anions as the voltage sensor of prestin, the outer hair cell motor protein. *Science, 292*(5525), 2340-2343. doi: 10.1126/science.1060939

Osman, C., Voelker, D. R., & Langer, T. (2011). Making heads or tails of phospholipids in mitochondria. *J Cell Biol, 192*(1), 7-16. doi: 10.1083/jcb.201006159

Pan, S., Wan, J., Liu, S., Zhang, S., Xiong, H., Zhou, J., . . . Fu, Y. (2013). Lentivirus carrying the Atoh1 gene infects normal rat cochlea. *Neural regeneration research, 8*(17), 1551-1559. doi: 10.3969/j.issn.1673-5374.2013.17.002

Pasqualetto, E., Aiello, R., Gesiot, L., Bonetto, G., Bellanda, M., & Battistutta, R. (2010). Structure of the cytosolic portion of the motor protein prestin and functional role of the STAS domain in SLC26/SulP anion transporters. *J Mol Biol, 400*(3), 448-462. doi: 10.1016/j.jmb.2010.05.013

Pelaseyed, T., Bergstrom, J. H., Gustafsson, J. K., Ermund, A., Birchenough, G. M., Schutte, A., . . . Hansson, G. C. (2014). The mucus and mucins of the goblet cells and enterocytes provide the first defense line of the gastrointestinal tract and interact with the immune system. *Immunol Rev, 260*(1), 8-20. doi: 10.1111/imr.12182

Pelaseyed, T., Gustafsson, J. K., Gustafsson, I. J., Ermund, A., & Hansson, G. C. (2013). Carbachol-induced MUC17 endocytosis is concomitant with NHE3 internalization and CFTR membrane recruitment in enterocytes. *American journal of physiology. Cell physiology, 305*(4), C457-C467. doi: 10.1152/ajpcell.00141.2013

Penczek, P., Marko, M., Buttle, K., & Frank, J. (1995). Double-tilt electron tomography. *Ultramicroscopy, 60*(3), 393-410. doi: https://doi.org/10.1016/0304-3991(95)00078-X

Perkins, G., Lee, J. H., Park, S., Kang, M., Perez-Flores, M. C., Ju, S., . . . Yamoah, E. N. (2020). Altered Outer Hair Cell Mitochondrial and Subsurface Cisternae Connectomics Are Candidate Mechanisms for Hearing Loss in Mice. *The Journal of Neuroscience, 40*(44), 8556. doi: 10.1523/JNEUROSCI.2901-19.2020

Pettersen, E. F., Goddard, T. D., Huang, C. C., Couch, G. S., Greenblatt, D. M., Meng, E. C., & Ferrin, T. E. (2004). UCSF Chimera--a visualization system for exploratory research and analysis. *J Comput Chem, 25*(13), 1605-1612. doi: 10.1002/jcc.20084

Raphael, R. M., Popel, A. S., & Brownell, W. E. (2000). A membrane bending model of outer hair cell electromotility. *Biophys J, 78*(6), 2844-2862. doi: 10.1016/s0006-3495(00)76827-5

Rizzuto, R., Pinton, P., Carrington, W., Fay, F. S., Fogarty, K. E., Lifshitz, L. M., . . . Pozzan, T. (1998). Close contacts with the endoplasmic reticulum as determinants of mitochondrial Ca2+ responses. *Science, 280*(5370), 1763-1766. doi: 10.1126/science.280.5370.1763

Saito, K. (1983). Fine structure of the sensory epithelium of guinea-pig organ of Corti: subsurface cisternae and lamellar bodies in the outer hair cells. *Cell Tissue Res, 229*(3), 467-481. doi: 10.1007/bf00207692

Santos-Sacchi, J. (1991). Reversible inhibition of voltage-dependent outer hair cell motility and capacitance. *J Neurosci, 11*(10), 3096-3110.

Santos-Sacchi, J., & Dilger, J. P. (1988). Whole cell currents and mechanical responses of isolated outer hair cells. *Hear Res, 35*(2-3), 143-150. doi: 10.1016/0378-5955(88)90113-x

Santos-Sacchi, J., Navaratnam, D., Raphael, R., & Oliver, D. (2017). Prestin: Molecular Mechanisms Underlying Outer Hair Cell Electromotility. In G. A. Manley, A. W. Gummer, A. N. Popper & R. R. Fay (Eds.), *Understanding the Cochlea* (pp. 113-145). Cham: Springer International Publishing.

Santos-Sacchi, J., Song, L., Zheng, J., & Nuttall, A. L. (2006). Control of mammalian cochlear amplification by chloride anions. *J Neurosci, 26*(15), 3992-3998. doi: 10.1523/jneurosci.4548-05.2006

Scheller, E. L., & Krebsbach, P. H. (2009). Gene therapy: design and prospects for craniofacial regeneration. *J Dent Res, 88*(7), 585-596. doi: 10.1177/0022034509337480

Schindelin, J., Arganda-Carreras, I., Frise, E., Kaynig, V., Longair, M., Pietzsch, T., . . . Cardona, A. (2012). Fiji: an open-source platform for biological-image analysis. *Nat Methods, 9*(7), 676-682. doi: 10.1038/nmeth.2019

Schulze-Bahr, E., Wang, Q., Wedekind, H., Haverkamp, W., Chen, Q., Sun, Y., . . . Funke, H. (1997). KCNE1 mutations cause Jervell and Lange-Nielsen syndrome. *Nat Genet, 17*(3), 267-268. doi: 10.1038/ng1197-267

Schwander, M., Kachar, B., & Muller, U. (2010). Review series: The cell biology of hearing. *J Cell Biol, 190*(1), 9-20. doi: 10.1083/jcb.201001138

Schweizer, A., Ericsson, M., Bächi, T., Griffiths, G., & Hauri, H. P. (1993). Characterization of a novel 63 kDa membrane protein. Implications for the organization of the ER-to-Golgi pathway. *J Cell Sci, 104 (Pt 3)*, 671-683.

Shehata, W. E., Brownell, W. E., & Dieler, R. (1991). Effects of salicylate on shape, electromotility and membrane characteristics of isolated outer hair cells from guinea pig cochlea. *Acta Otolaryngol, 111*(4), 707-718. doi: 10.3109/00016489109138403

Shen, Z., Marcus, D. C., Sunose, H., Chiba, T., & Wangemann, P. (1997). I(sK) Channel in Strial Marginal Cells. Voltage-Dependence, Ion-Selectivity, Inhibition by 293B and Sensitivity to Clofilium. *Audit Neurosci, 3*(3), 215-230.

Shibagaki, N., & Grossman, A. R. (2004). Probing the function of STAS domains of the Arabidopsis sulfate transporters. *J Biol Chem, 279*(29), 30791-30799. doi: 10.1074/jbc.M403248200

Shibagaki, N., & Grossman, A. R. (2006). The role of the STAS domain in the function and biogenesis of a sulfate transporter as probed by random mutagenesis. *J Biol Chem, 281*(32), 22964-22973. doi: 10.1074/jbc.M603462200

Shibata, S. B., West, M. B., Du, X., Iwasa, Y., Raphael, Y., & Kopke, R. D. (2020). Gene therapy for hair cell regeneration: Review and new data. *Hear Res, 394*, 107981. doi: 10.1016/j.heares.2020.107981

Shibata, Y., Shemesh, T., Prinz, W. A., Palazzo, A. F., Kozlov, M. M., & Rapoport, T. A. (2010). Mechanisms determining the morphology of the peripheral ER. *Cell, 143*(5), 774-788. doi: 10.1016/j.cell.2010.11.007

Sitte, H., Edelmann, L., & Neumann, K. (1987). Cryofixation Without Pretreatment at Ambient Pressure. In R. A. Steinbrecht & K. Zierold (Eds.), *Cryotechniques in Biological Electron Microscopy* (pp. 87-113). Berlin, Heidelberg: Springer Berlin Heidelberg.

Smith, A. S., Nowak, R. B., Zhou, S., Giannetto, M., Gokhin, D. S., Papoin, J., . . . Fowler, V. M. (2018). Myosin IIA interacts with the spectrin-actin membrane skeleton to control red blood cell membrane curvature and deformability. *Proc Natl Acad Sci U S A*. doi: 10.1073/pnas.1718285115

Snapp, E. L., Hegde, R. S., Francolini, M., Lombardo, F., Colombo, S., Pedrazzini, E., . . . Lippincott-Schwartz, J. (2003). Formation of stacked ER cisternae by low affinity protein interactions. *J Cell Biol, 163*(2), 257-269. doi: 10.1083/jcb.200306020

Sochacki, K. A., Heine, B. L., Haber, G. J., Jimah, J. R., Prasai, B., Alfonzo-Méndez, M. A., . . . Taraska, J. W. (2021). The structure and spontaneous curvature of clathrin lattices at the plasma membrane. *Dev Cell, 56*(8), 1131-1146.e1133. doi: 10.1016/j.devcel.2021.03.017

Someya, S., Xu, J., Kondo, K., Ding, D., Salvi, R. J., Yamasoba, T., . . . Prolla, T. A. (2009). Age-related hearing loss in C57BL/6J mice is mediated by Bak-dependent mitochondrial apoptosis. *Proceedings of the National Academy of Sciences, 106*(46), 19432-19437. doi: 10.1073/pnas.0908786106

Spicer, S. S., Thomopoulos, G. N., & Schulte, B. A. (1998). Cytologic evidence for mechanisms of K+ transport and genesis of Hensen bodies and subsurface cisternae in outer hair cells. *Anat Rec, 251*(1), 97-113. doi: 10.1002/(sici)1097-0185(199805)251:1<97::aid-ar15>3.0.co;2-6

Spoendlin, H. (1969). Innervation patterns in the organ of corti of the cat. *Acta Otolaryngol, 67*(2), 239-254. doi: 10.3109/00016486909125448

Stabach, P. R., & Morrow, J. S. (2000). Identification and characterization of beta V spectrin, a mammalian ortholog of Drosophila beta H spectrin. *J Biol Chem, 275*(28), 21385-21395. doi: 10.1074/jbc.C000159200

Sun, W. W., Krystofiak, E. S., Leo-Macias, A., Cui, R., Sesso, A., Weigert, R., . . . Kachar, B. (2020). Nanoarchitecture and dynamics of the mouse enteric glycocalyx examined by freeze-etching electron tomography and intravital microscopy. *Commun Biol, 3*(1), 5. doi: 10.1038/s42003-019-0735-5

Sunose, H., Liu, J., & Marcus, D. C. (1997). cAMP increases K+ secretion via activation of apical IsK/KvLQT1 channels in strial marginal cells. *Hear Res, 114*(1-2), 107-116. doi: 10.1016/s0378-5955(97)00152-4

Sutherland, B. W., Toews, J., & Kast, J. (2008). Utility of formaldehyde cross-linking and mass spectrometry in the study of protein-protein interactions. *J Mass Spectrom, 43*(6), 699-715. doi: 10.1002/jms.1415

Swift, J. G., & Mukherjee, T. M. (1976). Demonstration of the fuzzy surface coat of rat intestinal microvilli by freeze-etching. *J Cell Biol, 69*(2), 491-495. doi: 10.1083/jcb.69.2.491

Szabadkai, G., Bianchi, K., Várnai, P., De Stefani, D., Wieckowski, M. R., Cavagna, D., . . . Rizzuto, R. (2006). Chaperone-mediated coupling of endoplasmic reticulum and mitochondrial Ca2+ channels. *J Cell Biol, 175*(6), 901-911. doi: 10.1083/jcb.200608073

Takahashi, S., Sun, W., Zhou, Y., Homma, K., Kachar, B., Cheatham, M. A., & Zheng, J. (2018). Prestin Contributes to Membrane Compartmentalization and Is Required for Normal Innervation of Outer Hair Cells. *Frontiers in Cellular Neuroscience, 12*(211). doi: 10.3389/fncel.2018.00211

Terasaki, M., Shemesh, T., Kasthuri, N., Klemm, R. W., Schalek, R., Hayworth, K. J., . . . Kozlov, M. M. (2013). Stacked endoplasmic reticulum sheets are connected by helicoidal membrane motifs. *Cell, 154*(2), 285-296. doi: 10.1016/j.cell.2013.06.031

Teubner, B., Michel, V., Pesch, J., Lautermann, J., Cohen-Salmon, M., Söhl, G., . . . Willecke, K. (2003). Connexin30 (Gjb6)-deficiency causes severe hearing impairment and lack of endocochlear potential. *Hum Mol Genet, 12*(1), 13-21. doi: 10.1093/hmg/ddg001

Tolomeo, J. A., Steele, C. R., & Holley, M. C. (1996). Mechanical properties of the lateral cortex of mammalian auditory outer hair cells. *Biophys J, 71*(1), 421-429. doi: 10.1016/s0006-3495(96)79244-5

Triffo, W. J., Palsdottir, H., Song, J., Morgan, D. G., McDonald, K. L., Auer, M., & Raphael, R. M. (2019). 3D Ultrastructure of the Cochlear Outer Hair Cell Lateral Wall Revealed By Electron Tomography. *Front Cell Neurosci, 13*, 560. doi: 10.3389/fncel.2019.00560

Trus, B. L., Kocsis, E., Conway, J. F., & Steven, A. C. (1996). Digital image processing of electron micrographs: the PIC system-III. *J Struct Biol, 116*(1), 61-67. doi: 10.1006/jsbi.1996.0011

Unsain, N., Stefani, F. D., & Cáceres, A. (2018). The Actin/Spectrin Membrane-Associated Periodic Skeleton in Neurons. *Frontiers in Synaptic Neuroscience, 10*(10). doi: 10.3389/fnsyn.2018.00010

Vance, J. E. (1990). Phospholipid synthesis in a membrane fraction associated with mitochondria. *J Biol Chem, 265*(13), 7248-7256.

Varki, A., Schnaar, R. L., & Schauer, R. (2015). Sialic Acids and Other Nonulosonic Acids. In A. Varki, R. D. Cummings, J. D. Esko, P. Stanley, G. W. Hart, M. Aebi, A. G. Darvill, T. Kinoshita, N. H. Packer, J. H. Prestegard, R. L. Schnaar

& P. H. Seeberger (Eds.), *Essentials of Glycobiology* (pp. 179-195). Cold Spring Harbor (NY): Cold Spring Harbor Laboratory Press

Copyright 2015-2017 by The Consortium of Glycobiology Editors, La Jolla, California. All rights reserved.

Vetter, D. E., Mann, J. R., Wangemann, P., Liu, J., McLaughlin, K. J., Lesage, F., . . . Barhanin, J. (1996). Inner ear defects induced by null mutation of the isk gene. *Neuron, 17*(6), 1251-1264. doi: 10.1016/s0896-6273(00)80255-x

Von Bekesy, G. (1952). Resting potentials inside the cochlear partition of the guinea pig. *Nature, 169*(4293), 241-242. doi: 10.1038/169241a0

Wada, H., Kimura, K., Gomi, T., Sugawara, M., Katori, Y., Kakehata, S., . . . Kobayashi, T. (2004). Imaging of the cortical cytoskeleton of guinea pig outer hair cells using atomic force microscopy. *Hear Res, 187*(1-2), 51-62.

Walter, J. D., Sawicka, M., & Dutzler, R. (2019). Cryo-EM structures and functional characterization of murine Slc26a9 reveal mechanism of uncoupled chloride transport. *eLife, 8*, e46986. doi: 10.7554/eLife.46986

Wang, X., Yang, S., Jia, S., & He, D. Z. (2010). Prestin forms oligomer with four mechanically independent subunits. *Brain Res, 1333*, 28-35. doi: 10.1016/j.brainres.2010.03.070

Wangemann, P. (2002). K+ cycling and the endocochlear potential. *Hear Res, 165*(1-2), 1-9. doi: 10.1016/s0378-5955(02)00279-4

Wangemann, P., Liu, J., & Marcus, D. C. (1995). Ion transport mechanisms responsible for K+ secretion and the transepithelial voltage across marginal cells of stria vascularis in vitro. *Hear Res, 84*(1-2), 19-29. doi: 10.1016/0378-5955(95)00009-s

Wangemann, P., & Schacht, J. (1996). Homeostatic Mechanisms in the Cochlea. In P. Dallos, A. N. Popper & R. R. Fay (Eds.), *The Cochlea* (pp. 130-185). New York, NY: Springer New York.

Waterhouse, A., Bertoni, M., Bienert, S., Studer, G., Tauriello, G., Gumienny, R., . . . Schwede, T. (2018). SWISS-MODEL: homology modelling of protein structures and complexes. *Nucleic Acids Res, 46*(W1), W296-w303. doi: 10.1093/nar/gky427

Willems, P. H., Rossignol, R., Dieteren, C. E., Murphy, M. P., & Koopman, W. J. (2015). Redox Homeostasis and Mitochondrial Dynamics. *Cell Metab, 22*(2), 207-218. doi: 10.1016/j.cmet.2015.06.006

Wong, K., Kozin, E. D., Kanumuri, V. V., Vachicouras, N., Miller, J., Lacour, S., . . . Lee, D. J. (2019). Auditory Brainstem Implants: Recent Progress and Future Perspectives. *Frontiers in Neuroscience, 13*(10). doi: 10.3389/fnins.2019.00010

Woods, C., Montcouquiol, M., & Kelley, M. W. (2004). Math1 regulates development of the sensory epithelium in the mammalian cochlea. *Nat Neurosci, 7*(12), 1310-1318. doi: 10.1038/nn1349

Wu, N., Li, M., Chen, Z. T., Zhang, X. B., Liu, H. Z., Li, Z., . . . Yang, S. M. (2013). In vivo delivery of Atoh1 gene to rat cochlea using a dendrimer-based nanocarrier. *J Biomed Nanotechnol, 9*(10), 1736-1745. doi: 10.1166/jbn.2013.1684

Xia, A., Kikuchi, T., Hozawa, K., Katori, Y., & Takasaka, T. (1999). Expression of connexin 26 and Na,K-ATPase in the developing mouse cochlear lateral wall: functional implications. *Brain Res, 846*(1), 106-111. doi: 10.1016/s0006-8993(99)01996-4

Yamashita, T., Hakizimana, P., Wu, S., Hassan, A., Jacob, S., Temirov, J., . . . Zuo, J. (2015). Outer Hair Cell Lateral Wall Structure Constrains the Mobility of Plasma Membrane Proteins. *PLoS Genet, 11*(9), e1005500. doi: 10.1371/journal.pgen.1005500

Yoboue, E. D., Sitia, R., & Simmen, T. (2018). Redox crosstalk at endoplasmic reticulum (ER) membrane contact sites (MCS) uses toxic waste to deliver messages. *Cell Death & Disease, 9*(3), 331. doi: 10.1038/s41419-017-0033-4

Yu, N., Zhu, M.-L., & Zhao, H.-B. (2006). Prestin is expressed on the whole outer hair cell basolateral surface. *Brain Res, 1095*(1), 51-58. doi: 10.1016/j.brainres.2006.04.017

Yu, S. B., & Pekkurnaz, G. (2018). Mechanisms Orchestrating Mitochondrial Dynamics for Energy Homeostasis. *J Mol Biol, 430*(21), 3922-3941. doi: 10.1016/j.jmb.2018.07.027

Zhang, H., & Hu, J. (2016). Shaping the Endoplasmic Reticulum into a Social Network. *Trends Cell Biol, 26*(12), 934-943. doi: 10.1016/j.tcb.2016.06.002

Zheng, J., Du, G. G., Anderson, C. T., Keller, J. P., Orem, A., Dallos, P., & Cheatham, M. (2006). Analysis of the oligomeric structure of the motor protein prestin. *J Biol Chem, 281*(29), 19916-19924. doi: 10.1074/jbc.M513854200

Zheng, J., Du, G. G., Matsuda, K., Orem, A., Aguinaga, S., Deak, L., . . . Dallos, P. (2005). The C-terminus of prestin influences nonlinear capacitance and plasma membrane targeting. *J Cell Sci, 118*(Pt 13), 2987-2996. doi: 10.1242/jcs.02431

Zheng, J., Shen, W., He, D. Z., Long, K. B., Madison, L. D., & Dallos, P. (2000). Prestin is the motor protein of cochlear outer hair cells. *Nature, 405*(6783), 149-155. doi: 10.1038/35012009

Zheng, J. L., & Gao, W. Q. (2000). Overexpression of Math1 induces robust production of extra hair cells in postnatal rat inner ears. *Nat Neurosci, 3*(6), 580-586. doi: 10.1038/75753

Zidanic, M., & Brownell, W. E. (1990). Fine structure of the intracochlear potential field. I. The silent current. *Biophys J, 57*(6), 1253-1268. doi: 10.1016/S0006-3495(90)82644-8

Zych, A. (2017). What Do Cochlear Implants And Hearing Aids Sound Like? doi: https://www.sciencefriday.com/educational-resources/cochlear-implants-hearing-aids-sound-like/